Mixing and Combustion of Rich Fireballs

F. Pintgen and J. E. Shepherd

Graduate Aeronautical Laboratories
California Institute of Technology
Pasadena, CA 91125
U.S.A.

GALCIT Report FM2003-004
October 14, 2003

prepared for Sandia National Laboratory
Albuquerque, NM USA

Abstract

A series of experiments was carried out to investigate the effect of fireball composition on secondary combustion. The fireball was created from a 1.5 liter balloon filled with a propane-oxygen mixture ($1< \Phi <3$) and initiated by a detonation. Two initiation locations and two initiator strengths were studied. Two pencil pressure gauges located at 0.6 and 1.2 m and in some experiments, simultaneous high-speed imaging, were used as diagnostics. For $\Phi > 1$, the incompletely oxidized products from the primary burn mix with the surrounding air and may be oxidized in a secondary combustion process.

The unique feature of the present experiments was a repeatable secondary pressure pulse for sufficiently rich mixtures. The secondary pressure rise was observed repeatably for all initiation configurations. The nature of the secondary pressure pulse is a strong function of the initial equivalence ratio. For $\Phi = 1$ and 1.5, no secondary pressure waves are observed. An acoustic analysis of the measured pressure histories has been carried out to infer the rate of volume displacement and the total volume displaced by the secondary combustion. The results of the acoustic analysis are in reasonable agreement with both a simplified thermodynamic model predicting the total volume displacement assuming constant-pressure combustion for the secondary burn and the analysis of the fireball luminosity of the high-speed images.

For nearly stoichiometric mixtures, $\Phi = 1$ and 1.5, the leading blast wave peak pressures and impulses are comparable with the previously-measured gaseous and high explosive blasts when the energy content of the balloon only is used to formulate Sachs scaling variables. Due to a much slower combustion process than detonation for $\Phi > 2$ the peak pressure of the leading wave rapidly decreases below the energy-equivalent reference blast values as the equivalence ratio is increased. The Sachs-scaled impulse agrees well with the predictions on the basis of the energy in the balloon alone for $2.75 > \Phi > 1$.

One of the key results of the present study has been the documentation of the existence

of the secondary pressure wave. The present study has emphasized the acoustic nature of the secondary pressure waves and the origin of these pressure waves due to the processes at the interface between the fireball and the atmosphere. The presence of the secondary pressure peak and the higher impulses indicate that there is the potential for significant enhancement of the blast through secondary combustion.

Contents

Abstract i

List of Figures v

List of Tables xi

1 Introduction 1

2 Experimental Setup 3

3 Results 7
- 3.1 Initiator Characterization . . . 7
- 3.2 Propane-oxygen Initiator Mixture . . . 7
- 3.3 Sachs-scaled Results . . . 12
- 3.4 Acetylene-oxygen Initiator Mixture . . . 19
- 3.5 Initiation Location . . . 20
- 3.6 Analysis of Secondary Combustion Process . . . 25
- 3.7 Acoustic Approach to Secondary Combustion . . . 30
- 3.8 High-speed camera imaging . . . 36

4 Conclusions 41
- 4.1 Future Directions . . . 43

Bibliography 45

A Plots 47
- A.1 Peak pressure . . . 47
- A.2 Impulse . . . 50
- A.3 Time to Secondary Pressure Peak . . . 52
- A.4 Pressure traces . . . 53
- A.5 Species shift during expansion . . . 55
- A.6 Pencil gauge calibration . . . 57

B Highspeed movies 59

C Shotlist 87

D Initial balloon shape 89

List of Figures

1 Major products calculated for a constant volume combustion for a propane-oxygen mixture as a function of the equivalence ratio. 3
2 Initiation locations 3
3 Detailed drawing of initiator tube and set-up 4
4 Schematic of plumbing for balloon filling procedure. 5
5 Plan view of blast room with location of fire ball center and blast pencil gauges. 5
6 Photograph of actual test rig 6
7 Example pressure traces of experiment with initiator charge only . . . 7
8 Pressure traces obtained from the pencil gauges at 0.6 and 1.2 m. . . . 9
9 Peak pressure measured for C_3H_8-O_2 initiator mixture. 10
10 Mach number obtained from shock jump conditions for C_3H_8-O_2 initiator mixture. 10
11 Delay between blast wave and secondary pressure peak for C_3H_8-O_2 initiator mixture. Center initiation location. 11
12 Maximum positive impulse obtained from integrating the pressure trace. C_3H_8-O_2 initiator mixture. Center initiation location. 11
13 Point in time at which the maximum positive impulse (Fig. 12) occurs. C_3H_8-O_2 initiator mixture. Center initiation location. 11
14 Delay between blast wave and secondary pressure peak for C_3H_8-O_2 and C_2H_2-O_2 initiator mixture. Center initiation location. 11
15 Amount of fuel and oxidizer for different equivalence ratios. 13
16 Balloon charge energies for varying equivalence ratio. 13
17 Ratio for temperature and number of moles of reactants to expanded products as a function of equivalence ratio. 14
18 Sachs-scaled peak pressure vs. distance based on energy content E_1. C_3H_8-O_2 initiator mixture. Center initiation location. 14
19 Sachs-scaled impulse based on E_1 vs. distance. C_3H_8-O_2 initiator mixture. Center initiation location. 14
20 Sachs-scaled impulse based on E_2 vs. distance based on energy content E_2. C_3H_8-O_2 initiator mixture. Center initiation location. 14
21 Peak pressure of blast wave vs. equivalence ratio for stoichiometric C_2H_2-O_2 and C_3H_8-O_2 initiator mixtures. Center initiation location. . 20
22 Mach number of blast wave derived from shock jump conditions for stoichiometric C_2H_2-O_2 and C_3H_8-O_2 initiator mixtures. Center initiation location. 20
23 Comparison of Sachs' E_1-scaled blast wave peak pressure vs. scaled distance for the C_2H_2-O_2 initiator mixture. Center initiation location. Gauge locations: 0.6 m and 1.2 m. 21

24 Peak blast wave pressure and peak pressure of secondary pressure rise vs. equivalence ratio for stoichiometric C_2H_2-O_2 initiator mixture. Center initiation location. . . . 21
25 Comparison of blast wave pressure and peak pressure of secondary pressure rise for C_2H_2-O_2 and C_3H_8-O_2 initiator mixtures. Center initiation location. Gauge location: 0.6 m. . . . 21
26 Comparison of blast wave pressure and peak pressure of secondary pressure rise for C_2H_2-O_2 and C_3H_8-O_2 initiator mixtures. Center initiation location. Gauge location: 1.2 m. . . . 21
27 Impulse for C_2H_2-O_2 and C_3H_8-O_2 initiator mixture. Center initiation location. . . . 22
28 Comparison of secondary wave peak time for C_2H_2-O_2 and C_3H_8-O_2 initiator mixtures. Center initiation location. Gauge location: 0.6 m. . 22
29 Comparison of blast wave pressure for center and bottom initiation locations. C_2H_2-O_2 initiator mixture. . . . 23
30 Comparison of Mach number derived from the shock jump condition for center and bottom initiation locations. C_2H_2-O_2 initiator mixture. 23
31 Comparison of blast wave pressure and peak pressure of secondary pressure rise for center and bottom initiation locations. C_2H_2-O_2 initiator mixture. Gauge location: 0.6 m. . . . 23
32 Comparison of blast wave pressure and peak pressure of secondary pressure rise for center and bottom initiation locations. C_2H_2-O_2 initiator mixture. Gauge location: 1.2 m. . . . 23
33 Comparison of impulse derived from pressure traces for center and bottom initiation locations. C_2H_2-O_2 initiator mixture. . . . 24
34 Comparison of point in time at which maximum impulse occurs for center and bottom initiation locations. C_2H_2-O_2 initiator mixture. . . 24
35 Delay between blast wave peak pressure and peak pressure of secondary pressure rise for center (c) and bottom (b) initiation locations. C_2H_2-O_2 initiator mixture. . . . 24
36 Comparison of the E_1-Sachs-scaled impulse derived from pressure traces for center and bottom initiation locations. C_2H_2-O_2 initiator mixture. 24
37 Schematic of model process used to analyze the primary and secondary combustion events. . . . 25
38 Major products of state 1 and state 2 calculated for a constant volume combustion for a propane-oxygen mixture as a function of the equivalence ratio. . . . 27
39 Thermodynamic properties of state 1 calculated for a constant volume combustion for a propane-oxygen mixture as a function of the equivalence ratio. . . . 27
40 Shift in major species for chemically-equilibrated isentropic expansion to atmospheric pressure calculated for Φ=1. . . . 27

41 Volume-temperature relationship for chemically-equilibrated isentropic expansion to atmospheric pressure calculated for different equivalence ratios of the primary combustion. 27
42 Volume-temperature relationship illustrating the dependence of heat capacity ratios on equivalence ratio. 29
43 Temperature at states 3 and 4. 29
44 Specific volume at states 3 and 4. 29
45 Volumes calculated for different states in the model cycle based on the 1.5 l charge as a function of initial equivalence ratio. 29
46 Volume displacement rate calculated from Eq. 7 using the pressure history obtained at 0.6 m. Shot 106, $\Phi = 2.5$. 32
47 Volume displacement rate calculated from Eq. 7 using the pressure history obtained at 0.6 m. Shot 106, $\Phi = 2.5$. 32
48 Volume displacement rate calculated from Eq. 7 for both gauge locations. 32
49 Shot 174, $\Phi = 2.5$. Volume displacement rate calculated from Eq. 7 using the pressure history obtained at 0.6 m. 33
50 Volume displacement rate calculated from Eq. 7 using the pressure history obtained at 1.2 m. Shot 174, $\Phi = 2.5$. 33
51 Volume displacement rate calculated from Eq. 7 for both gauge locations. Shot 174 and 175, both $\Phi = 2.5$. 33
52 Volume displacement ΔV derived from integrating the volume displacement rate Q shown in Fig. 51 and Fig. 48. $\Phi = 2.5$, C_3H_8-O_2 and C_2H_2-O_2 initiator mixture. 35
53 Volume displacement ΔV derived from integrating the volume displacement rate Q shown in Fig. 51 and integrated volume of fireball from high speed video. Shot 106. $\Phi = 2.5$, C_3H_8-O_2 initiator mixture. The delay time of R/c is included. 35
54 Luminous volume of fireball determined by analyzing the high-speed video for shots at several different equivalence ratios. C_3H_8-O_2 initiator mixture. 35
55 Sequence of high-speed movie for $\Phi = 1.5$ (shot 111).The complete sequences for all high-speed movies is shown in Sec. B. 36
56 Luminosity derived from high-speed videos by averaging the luminosity of each frame and normalizing by the peak luminosity. 38
57 Transit time Δt that a blast wave needs to travel from the balloon edge (0.07 m) to the gauge located at 0.6 m and 1.2 m as a function of the blast wave peak pressure measured at the corresponding gauges. . . . 39
A.1.1 Peak pressure for C_3H_8-O_2 initiator. Center initiation location. 47
A.1.2 Peak pressure for C_3H_8-O_2 initiator. Center initiation location. 47
A.1.3 Peak pressure for C_3H_8-O_2 initiator. Center initiation location. 47
A.1.4 Peak pressure for C_2H_2-O_2 initiator. Center initiation location. 47
A.1.5 Peak pressure for C_3H_8-O_2 and C_2H_2-O_2 initiator. 0.6 m. Center initiation location. 48

A.1.6 Peak pressure for C_3H_8-O_2 and C_2H_2-O_2 initiator. 1.2 m. Center initiation location. . . . 48
A.1.7 Peak pressure for center and bottom initiation location. 0.6 m. C_2H_2-O_2 initiator mixture. . . . 48
A.1.8 Peak pressure for center and bottom initiation location. 1.2 m. C_2H_2-O_2 initiator mixture. . . . 48
A.1.9 E_1-Sachs-scaled impulse for both initiator mixtures versus Sachs-scaled distance. Center initiation location. . . . 49
A.1.10 E_1-Sachs-scaled peak pressure for center and bottom initiation location versus Sachs-scaled distance. C_2H_2-O_2 initiator mixture. . . . 49
A.1.11 E_2-Sachs-scaled impulse for both initiator mixtures versus Sachs-scaled distance. Center initiation location. . . . 49
A.1.12 E_2-Sachs-scaled peak pressure for center and bottom initiation location versus Sachs-scaled distance. C_2H_2-O_2 initiator mixture. . . . 49
A.2.1 Impulse for both initiator mixtures versus equivalence ratio. Center initiation location. . . . 50
A.2.2 Maximum impulse point in time for both initiator mixtures versus equivalence ratio. Center initiation location. . . . 50
A.2.3 Impulse for both initiation locations versus equivalence ratio. C_2H_2-O_2 initiator mixture. . . . 50
A.2.4 Maximum impulse point in time for both initiation lo actions versus equivalence ratio. C_2H_2-O_2 initiator mixture. . . . 50
A.2.5 E_1-Sachs-scaled impulse for both initiator mixtures versus Sachs-scaled distance. Center initiation location. . . . 51
A.2.6 E_2-Sachs-scaled impulse for both initiator mixtures versus Sachs-scaled distance. Center initiation location. . . . 51
A.2.7 E_1-Sachs-scaled impulse for center and bottom initiation location versus Sachs-scaled distance. C_2H_2-O_2 initiator mixture. . . . 51
A.2.8 E_2-Sachs-scaled impulse for center and bottom initiation location versus Sachs-scaled distance. C_2H_2-O_2 initiator mixture. . . . 51
A.3.1 Time to secondary pressure peak for both initiator mixtures versus equivalence ratio. Center initiation location. . . . 52
A.3.2 Time to secondary pressure peak for both initiation locations versus equivalence ratio. C_2H_2-O_2 initiator mixture. . . . 52
A.4.1 Examples of pressure traces for replica tests obtained from the pencil gauge at 0.6 m. C_3H_8-O_2 initiator mixture. Center initiation location. 53
A.4.2 Examples of pressure traces for replica tests obtained from the pencil gauge at 1.2 m. C_3H_8-O_2 initiator. Center initiation location. . . . 54
A.5.1 Pressure-volume relationship for chemically-equilibrated isentropic expansion to atmospheric pressure calculated for different equivalence ratios of the primary combustion. . . . 55
A.5.2 Shift in OH and H mole fraction for chemically-equilibrated isentropic expansion from state 1 to state 2 to atmospheric pressure. . . . 55

A.5.3 Shift in O_2 and O mole fraction for chemically-equilibrated isentropic expansion from state 1 to state 2 to atmospheric pressure. Note that Φ only ranges from 1 to 2. 55
A.5.4 Shift in major species for chemically-equilibrated isentropic expansion from state 1 to state 2 to atmospheric pressure calculated for Φ=1. . . 55
A.5.5 Shift in major species for chemically-equilibrated isentropic expansion from state 1 to state 2 to atmospheric pressure calculated for Φ=1.5. . 56
A.5.6 Shift in major species for chemically-equilibrated isentropic expansion from state 1 to state 2 to atmospheric pressure calculated for Φ=2. . . 56
A.5.7 Shift in major species for chemically-equilibrated isentropic expansion from state 1 to state 2 to atmospheric pressure calculated for Φ=2.5. . 56
A.5.8 Shift in major species for chemically-equilibrated isentropic expansion from state 1 to state 2 to atmospheric pressure calculated for Φ=3. . . 56
A.6.1 Calibration curves obtained from shock tube experiments for the two pencil gauges used. 57
B.1 Shot 113, frames 5 to 34, $\Phi = \mathbf{1}$. 60
B.2 Shot 113, frames 35 to 49, $\Phi = \mathbf{1}$. 61
B.3 Shot 113. Pressure traces from the pencil gauges located at 0.6 and 1.2 m. 61
B.4 Shot 110, frames 5 to 34, $\Phi = \mathbf{1.5}$ 62
B.5 Shot 110, frames 35 to 49, $\Phi = \mathbf{1.5}$. 63
B.6 Shot 110. Pressure traces from the pencil gauges located at 0.6 and 1.2 m. 63
B.7 Shot 111, frames 5 to 34, $\Phi = \mathbf{1.5}$ 64
B.8 Shot 111, frames 35 to 49, $\Phi = \mathbf{1.5}$. 65
B.9 Shot 111. Pressure traces from the pencil gauges located at 0.6 and 1.2 m. 65
B.10 Shot 112, frames 5 to 34, $\Phi = \mathbf{1.5}$. 66
B.11 Shot 112, frames 35 to 49, $\Phi = \mathbf{1.5}$. 67
B.12 Shot 112. Pressure traces from the pencil gauges located at 0.6 and 1.2 m. 67
B.13 Shot 107, frames 5 to 34, $\Phi = \mathbf{2}$. 68
B.14 Shot 107, frames 35 to 49, $\Phi = \mathbf{2}$. 69
B.15 Shot 107. Pressure traces from the pencil gauges located at 0.6 and 1.2 m. 69
B.16 Shot 108, frames 5 to 34, $\Phi = \mathbf{2}$. 70
B.17 Shot 108, frames 35 to 49, $\Phi = \mathbf{2}$. 71
B.18 Shot 108. Pressure traces from the pencil gauges located at 0.6 and 1.2 m. 71
B.19 Shot 109, frames 5 to 34, $\Phi = \mathbf{2}$. 72
B.20 Shot 109, frames 35 to 49, $\Phi = \mathbf{2}$. 73
B.21 Shot 109. Pressure traces from the pencil gauges located at 0.6 and 1.2 m. 73
B.22 Shot 103, frames 5 to 34, $\Phi = \mathbf{2.5}$. 74
B.23 Shot 103, frames 35 to 49, $\Phi = \mathbf{2.5}$. 75
B.24 Shot 103. Pressure traces from the pencil gauges located at 0.6 and 1.2 m. 75
B.25 Shot 104, frames 5 to 34, $\Phi = \mathbf{2.5}$. 76
B.26 Shot 104, frames 35 to 49, $\Phi = \mathbf{2.5}$. 77
B.27 Shot 104. Pressure traces from the pencil gauges located at 0.6 and 1.2 m. 77
B.28 Shot 105, frames 5 to 34, $\Phi = \mathbf{2.5}$. 78

B.29 Shot 105, frames 35 to 49, $\Phi = \mathbf{2.5}$. 79
B.30 Shot 105. Pressure traces from the pencil gauges located at 0.6 and 1.2 m. 79
B.31 Shot 106, frames 5 to 34, $\Phi = \mathbf{2.5}$. 80
B.32 Shot 106, frames 35 to 49, $\Phi = \mathbf{2.5}$. 81
B.33 Shot 106. Pressure traces from the pencil gauges located at 0.6 and 1.2 m. 81
B.34 Shot 114, frames 5 to 34, $\Phi = \mathbf{3}$. 82
B.35 Shot 114, frames 35 to 49, $\Phi = \mathbf{3}$. 83
B.36 Shot 114. Pressure traces from the pencil gauges located at 0.6 and 1.2 m. 83
B.37 Shot 115, frames 5 to 34, $\Phi = \mathbf{3}$. 84
B.38 Shot 115, frames 35 to 49, $\Phi = \mathbf{3}$. 85
B.39 Shot 115. Pressure traces from the pencil gauges located at 0.6 and 1.2 m. 85
D.1 Outline of balloon geometry 89

List of Tables

1 Volume calculated for different states in the modeled combustion process. 28
2 Shotlist. 87
3 Shot 109. Initial balloon outline coordinates are given in mm, where x is the horizontal axis. The initiator tube was located for the center initiation at the coordinate origin. 90
4 Shot 109. Initial balloon outline coordinates are given in mm, where x is the horizontal axis. The initiator tube was located for the center initiation at the coordinate origin. 91
5 Shot 114. Initial balloon outline coordinates are given in mm, where x is the horizontal axis. The initiator tube was located for the center initiation at the coordinate origin. 92

1 Introduction

We have carried out a series of experiments to study mixing and combustion of fireballs created by the rapid combustion of rich gaseous explosive mixtures. There are two combustion events in these experiments. A detonation is used to initiate the primary (initial) combustion event in propane-oxygen mixtures with equivalence ratios between one and three. The resulting fireball of combustion products expands and mixes with the surrounding air, which can result in a secondary combustion event. Blast pressures were measured at locations 0.6 m and 1.2 m from the center of the balloon containing the propane-oxygen mixture. The experiments are the first in a series of tests designed to study the role of fireball composition and gas dynamic interactions on secondary combustion.

The amount of energy released during the initial combustion event and the secondary reaction depends on the composition of the balloon mixture and the extent of the mixing and reaction of the resulting fireball with the surrounding air. Initially, the mixture inside the balloon was

$$\Phi \; C_3H_8 + 5\,O_2 \;\; ,$$

where the equivalence ratio is $1 < \Phi < 3$. For a stoichiometric mixture, $\Phi = 1$, complete combustion occurs during the initial event and the products are fully oxidized[1]

$$C_3H_8 + 5\,O_2 \longrightarrow 3\,CO_2 + 4\,H_2O \quad .$$

In this case, all the energy is released in the initial combustion event and no further reaction will take place upon mixing of the products with air. There is no secondary combustion event in this case.

[1]The products have been idealized in this reaction equations. Due to the high temperatures, 4000 K, a substantial amount of dissociation occurs and equilibrium computations indicate that H_2, CO, and O are presented in substantial amounts, as shown in Fig. 1

For $\Phi > 1$, the products of the initial combustion are incompletely oxidized and energy will be released both during the initial combustion event and the secondary event associated with the fireball. For example, at $\Phi = 3$, the initial combustion reaction can be approximately written as

$$3\,C_3H_8 + 5\,O_2 \longrightarrow 9\,CO + 11\,H_2 + H_2O \ .$$

As indicated, the partially oxidized species CO and H_2 are created by the initial combustion event in rich mixtures. As the equivalence ratio is increased, Fig. 1, an increasing amount of CO and H_2 is produced. When the fireball mixes with the surrounding air, these can be oxidized to CO_2 and H_2O,

$$CO + \tfrac{1}{2}\,O_2 \longrightarrow CO_2 \quad , \qquad H_2 + \tfrac{1}{2}\,O_2 \longrightarrow H_2O \ ,$$

releasing energy and creating pressure waves.

2 Experimental Setup

The propane-oxygen mixture is contained in a 1.5 liter (equivalent to a 140 mm diameter sphere) balloon. The volume of the balloon was held constant at 1.5 liter for all experiments. The fireball is initiated by a detonation defracting into the propane-oxygen mixture out of the initiator tube which emerges from below into the balloon, Fig. 3a. The balloon is made of natural rubber latex and, in the inflated state, the wall thickness is approximately 0.02 mm. The balloon is slightly bulb shaped, see Sec. D. The initiation location of the balloon mixture can be adjusted by sliding the balloon retainer vertically along the initiator tube. Two configurations are studied, Fig. 2: a) The initiator tube end is centered with respect to the balloon and b) The initiator tube end emerges into the bottom of the balloon. In order to prevent leaking of the balloon mixture, the balloon retainer is sealed with an O-ring against the initiator tube. The initiator tube has a total length of 440 mm and contains two sections, one of which is equipped with a

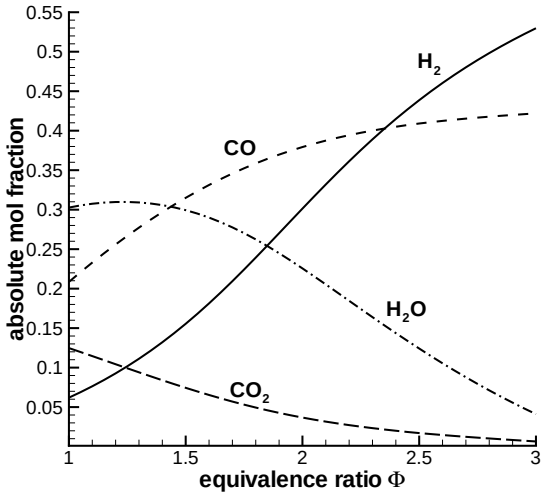

Figure 1: Major products calculated with an equilibrium solver (STANJAN) for a constant volume combustion for a propane-oxygen mixture as a function of the equivalence ratio. Initial temperature 294 K, Initial pressure 1.013 bar.

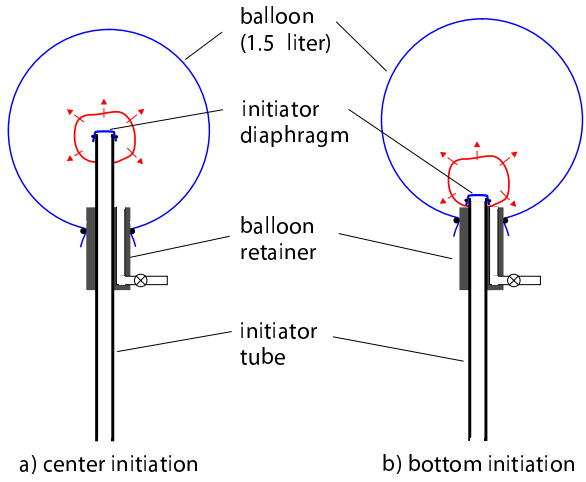

Figure 2: Two initiation locations were studied. The balloon retainer slides onto the initiator tube and was locked in position with a screw.

Shchelkin spiral in order to ensure transition to detonation within the tube, Fig. 3b. The initiator tube of volume 0.13 l was sealed with a 0.02 mm thick polyethylene diaphragm and then evacuated to 1 mbar prior to filling with a premixed initiator gas mixture to atmospheric pressure. Stoichiometric propane-oxygen or stoichiometric acetylene-oxygen mixtures were used in the initiator, labeled as C_3H_8 or C_2H_2 in the plot legends.

After filling the initiator, the balloon was attached and sealed with an elastic band to the balloon retainer. The remaining air inside the balloon was evacuated prior to filling

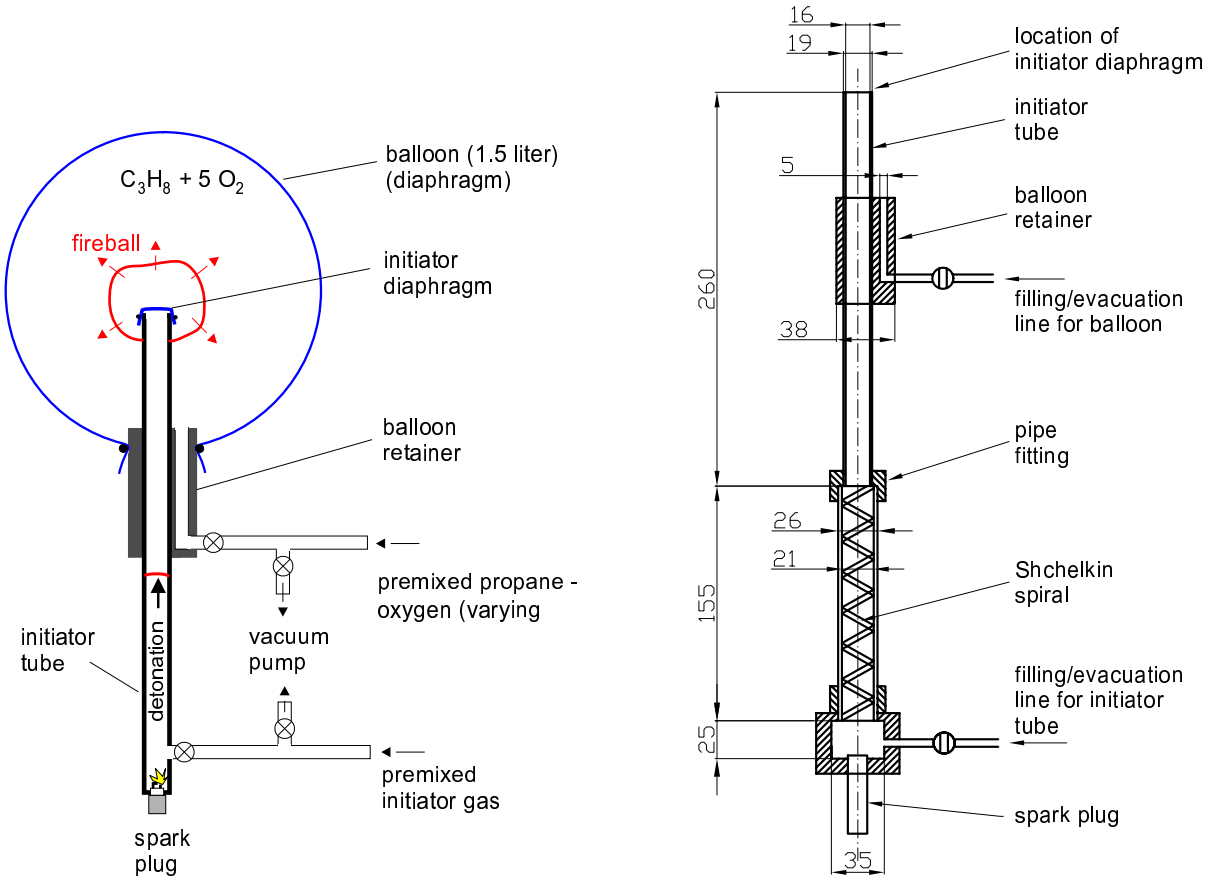

(a) Schematic of set-up

(b) Initiator tube

Figure 3: a) The initiator tube is sealed with an approximately 0.02 mm thick diaphragm. b) Detailed technical drawing of initiator tube. The dimensions are given in mm. The Shchelkin spiral has a pitch of approximately 25 mm, a wire diameter of 3 mm and an outer diameter equal to the inner tube diameter.

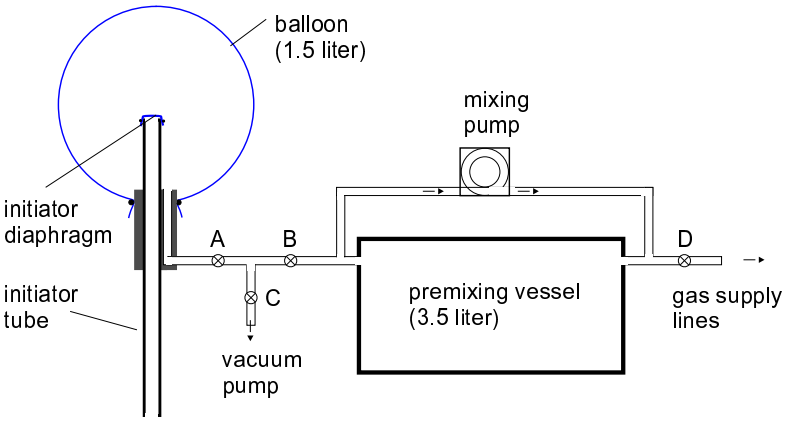

Figure 4: Schematic of plumbing for balloon filling procedure.

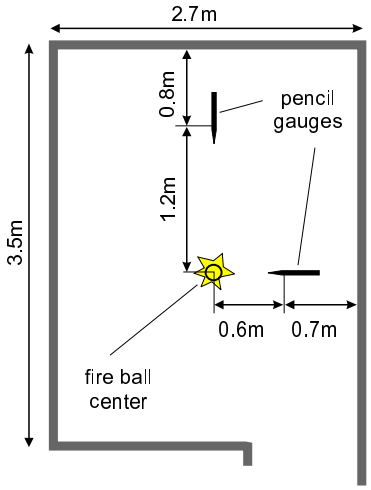

Figure 5: Plan view of blast room with location of fire ball center and blast pencil gauges.

the balloon by opening valve A and C, Fig. 4. Since the balloon is elastic, the method of partial pressures could not be applied directly to mix the propane and oxygen during the balloon filling. Instead, a vessel of volume 3.8 l was evacuated to 1 mbar by opening valve B and C and then filled with a premixed propane-oxygen mixture of the desired stoichiometric ratio by the method of partial pressures through valve D. The premixing vessel was filled to a final pressure of 1.5 bar and mixed by circulating the gas with a pump for five minutes. After preparation of the mixture, valves A and B were opened, letting the pressure in the balloon equilibrate close to atmospheric pressure. Due to tension, the internal pressure was measured to be 20 mbar above the surrounding atmospheric pressure. After the pressure equilibrated, the balloon itself contained a volume of 1.5 l considering the volume of the filling lines. Subsequently, all valves were closed. The leak rate of the balloon volume was measured to be less than 0.06 l/h, which results in a volume uncertainty of less than 0.5%, since the charge was initiated within five minutes after the filling procedure. A discharge system with a stored energy of 30 mJ was used to ignite the initiator mixture with the spark plug.

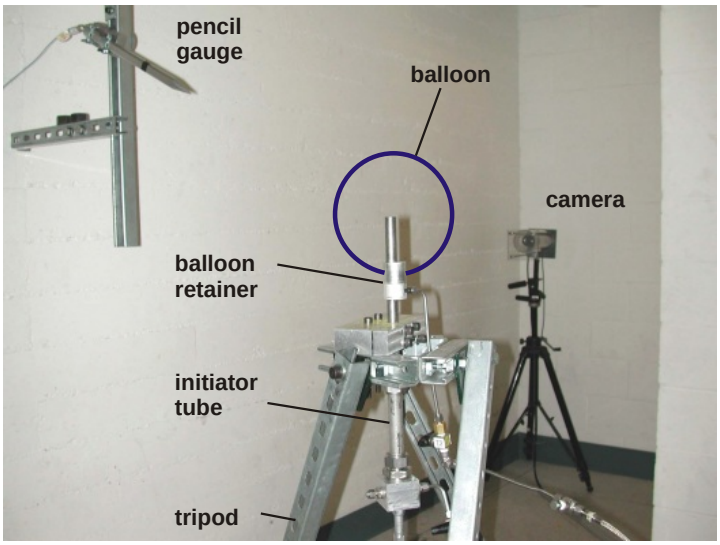

Figure 6: Photograph of actual test rig. The camera shown is for surveillance purposes during the balloon filling procedure only and is not the high speed camera, which is located outside this view.

The experiments were carried out in a 35 m^3 blast room. A plan view of the blast room and the location of the fireball center is shown in Fig. 5. The height of the room is approximately 3.5 m. The initiator and balloon are attached to a rigid tripod (Fig. 6) so that the fireball center is located 1.25 m above the ground. Two pencil gauges were located at a distance of 0.6 and 1.2 m from the fireball center at a height of 1.25 m above the ground in order to obtain the pressure history. The pressure transducers were PCB piezoelectric transducers (Model 137A23) with a rise time of 4 μs and a discharge time constant larger than 0.2 s. In order to prevent thermal effects on the piezoelectric transducers, the pencil gauge was covered with one layer of electrical tape. The pencil gauges are normally mounted the same height as the fireball center in a horizontal position (polar angle of 90°). For the initiator characterization, polar angles of 0° to 90° were investigated. The relative azimuthal angle between the pencil gauges was kept at 90°. A blast-shielded high speed camera (Phantom V) with a resolution of 256×256 pixels and 11200 frames per second was used for some shots to image the event.

3 Results

3.1 Initiator Characterization

A series of shots was conducted with the initiator diaphragm and charge only, i.e., without the balloon. The pressure traces showed a repeatable deflagration-to-detonation transition within the initiator tube, and the blast wave parameters measured were constant over the polar angle of 0° (vertical) to 90° (horizontal) and the azimuthal angle, Fig. 7. For this series of shots, the pencil gauges were located at a distance of 0.3 m, 0.6 m, and 1.2 m from the end of the initiator tube.

3.2 Propane-oxygen Initiator Mixture

A series of 48 shots was carried out using a stoichiometric propane-oxygen mixture in the initiator tube and a balloon filled with a propane-oxygen mixture. Using the center initiation location, a single leading peak in the pressure history (Fig. 8) is measured for a balloon charge equivalence ratio of up to 1.75. The time $t = 0$ in all plots corresponds to the point in time of ignition of the initiator mixture with the spark plug. The maximum blast wave peak pressure of 39 kPa at 0.6 m is observed for an equivalence ratio of 1.5. The values shown in Fig. 9 are the averages obtained from several experiments.

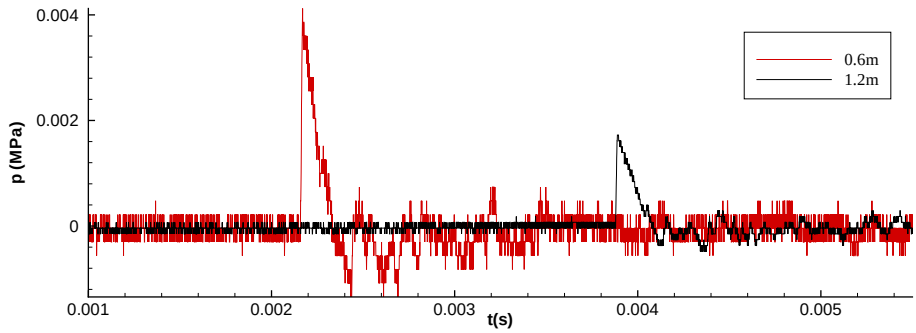

Figure 7: Pressure trace of experiment with initiator charge (stoichiometric propane-oxygen) only. Pencil gauges were located at 0.6 m and 1. 2m from fireball center.

Corresponding plots with error bars are shown in App. A.1. The shot-to-shot variations in peak pressure of the initial blast wave are also largest for an equivalence ratio of 1.5, Fig. A.1. For an equivalence ratio of 2 and higher, a secondary pressure peak is observed at both 0.6 m and 1.2 m from the fireball center. The secondary pressure peak occurs (Fig. 11) for an equivalence ratio of 2 at 0.6 ms after the initial blast wave, and for an equivalence ratio of 3, up to 3 ms after the primary blast. The larger error bars for the equivalence ratios 2, 2.5, and 3 reflect the larger number of replica experiments that have been conducted for these equivalence ratios. For an equivalence ratio of 3, the second pressure peak was sometimes difficult to determine since the secondary pressure rise was rather weak and occurred so late that it overlapped the wave reflected from the wall.

The secondary pressure rise is not due to the primary blast wave reflecting from the wall, which occurs at a later point in time. For the pencil gauge at 0.6 m, the reflected wave is observed at approximately 5.8 ms and, for the pencil gauge at 1.2 m, at approximately 8 ms, Fig. 8. This corresponds to a Mach number of approximately 1.01 for the reflected wave which agrees with the Mach number of the incident wave computed from the time of arrival of the blast wave at the pencil gauges and the shock jump conditions, Fig. 22. The labels (c) and (b) in the legend of all plots stand for center and bottom initiation location, respectively. The labels C_3H_8 or C_2H_2 describe the type of initiator mixture used. The secondary pulse measured for equivalence ratios 2 and 2.25 is associated with a sharp pressure rise or shock wave. This is an indication that a rapid explosion of a substantial volume of combustible mixture is taking place.

For $\Phi > 2.25$, the secondary pressure rise occurs more smoothly and does not exhibit shocks. This suggests that the secondary combustion occurs more slowly as Φ increases. The maximum secondary pressure rise occurs (Fig. 9) for an equivalence ratio of 2.25. For $\Phi > 2.25$, the secondary peak pressure occurs later in time and is gradually less pronounced. For $2.25 < \Phi < 2.75$, the peak pressure of the secondary rise exceeds the

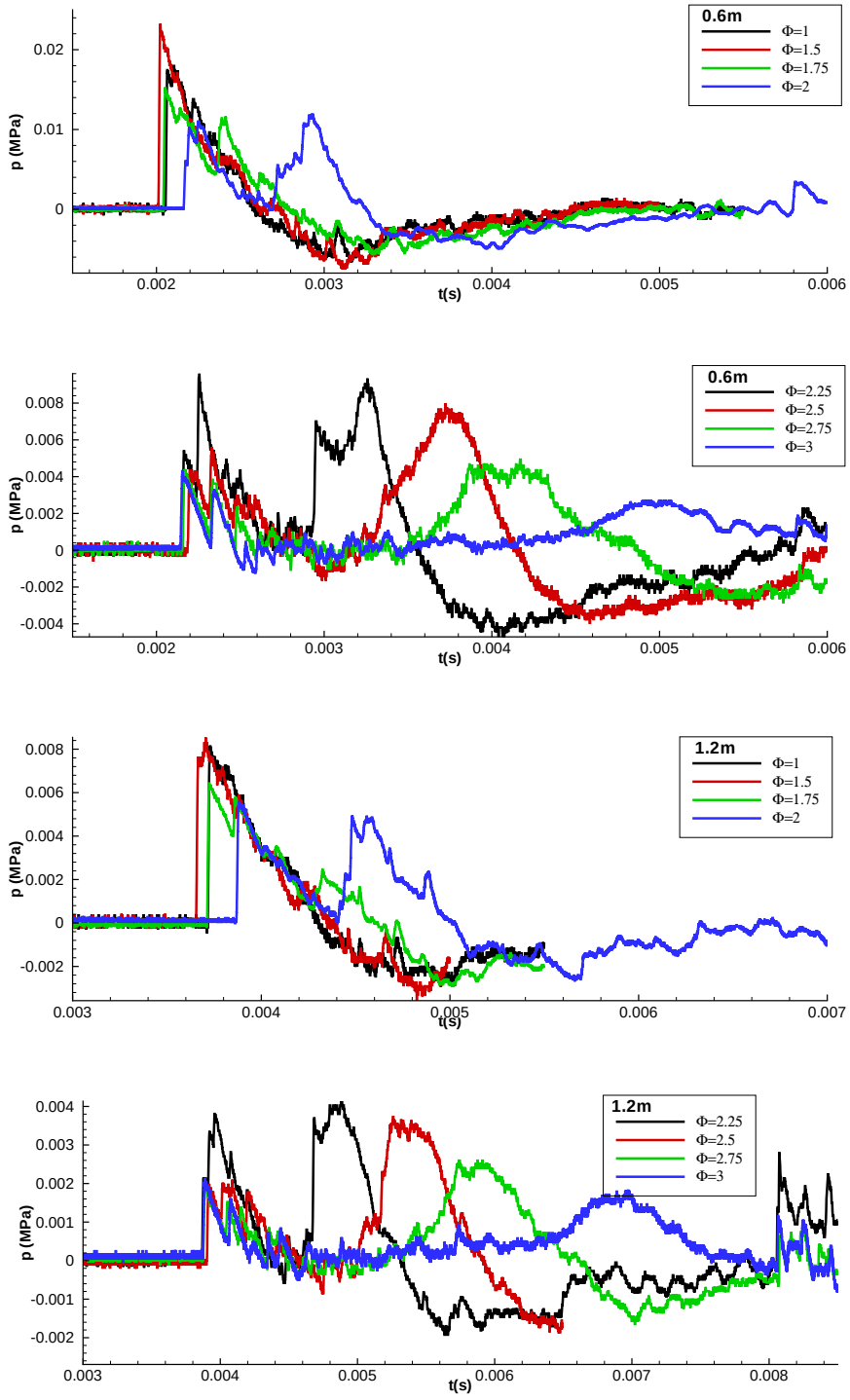

Figure 8: Pressure traces obtained from the pencil gauges at 0.6 and 1.2 m for several experiments at different equivalence ratio. The time $t = 0$ corresponds to the point in time of ignition of the initiator mixture with the spark plug.

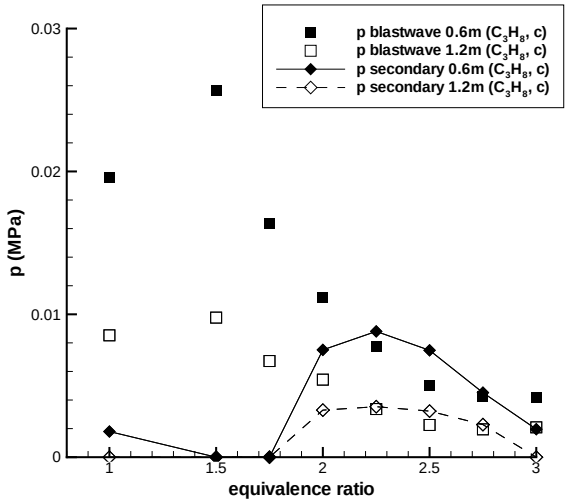

Figure 9: Peak pressure measured for C_3H_8-O_2 initiator mixture. For equivalence ratios up to 1.75, no secondary peak is observed, and, therefore the data point is set to 0.

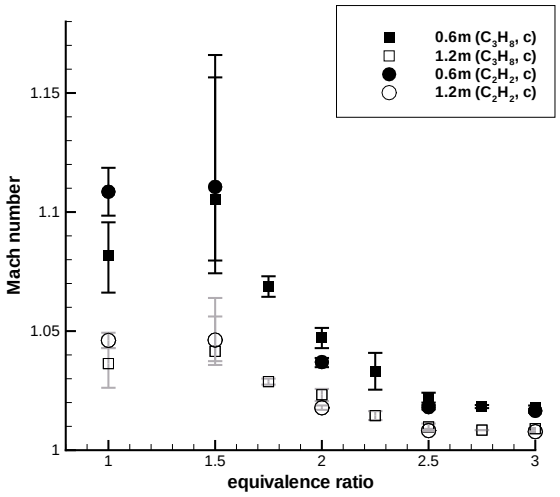

Figure 10: Mach number obtained from shock jump conditions for C_3H_8-O_2 initiator mixture.

peak pressure from the initial blast wave.

These tests show that the secondary pressure rise occurs in a repeatable fashion. Replica test pressure histories for the case of C_3H_8-O_2 initiator mixture and the center initiation location are shown in App. A.4. For equivalence ratios 1, 1.5, 2, 2.5, and 3, at least four replica tests were performed. The impulse, in units of Ns/m^2, was derived by integrating the pressure transducer signal over time and correcting for the slight initial off-set from the zero line for some pressure traces. The maximum value of the positive impulse, also referred to just as impulse in the following, was calculated by integrating the pressure traces to that point in time at which the integral is maximum, but not further than the point in time where the reflected wave occurs. The point in time at which the positive impulse is maximized corresponds to the beginning of the negative phase of the pressure trace. Due to the secondary pressure rise and the overlap of the reflected wave from the wall and the negative phase, meaningful values of the negative phase impulse could not be obtained. The maximum positive impulse for all cases is shown in Fig. 12.

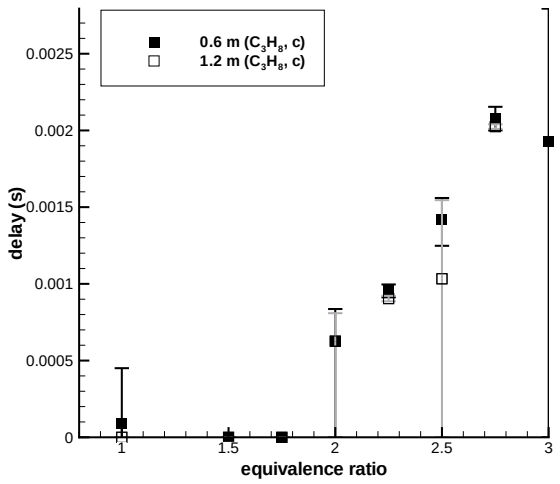

Figure 11: Delay between blast wave and secondary pressure peak for C_3H_8-O_2 initiator mixture. Center initiation location.

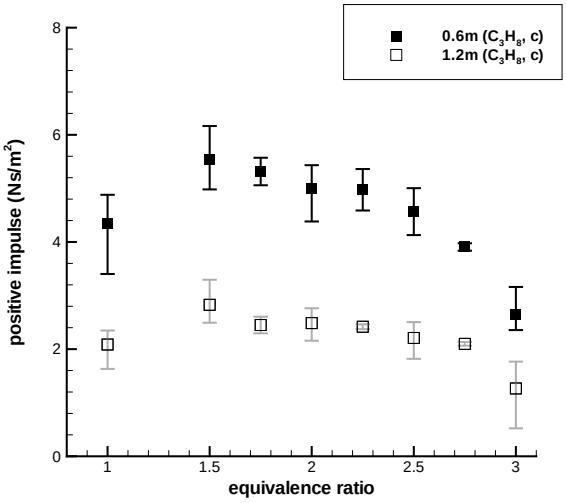

Figure 12: Maximum positive impulse obtained from integrating the pressure trace. C_3H_8-O_2 initiator mixture. Center initiation location.

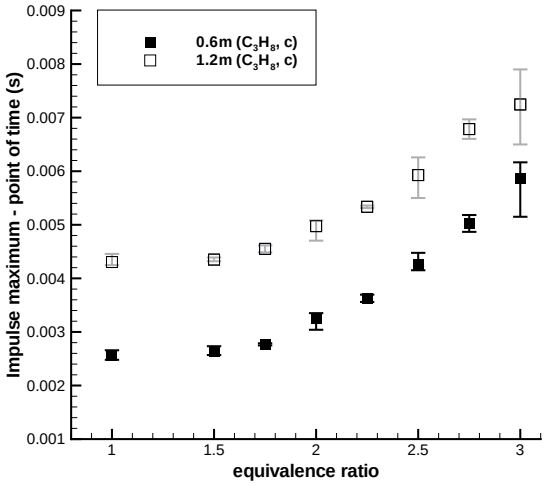

Figure 13: Point in time at which the maximum positive impulse (Fig. 12) occurs. C_3H_8-O_2 initiator mixture. Center initiation location.

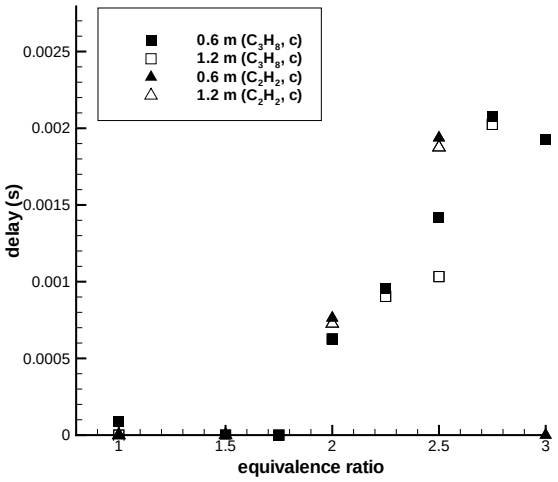

Figure 14: Delay between blast wave and secondary pressure peak for C_3H_8-O_2 and C_2H_2-O_2 initiator mixture. Center initiation location.

The maximum positive impulse reflects the impulse combined from the initial blast wave and the secondary pressure rise, in case it occurred. The maximum impulse is obtained for an equivalence ratio of 1.5 and measured to be 5.6 $\mathrm{Ns/m^2}$ at 0.6 m. Despite the secondary pressure rise for equivalence ratio 2, the maximum impulse is slightly lower than for $\Phi = 1.5$, approximately 4.8 $\mathrm{Ns/m^2}$. The impulse is 4.6 $\mathrm{Ns/m^2}$ for $\Phi = 2.5$ and falls off dramatically for equivalence ratios higher than 2.5. The lower values in maximum positive impulse for $\Phi = 3$ may also be due to the fact that the secondary pressure rise overlaps the reflected wave and is, therefore, not fully accounted for in the maximum impulse value. The impulse is decreasing with increasing equivalence ratio despite the larger amount of fuel (this is discussed further in Sec. 3.3). The secondary pressure rise does not compensate for the smaller impulse arising from the decreased initial blast wave magnitude.

The point in time at which the maximum positive impulse occurs is increasing with increasing equivalence ratio due to two effects: The secondary peak pressure occurs at a later point in time, Fig. 11, and the secondary peak is broader, both leading to a shift of the negative phase start towards a later point in time.

3.3 Sachs-scaled Results

To enable a comparison with other experiments, the experimental results can be presented using Sachs dimensionless variables described in AMC (1974). These are labeled here with a bar and defined as follows:

$$\text{distance} \quad \bar{R} = R \left(\frac{p_0}{E} \right)^{\frac{1}{3}} , \tag{1}$$

$$\text{pressure} \quad \bar{p} = \frac{p}{p_0} , \tag{2}$$

$$\text{impulse} \quad \bar{I} = \frac{I\, c_0}{p_0\, \bar{R}} = \frac{I\, c_0}{p_0^{\frac{2}{3}}\, E^{\frac{1}{3}}} , \tag{3}$$

where R is the distance from the charge, p_0 is the surrounding pressure, E is the energy equivalent of the charge, p is the blast wave peak pressure, and I is the impulse calculated by integrating either the positive or negative phase of the blast pressure trace. Here, only the positive phase is considered. Sachs scaling was developed to analyze blast waves from ideal explosives, for which the energy release is spatially concentrated, rapid, and usually has a well-defined value, at least for oxygen-balanced high explosives or nuclear weapons. In order to use Sachs scaling with the present problem, it is necessary to consider how to define the equivalent energy release for the propane-oxygen mixtures in the balloon.

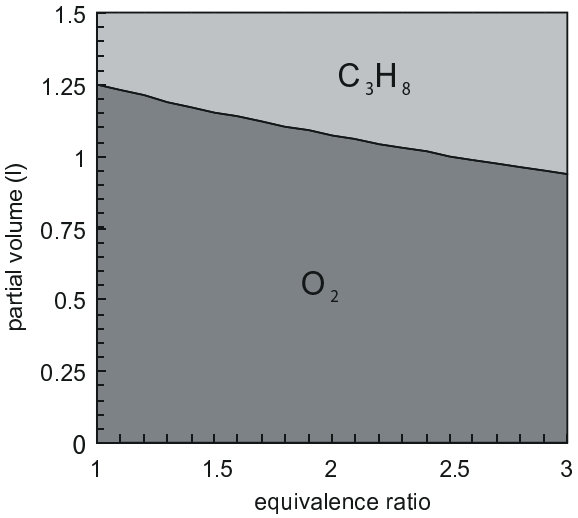

Figure 15: Amount of fuel and oxidizer for different equivalence ratios. The total volume is held constant at 1.5 l.

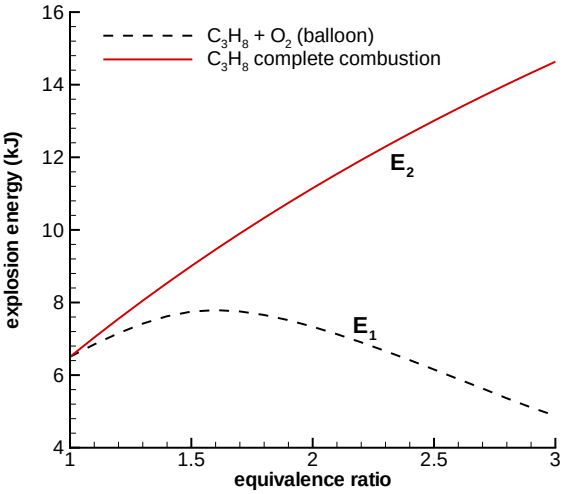

Figure 16: Balloon charge energies for varying equivalence ratio assuming only combustion with the supplied oxygen inside the balloon, E_1, and assuming complete combustion of the propane with oxygen supplied by the surrounding air, E_2.

The amount of fuel increases with increasing Φ since the volume of the charge is held constant, Fig. 15. The energy equivalent of the balloon is calculated as the energy difference between the reactants and the detonation products expanded to atmospheric pressure. This is different than the procedure followed in high explosives, Baker et al. (1980), or detonation of fuel-air mixtures, Dorofeev et al. (1995b). In those cases, the

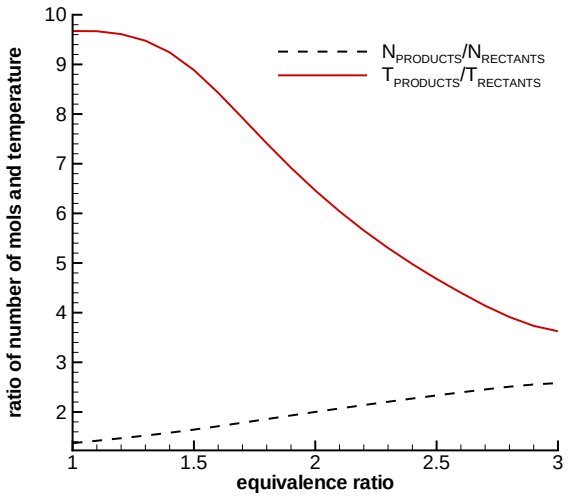

Figure 17: Ratio for temperature and number of moles of reactants to expanded products as a function of equivalence ratio.

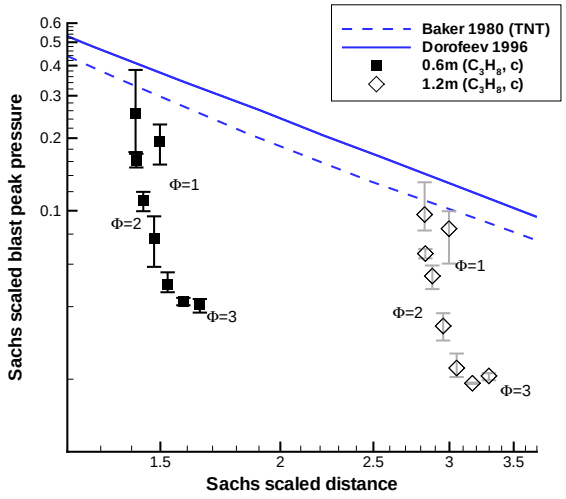

Figure 18: Sachs-scaled peak pressure vs. distance based on energy content E_1. The Sachs-scaled data of Dorofeev et al. (1995b) is based on the corresponding E_1 for their charge. C_3H_8-O_2 initiator mixture. Center initiation location.

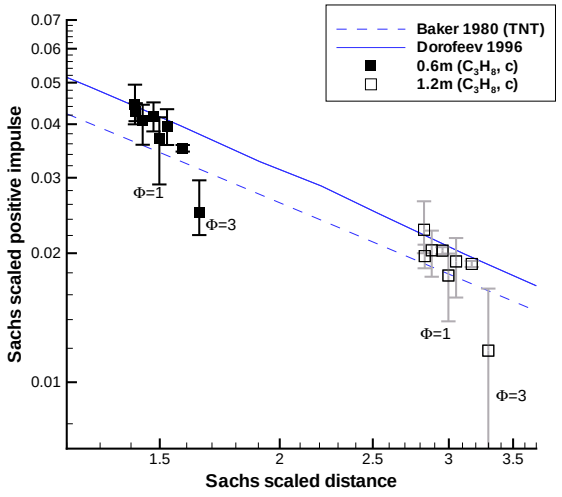

Figure 19: Sachs-scaled impulse based on E_1 vs. distance. C_3H_8-O_2 initiator mixture. Center initiation location.

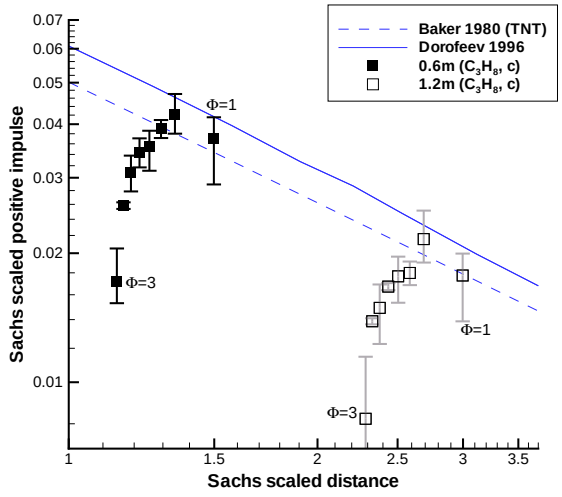

Figure 20: Sachs-scaled impulse based on E_2 vs. distance based on energy content E_2. C_3H_8-O_2 initiator mixture. Center initiation location.

equivalent energy is computed by multiplying the mass of mixture with the heat of combustion, which is calculated as the difference in enthalpy between the reactants and products at standard temperature (25°C) and pressure (1 atm). In fact, it is known that only a fraction of the heat of combustion goes into producing the blast wave since the products are still quite hot after expanding to atmospheric pressure but before mixing with the surrounding air. This effect is particularly important for fuel-oxygen mixtures which are highly dissociated and much less efficient than fuel-air mixtures at creating blast waves. To account for this, we have adopted the present procedure, which is similar to the method used for computing the blast energy equivalent for pressurized vessels, see the discussion on pp. 185–199 of AIChE (1994). For a stoichiometric propane-oxygen mixture, the revised procedure predicts an energy content of 3.1 MJ/kg as compared to 10 MJ/kg predicted by using the conventional heat of combustion technique. By contrast, the energy content of a stoichiometric propane-air mixture is predicted to be 1.3 MJ/kg as compared to 2.8 MJ/kg predicted by the conventional method. The revised method predicts that 31% of the propane-oxygen mixtures chemical energy can be converted to mechanical work versus 46% for the propane-air mixture. In order to use the revised energy equivalence with Dorofeev's data, we have recomputed the Sachs-scaled variables and developed revised correlations for both peak pressure and impulse. On the other hand, we have used the original (Baker) correlation for the Sachs scaling of blast waves from TNT. We have not attempted to revise this correlation since there is significant uncertainty about the TNT energy equivalence due to the oxygen deficit in this explosive. In addition, computations with other high explosives (Fickett and Davis (1979))show that high explosives are much more efficient - up to 98 % for RDX - in converting chemical energy to mechanical work. To summarize: The Sachs scaling correlations presented in this work are based on the energy difference between the reactants and products of a detonation expanded to atmospheric pressure. The original data of Dorofeev et al.

(1995b) on fuel-air mixtures have been re-reduced to obtain a correlation on this basis but the high explosive-based correlation of Baker et al. (1980) has been used without any change.

The energy content is clearly defined only for the stoichiometric case. For rich mixtures, there is a range of values depending on how much of the mixing and combustion of the fireball contributes to blast pressure. Two extreme values can be computed. The smallest value, E_1, is obtained if we assume no mixing and combustion of the fireball with surrounding air. E_1 corresponds to incomplete oxidation of the fuel and decreasing temperature after the expansion for increasing equivalence ratio from 2900 K at $\Phi = 1$ to 1090 K at $\Phi = 3$. The number of moles of products created by combustion increases with increasing equivalence ratio (Fig. 17). Due to the modest decrease in temperature till $\Phi = 1.5$, E_1 increases (Fig. 16) from 6.5 kJ at $\Phi = 1$ to 7.7 kJ at $\Phi = 1.5$. For $\Phi > 1.5$ the strong decrease in temperature with increasing equivalence ratio dominates and E_1 decreases to 4.9 kJ at $\Phi = 3$. The largest value, E_2, is obtained if we assume complete mixing and combustion of the fuel with the surrounding air. This results in complete oxidation of the fuel and the total energy release, E_2, increases (Fig. 16) with increasing equivalence ratio, from 6.5 kJ at $\Phi = 1$ to 15 kJ for $\Phi = 3$. The energy equivalent calculated based on the differences in energy is for $\Phi = 1$ approximately 30% of the energy equivalent calculated based on the differences in enthalpy in a constant pressure combustion, 22 MJ.

Experiments by previous researchers have been carried out with gaseous and condensed explosives to define blast relationships in Sachs variables. Experiments on high explosives are described by AMC (1974) and Baker et al. (1980); experiments on the detonation of gaseous explosives are described in Dorofeev et al. (1995b) and Moen et al. (1983). Although detonation of high explosives and gaseous show differences in the *near field*, $\bar{R} < 1$, the far field results, $\bar{R} \gg 1$, show a universal dependence of the scaled

impulse and peak pressure on the scaled distance. For a given atmospheric pressure, the net energy release E is the only property of an ideal explosive that is needed to determine the blast effects at any distance. This leads to the concept of TNT equivalence that is widely used in the explosion hazards community to evaluate the consequences of accidental explosions, see AIChE (1994). On the other hand, low speed combustion or deflagration of gaseous explosives results in very different blast waves than a detonation, and the blast properties do not follow a universal relationship when expressed in terms of Sachs scaling. As discussed in AIChE (1994), many factors other than equivalent energy release are important and the blast pressure is a strong function of the speed of combustion for non ideal explosives.

The peak pressures from the present experiments are compared using Sachs scaling in Fig. 18 to the known high explosive (Baker 1980) and gaseous (Dorofeev 1996) detonation results, revised as discussed above. Due to the very non ideal nature of the initial explosion for all cases other than $\Phi = 1$, the Sachs-scaled peak pressure based on E_1 drops far below the curves obtained by Baker and Dorofeev for $\Phi > 1.5$ at both 0.6 and 1.2 m. Due to the maximum value of E_1 for $\Phi = 1.5$, the Sachs-scaled distance for the gauge locations at 0.6 and 1.2 decreases slightly for $\Phi < 1.5$ and increases for $\Phi > 1.5$ with increasing equivalence ratio. The previous work that is most closely related to the present study is the experiments of Dorofeev et al. (1995b), who investigated the detonation of rich fuel-air mixtures. Dorofeev et al. (1995b) used a large scale experiment with a hemispheric plastic envelope (4 m in radius) filled with propane-air mixtures with $1 < \Phi < 1.8$. No secondary pressure rise was observed in these experiments, presumably due to the lack of fuel in the initial combustion products. The Sachs-scaled data from Dorofeev et al. (1995b) shown here are rescaled based on an energy content of 420 MJ, which was calculated in two steps: First the energy difference of reactants and expanded products for the rich fuel-air mixtures used by Dorofeev et al. (1995b) was calculated as

described above to be approximately 210 MJ. Secondly, to take into account that the data of Dorofeev et al. (1995b) were obtained from a surface blast experiment the energy equivalent was doubled in order to compare it with the air blast experiments.

The Sachs-scaled peak pressure measured at the 0.6 m gauge location for $\Phi = 1.5$ is 20% below the blast wave pressure measured by Baker et al. (1980) for TNT air bursts and does not exceed the TNT air burst data for any equivalence ratio. The agreement is better for the stronger initiator used, Fig. A.1.9. The Sachs-scaled peak pressure measured at the 1.2 m gauge location agrees for an equivalence ratio of 1.5 with the TNT data of Baker et al. (1980) and remains for all other equivalence ratios below the peak pressure for the TNT surface burst. This is consistent with the trend seen in the data of Dorofeev et al. (1995b) and Moen et al. (1983) compared to the TNT blast peak pressure. Moen et al. detonated a gaseous mixture in a horizontal cylindrical bag of volume up to 110 m^3 in the immediate vicinity of the ground. For Sachs-scaled distances smaller than approximately 1, they found that the scaled peak pressure approaches the blast parameters for the TNT air burst. For larger Sachs-scaled distances, the scaled blast wave pressure from gaseous fuel-air explosives approaches the scaled peak pressure of the TNT surface charge.

The Sachs-scaled impulse based on E_1 is in fairly good agreement with the data from Dorofeev et al. (1995b) for $\Phi < 2.5$. The scaled peak pressure drops far below Dorofeev's values with increasing equivalence ratio $\Phi > 1.5$ based on either E_1 or E_2. Apparently for $\Phi > 1.5$, the charges do not react sufficiently fast to achieve blast pressures consistent with the energy equivalence. If the balloon mixtures are sufficiently rich, the detonation may fail to transit from the initiator tube to the balloon, and a much lower speed combustion wave will occur. It is known (Baker and Tang, 1994, Tang and Baker, 1999) that the energy equivalence method substantially overpredicts the blast pressures for low-speed flames. As the flame speed decreases below Mach numbers of about 3,

numerical simulations (Tang and Baker, 1999) predict that both the peak pressure and positive impulse decrease for a given value of E_1. For a flame Mach number of 0.2 (about 60 m/s), the scaled peak pressures are about 1/10 of the values given by the high explosive or gaseous detonation blast scaling. This is consistent with the peak pressures observed (Fig. 18) for $\Phi = 3$.

The secondary combustion does create an additional increments to the impulse, but the E_2-scaled impulse is lower (Fig. 20) than Dorofeev's values of impulse. Numerical simulations (Tang and Baker 1999) indicate that the scaled impulse in the far field, $\bar{R} > 0.5$, is much less sensitive to the flame speed, which is consistent with the results of Fig. 19.

3.4 Acetylene-oxygen Initiator Mixture

Using stoichiometric C_2H_2-O_2 instead of stoichiometric C_3H_8-O_2 as the initiator tube mixture results in a stronger initiation process. The Chapman-Jouguet velocity in stoichiometric C_2H_2-O_2 is 2720 m/s as compared to 2360 m/s for the stoichiometric C_3H_8-O_2. The Chapman-Jouguet pressures are 4.18 MPa and 3.69 MPa, respectively. In comparison to using C_3H_8-O_2 as the initiator gas, the peak pressure for an equivalence ratio 1 and 1.5 is increased by using C_2H_2-O_2 and decreased for equivalence ratios of 2 and higher, Fig. 21. The maximum blast peak pressure is obtained for an equivalence ratio of 1.5. The results for peak blast and secondary pressure and positive impulse are very similar (Figs. 21-28) for the two initiation mixtures, with a few exceptions.

For $\Phi = 1$, the stronger initiator results in an increase (Fig. 27) in maximum impulse measured at 0.6 m of about 30% and at 1.2 m of about 15% compared to the weaker initiator. For equivalence ratios 1.5 and 2, the positive impulse is 10% higher for the C_2H_2 initiator. For $\Phi = 1.5$, this is due to the increased blast wave strength and for $\Phi = 2$, this is due to the increase in the secondary pressure rise. The time between the

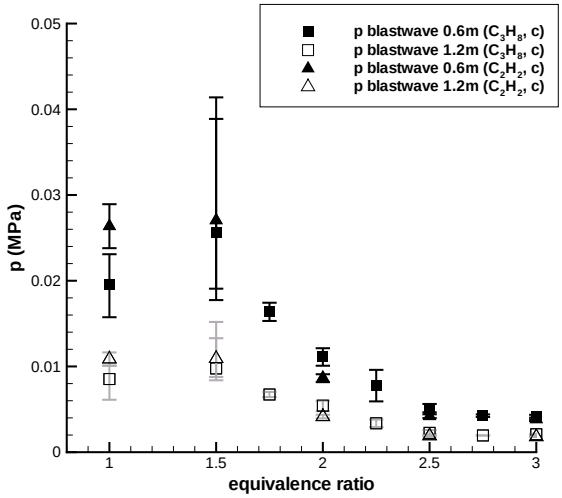

Figure 21: Peak pressure of blast wave vs. equivalence ratio for stoichiometric C_2H_2-O_2 and C_3H_8-O_2 initiator mixtures. Center initiation location.

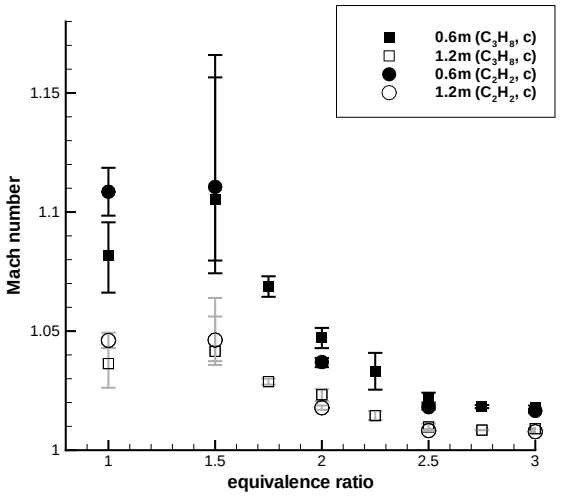

Figure 22: Mach number of blast wave derived from shock jump conditions for stoichiometric C_2H_2-O_2 and C_3H_8-O_2 initiator mixtures. Center initiation location.

blast peak pressure and the secondary peak pressure is not affected by the change in initiator mixture except for an equivalence ratio of 2.5, (Fig. 14), where the secondary peak pressure occurs 2 ms after the blast wave peak, compared to 1.5 ms (0.6 m) and 1 ms (1.2 m) after the blast wave peak pressure for the propane-oxygen initiator mixture.

3.5 Initiation Location

The initiation location of the balloon charge was investigated by moving the balloon retainer towards the end of the initiator tube. This placed the end of the initiator tube 6 mm above the bottom of the balloon, Fig. 2. The entire assembly was then lowered so that the location of the balloon center with respect to the pencil gauges was unaltered. For all experiments conducted with the bottom initiation location, the stronger C_2H_2-O_2 initiator mixture was used.

For equivalence ratios of 1 and 1.5, the peak pressure of the blast wave is higher for the bottom initiation location than for the center initiation location. The maximum

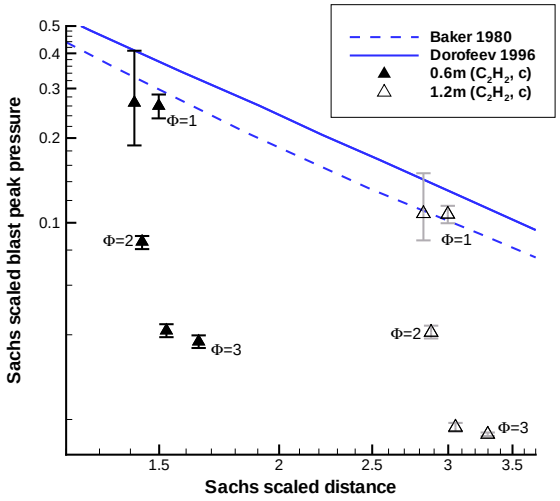

Figure 23: Comparison of Sachs' E_1-scaled blast wave peak pressure vs. scaled distance for the C_2H_2-O_2 initiator mixture. Center initiation location. Gauge locations: 0.6 m and 1.2 m.

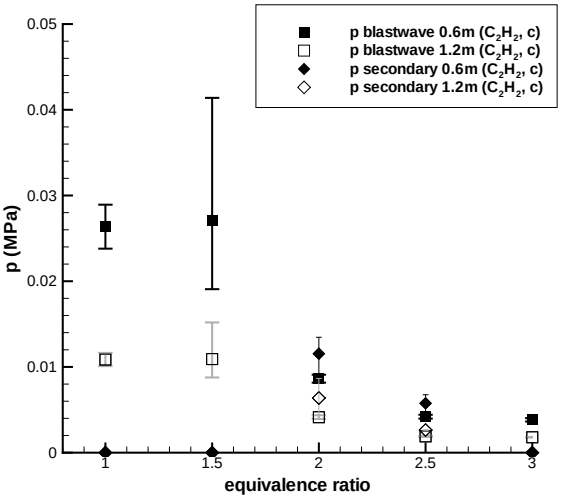

Figure 24: Peak blast wave pressure and peak pressure of secondary pressure rise vs. equivalence ratio for stoichiometric C_2H_2-O_2 initiator mixture. Center initiation location.

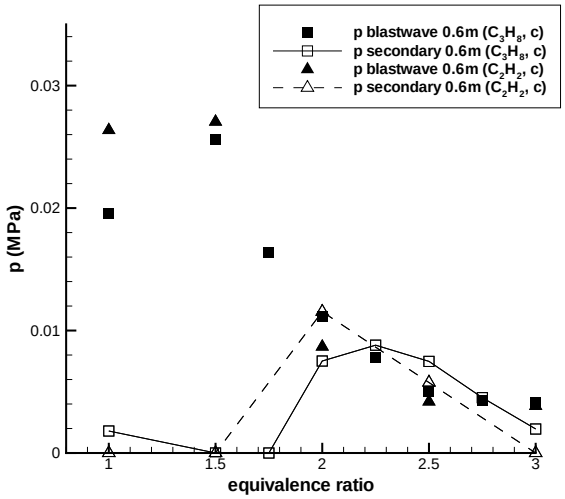

Figure 25: Comparison of blast wave pressure and peak pressure of secondary pressure rise for C_2H_2-O_2 and C_3H_8-O_2 initiator mixtures. Center initiation location. Gauge location: 0.6 m.

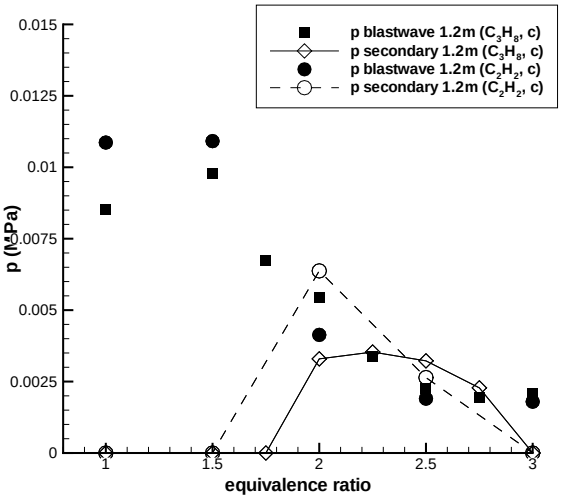

Figure 26: Comparison of blast wave pressure and peak pressure of secondary pressure rise for C_2H_2-O_2 and C_3H_8-O_2 initiator mixtures. Center initiation location. Gauge location: 1.2 m.

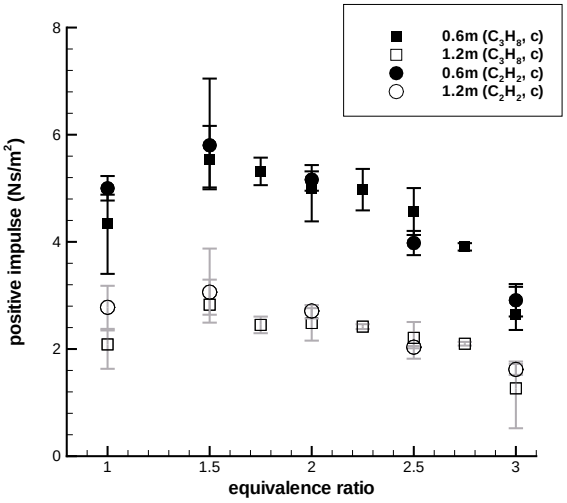

Figure 27: Impulse for C_2H_2-O_2 and C_3H_8-O_2 initiator mixture. Center initiation location.

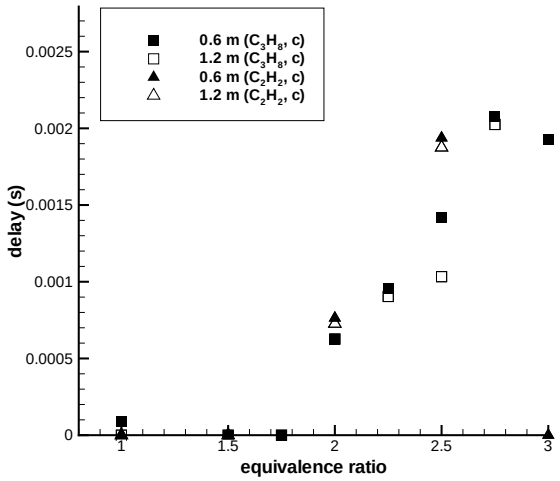

Figure 28: Comparison of secondary wave peak time for C_2H_2-O_2 and C_3H_8-O_2 initiator mixtures. Center initiation location. Gauge location: 0.6 m.

blast wave pressure occurs at $\Phi = 1$ and not $\Phi = 1.5$ as observed for the center initiation location, Fig. 29. The decrease of blast wave pressure with increasing equivalence ratio is also more pronounced for bottom initiation location. The blast wave pressures for $\Phi = 2$ are lower for the bottom initiator location. The secondary pressure rise is independent of the initiation location for $\Phi > 2$. For the bottom initiation location a secondary pressure rise occurs for $\Phi = 2$, Fig. 31 and 32, but up to 40% lower depending on the gauge location. For $\Phi \geq 2.5$, the peak pressures of the secondary pressure rise for both initiation locations are within 15%. For $\Phi = 3$, it was difficult to determine the peak of the secondary pressure rise, since the reflected wave of the wall reached the gauges simultaneously.

The positive impulse for $\Phi = 1$ and 1.5 is higher for the bottom than the center initiation location and lower for $\Phi > 1.5$, Fig. 33. The positive impulse follows the trend of the blast peak pressure for $\Phi = 1$ and 1.5 and secondary pressure rise $\Phi = 2$–3 for the change in initiation location. The point in time at which the maximum impulse is measured is increased by 0.5 ms for an equivalence ratio of 2 for the bottom initiation

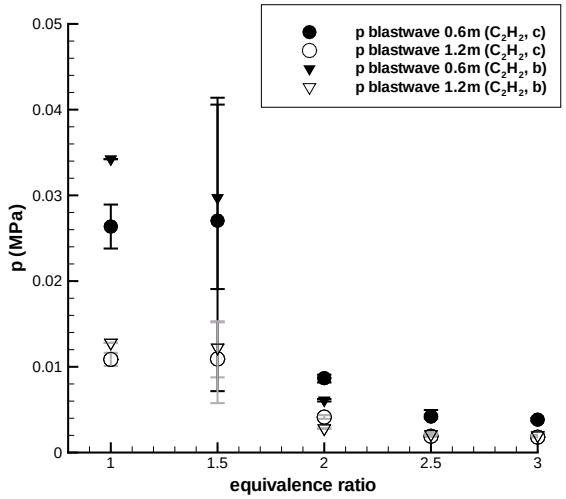

Figure 29: Comparison of blast wave pressure for center and bottom initiation locations. C_2H_2-O_2 initiator mixture.

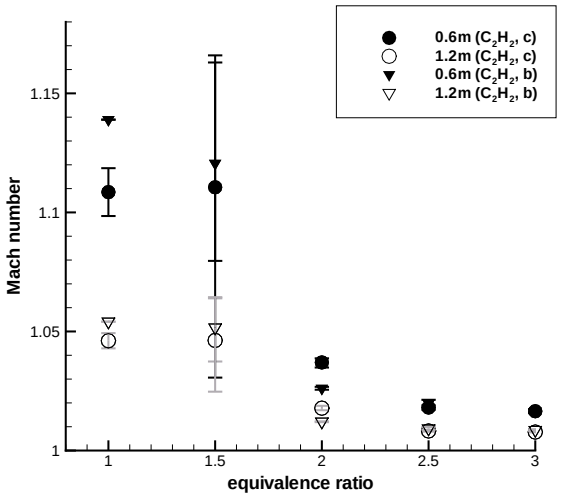

Figure 30: Comparison of Mach number derived from the shock jump condition for center and bottom initiation locations. C_2H_2-O_2 initiator mixture.

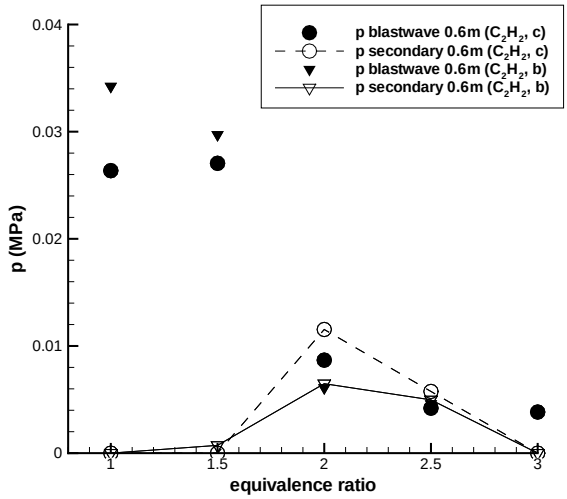

Figure 31: Comparison of blast wave pressure and peak pressure of secondary pressure rise for center and bottom initiation locations. C_2H_2-O_2 initiator mixture. Gauge location: 0.6 m.

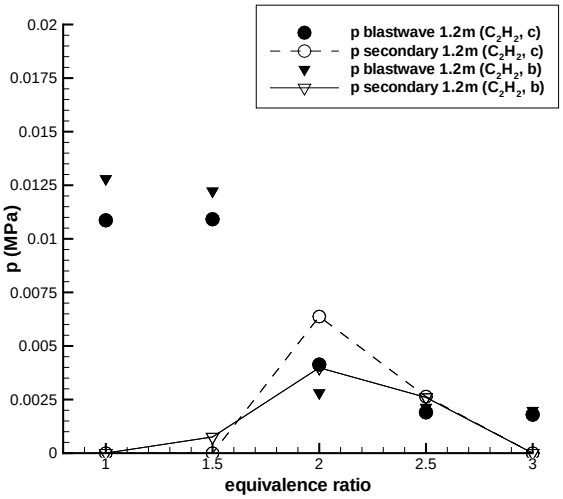

Figure 32: Comparison of blast wave pressure and peak pressure of secondary pressure rise for center and bottom initiation locations. C_2H_2-O_2 initiator mixture. Gauge location: 1.2 m.

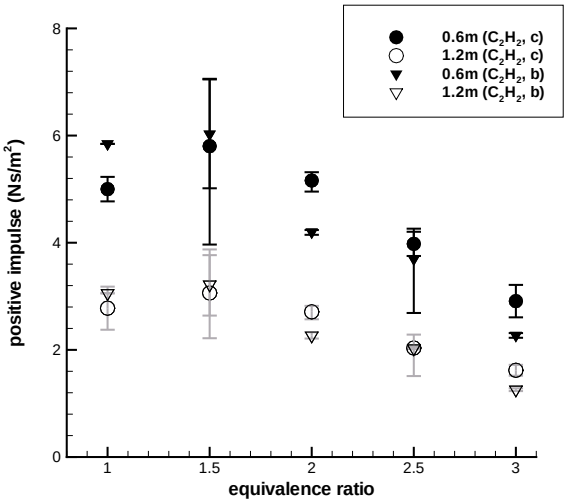

Figure 33: Comparison of impulse derived from pressure traces for center and bottom initiation locations. C_2H_2-O_2 initiator mixture.

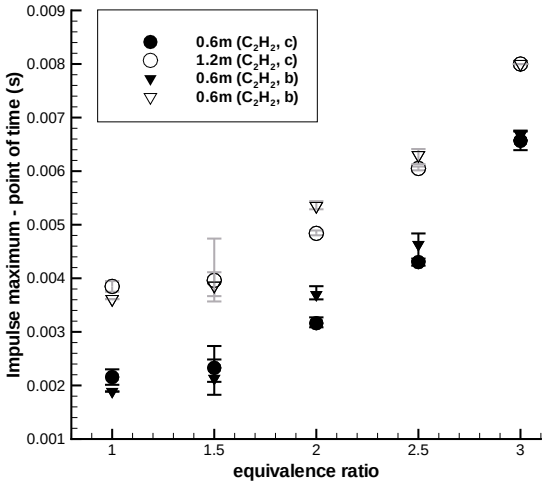

Figure 34: Comparison of point in time at which maximum impulse occurs for center and bottom initiation locations. C_2H_2-O_2 initiator mixture.

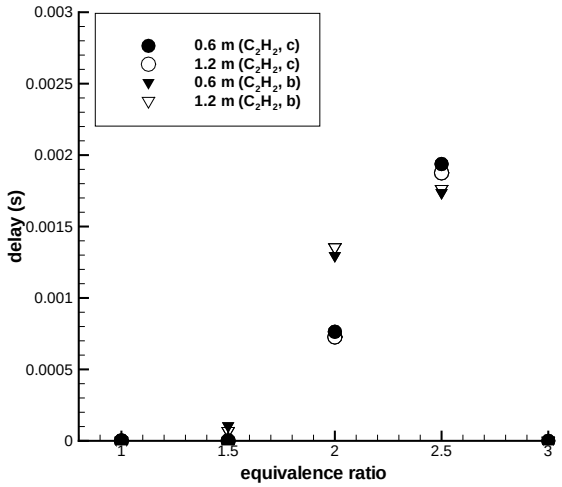

Figure 35: Delay between blast wave peak pressure and peak pressure of secondary pressure rise for center (c) and bottom (b) initiation locations. C_2H_2-O_2 initiator mixture.

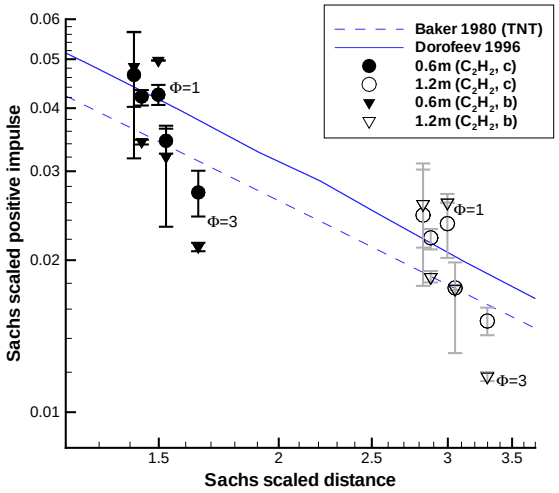

Figure 36: Comparison of the E_1-Sachs-scaled impulse derived from pressure traces for center and bottom initiation locations. C_2H_2-O_2 initiator mixture.

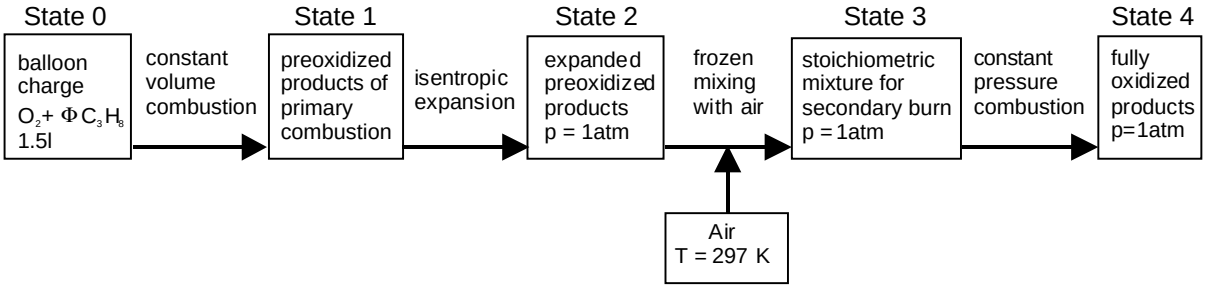

Figure 37: Schematic of model process used to analyze the primary and secondary combustion events. The designated states labeled zero to four are given above the flow chart.

location, which is caused by the later secondary pressure rise, Fig. 34. The time between the primary and secondary pressure peak is increased for $\Phi = 2$ from 0.75 ms to 1.4 ms. The delay is measured to be approximately the same at 0.6 m and 1.2 m since the blast waves for $\Phi \geq 2$ have a Mach number smaller than 1.1. The secondary pressure rise is characterized by a smooth pressure rise and nearly constant propagation velocity suggesting that an acoustic source for the secondary pressure rise is located within a radius of 0.6 m around the balloon center.

3.6 Analysis of Secondary Combustion Process

The entire combustion process can be divided up into four steps, Fig. 37, in order to carry out a simplified quantitative analysis. First, the primary combustion of the rich propane-oxygen mixture of state 0 is modeled by a constant volume combustion. Second, the hot products at state 1 are isentropically expanded to state 2 atmospheric pressure. Third, the expanded products are mixed in a chemically frozen process with cold air to form a stoichiometric mixture at state 3. Fourth, the secondary combustion of state 3 is modeled as a constant pressure reaction at a pressure of 1 atm to obtain the final state 4 of fully oxidized products.

The primary combustion event produces partially oxidized products with a composition, Fig. 38, that depends strongly on the primary equivalence ratio. The pressure and

temperature of state 1 are strong functions of the primary equivalence ratio, Fig. 39. The temperature is a maximum of 3600 K for $\Phi = 1$ and decreases with increasing equivalence ratio to 2200 K for $\Phi = 3$. Isentropic, chemically-equilibrated expansion to atmospheric pressure, Fig. A.5.1 and 41, results in a decrease in temperature to 2900 K for $\Phi = 1$ and 1100 K for $\Phi = 3$. For equivalence ratios near 1, the expanded products are nearly completely oxidized and secondary combustion can not take place. For higher equivalence ratios, the partially-oxidized species H_2 and CO are predominantly present in the products and if the temperature of the expanded products is sufficiently high, further oxidation can occur. The temperature of the products drops significantly, Fig. 42, during the expansion to atmospheric pressure.

Due primarily to the temperature dependence (Fig. 40) of the chemical equilibrium, a shift in the composition during expansion is occurring, Fig. 38. The increasing mole fraction of H_2O and deceasing mole fraction of H_2 during the expansion for $\Phi < 2$ are caused by the temperature dependence of the water-gas shift reaction, which favors H_2O over H_2 at lower temperature. Furthermore, the recombination of available OH and H leads to an increase in H_2O during the expansion for $\Phi < 2.5$, Fig. A.5.2. The increasing amount of CO_2 during the expansion is caused by the combination of CO with the available molecular and atomic oxygen for $\Phi < 2$, Fig. A.5.3. For $\Phi > 2$, the shift during the expansion is minor for all species. The volume of the expanded products of the primary combustion is decreasing with increasing equivalence ratio due to the lower temperature. The balloon of volume 1.5 l expands to a volume of approximately 20 l for $\Phi = 1$ compared to 14 l for $\Phi = 3$, Table 1. This corresponds to a fireball diameter of approximately 0.34 m for $\Phi = 1$ and 0.30 m for $\Phi = 3$.

The amount of air needed to create a stoichiometric mixture in state 3 increases with increasing equivalence ratio of the initial balloon composition, Table 1. For the 1.5 l balloon charge and an initial equivalence ratio of 3, approximately 9 l of air at normal

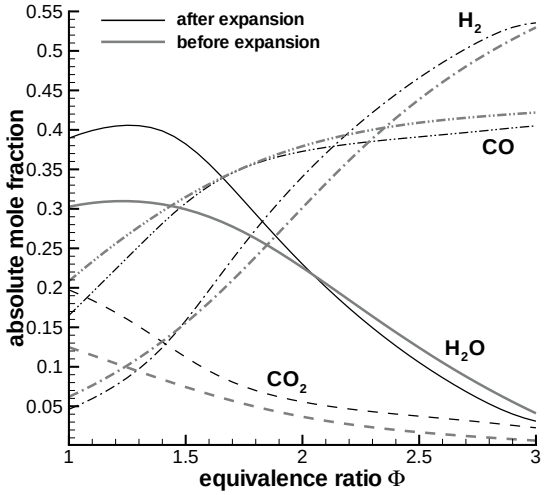

Figure 38: Major products of state 1 and state 2 calculated with an equilibrium solver (STANJAN) for a constant volume combustion for a propane-oxygen mixture as a function of the equivalence ratio. T_{state1}= 294 K, p_{state1}= p_{state2}= 1.013 bar.

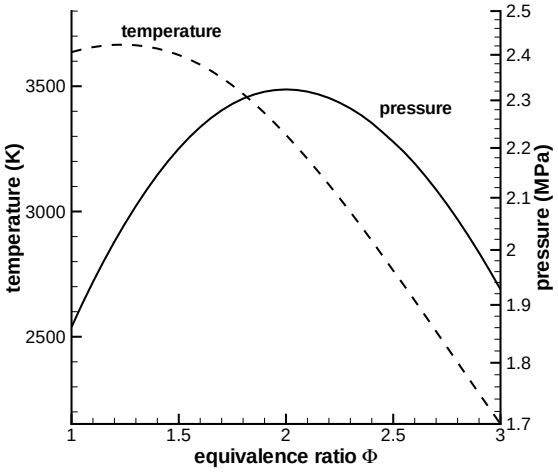

Figure 39: Thermodynamic properties of state 1 calculated with an equilibrium solver (STANJAN) for a constant volume combustion for a propane-oxygen mixture as a function of the equivalence ratio. Initial temperature 294 K, initial pressure 1.013 bar.

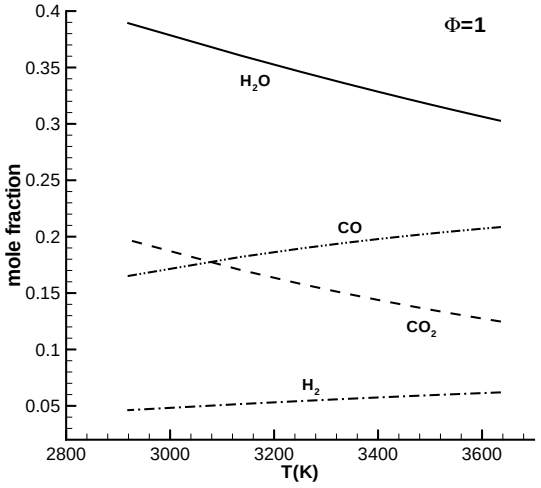

Figure 40: Shift in major species for chemically-equilibrated isentropic expansion to atmospheric pressure calculated for Φ=1.

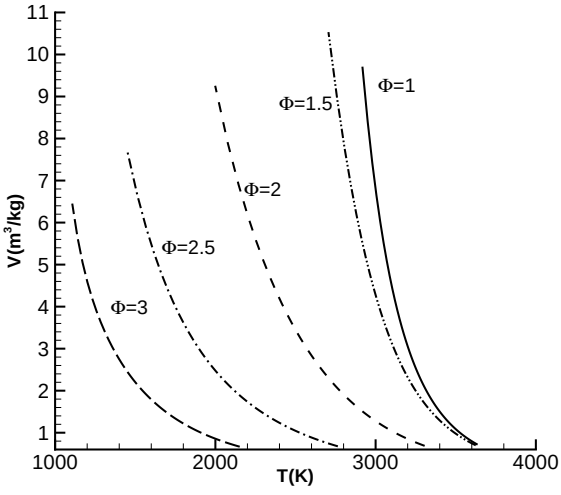

Figure 41: Volume-temperature relationship for chemically-equilibrated isentropic expansion to atmospheric pressure calculated for different equivalence ratios of the primary combustion.

conditions are needed to create a stoichiometric mixture at state 3. The temperature at state 3, after mixing with cold air, decreases rapidly as the equivalence ratio increases, Fig. 43. For equivalence ratios of 2.5 and 3, the temperature at state 3 is 700 K and 550 K, respectively.

Volume in l based on 1.5 l balloon charge at state 0						
State 0			State 1	Air added	State 4	Δ V
Φ	C_3H_8	O_2	after expansion	T=297K	final	displacement
1	0.25	1.25	20.3	0.00	20.2	0
1.5	0.34	1.15	22.5	2.75	42.3	17.0
2	0.42	1.07	20.2	5.10	61.0	35.7
2.5	0.50	1.00	17.1	7.14	77.7	53.4
3	0.56	0.93	14.5	8.93	92.5	69.1

Table 1: Volume calculated for different states in the modeled combustion process. All volumes are given in l and based on the initial balloon charge of 1.5 l at state 0.

The final (state 4) temperature (Fig. 43) and specific volume (Fig. 44) have a weak dependence on the initial equivalence ratio. Secondary combustion results in products at state 4 with final temperatures that are between 2500 and 2850 K for initial equivalence ratios between 3 and 1. The combustion of the partially oxidized products almost completely compensates for the decrease in temperature due to mixing with the cold air. The total volume ΔV displaced by the secondary combustion process can be calculated by subtracting the volume of the expanded products (state 2) and the added air from the final volume (state 4). The displaced volume increases approximately linearly with increasing equivalence ratio up to a maximum value of 70 l for an initial equivalence ratio of 3, Fig. 45. Note that this model does not take into account the rates of reaction, the reaction rate dependence on temperature, or the mixing process. We expect that this thermodynamic model is, at best, a rough guide to the overall behavior of the fireball. The estimates for maximum volume displacement will be most reliable when the temperature of state 3 is high enough that reaction will occur rapidly, that is, faster than on the time scale of 2-3 ms that is observed for the duration of the secondary pressure wave.

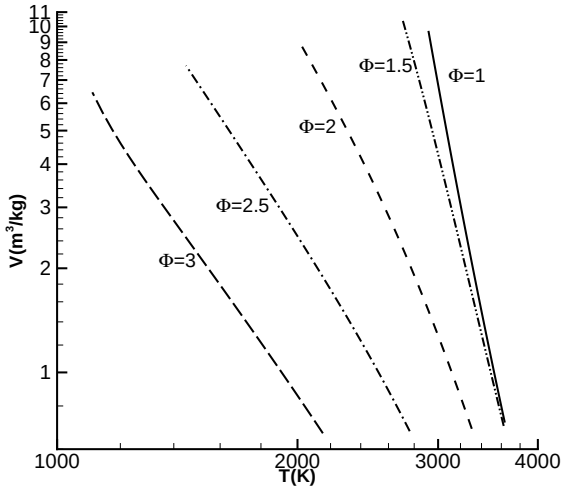

Figure 42: Volume-temperature relationship illustrating the dependence of heat capacity ratios on equivalence ratio.

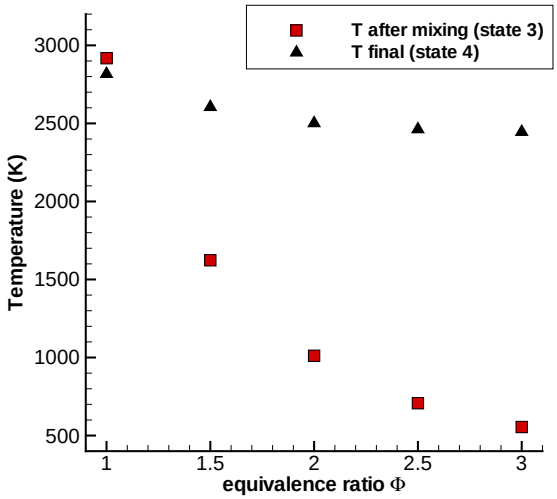

Figure 43: Temperature at states 3 and 4.

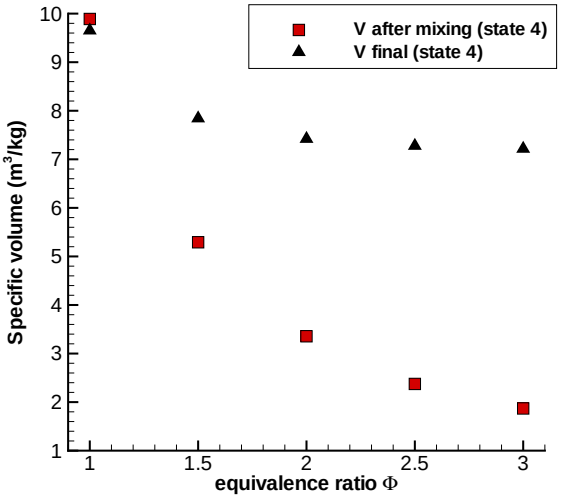

Figure 44: Specific volume at states 3 and 4.

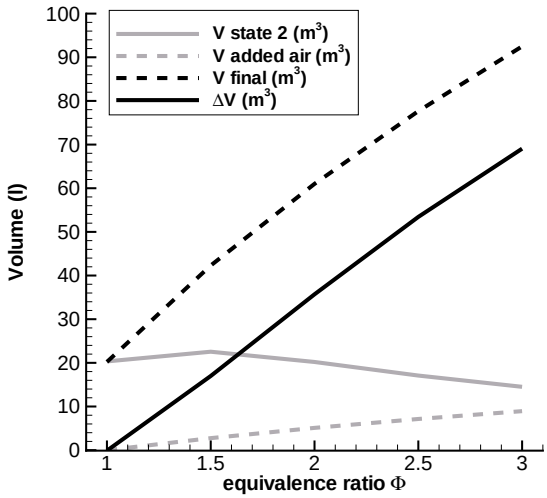

Figure 45: Volumes calculated for different states in the model cycle based on the 1.5 l charge as a function of initial equivalence ratio. The total displaced volume is also shown.

The experimental results indicate that this is the case for equivalence ratios between 2 and 2.5. However, for equivalence ratio 3, the reaction rates are apparently too slow for the secondary combustion to occur.

3.7 Acoustic Approach to Secondary Combustion

This section outlines a simple technique for analyzing the pressure waves that are generated by secondary combustion. The idea behind this is to treat the pressure wave generation process as being equivalent to a spherically-symmetric volume source that is centered about the balloon origin. Physically, the source of volume is the gas expansion and mole change resulting from mixing and combustion of the partially-oxidized fireball with the surrounding air.

The volume displacement rate $Q = dV/dt$ can be related, see Landau and Lifshitz (1987), to the pressure perturbation p' at a distance r from the volumetric source origin using the acoustic potential ϕ,

$$p' = p - p_0 = \rho_0 \frac{\partial \phi(r,t)}{\partial t}, \tag{4}$$

$$\phi(r,t) = -\frac{Q(t - r/c)}{4\pi r}, \tag{5}$$

where p_0 is the pressure, ρ_o the density, and c the speed of sound of the surrounding air. The pressure perturbation p' is determined by the time derivative of the displacement rate

$$p'(r,t) = \rho_0 \frac{\dot{Q}(t - r/c)}{4\pi r}, \tag{6}$$

which can be inverted to determine the volumetric displacement rate from the measured pressure signals

$$Q(t) = \frac{dV}{dt} = \frac{4\pi R}{\rho_0} \int_0^t p'(\tilde{t} + R/c)\, d\tilde{t} \tag{7}$$

where the pressure is measured at a distance $R = r$. The volumetric displacement rate is, therefore, proportional to the integrated pressure signal. Computations for several shots at $\Phi = 2.5$ are shown below in Figs. 46-51. Only the contribution due to the secondary combustion is shown and the range of integration has been selected based on visual inspection of the signals. The volume displacement rate smoothly increases from zero to a maximum value and then decays back to zero again. The time history is asymmetric, with a rise time that is slightly smaller than the decay time. The time history of the displacement rate reflects the finite duration of the secondary combustion event and also the gradual nature of the initiation and termination of combustion. Initially, the source term is zero and begins to rise only after a certain amount of mixing and reaction has taken place. Only a finite amount of partially-oxidized material is available for secondary combustion and once most of that has been consumed, the volume generation rate begins to decrease and ultimately returns to zero once the supply of partial oxidation products is exhausted. A consequence of this behavior is that the time integral of the negative and positive phases of the pressure signal have to cancel out so that $Q(t)$ approaches zero for large times, Eq. 7.

The four analyzed shots (104, 105, 174, and 175) were all carried out with the center initiation location and an equivalence ratio of 2.5. The interval for integration was chosen from the beginning of the secondary pressure rise to the arrival of the reflected wave from the wall. In shots 104 and 105, C_3H_8-O_2 was used as the initiator; in shots 174 and 175, C_2H_2-O_2 was used. Depending on the gauge location and initiator mixtures, the maximum displacement rate Q is found to be approximately 16 to 20 m^3/s. For the gauge located at 1.2 m, the wave reflected from the wall reaches the gauge before the pressure measured at the gauge reached ambient pressure. The integration is stopped at this point in time, since the negative phase of the pressure history is superimposed on the reflected wave. The computed volume displacement rate does not return to zero in

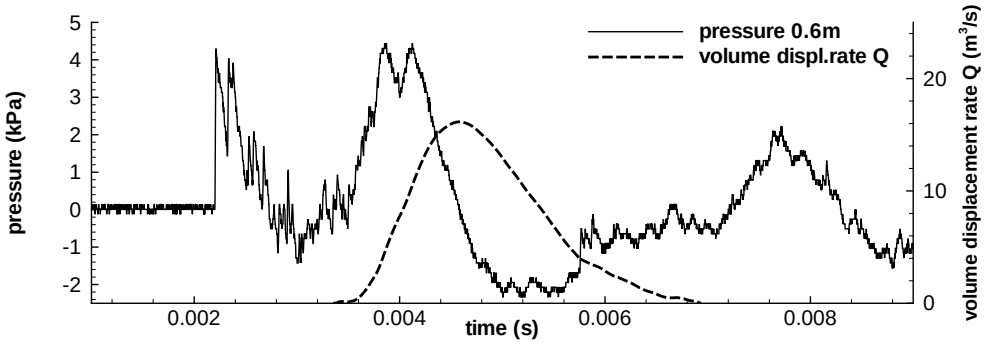

Figure 46: Shot 106, $\Phi = 2.5$. Volume displacement rate calculated from Eq. 7 using the pressure history obtained at 0.6 m. The integration was carried out from 3.1 ms to 7.04 ms. The time delay of R/c is not taken into account.

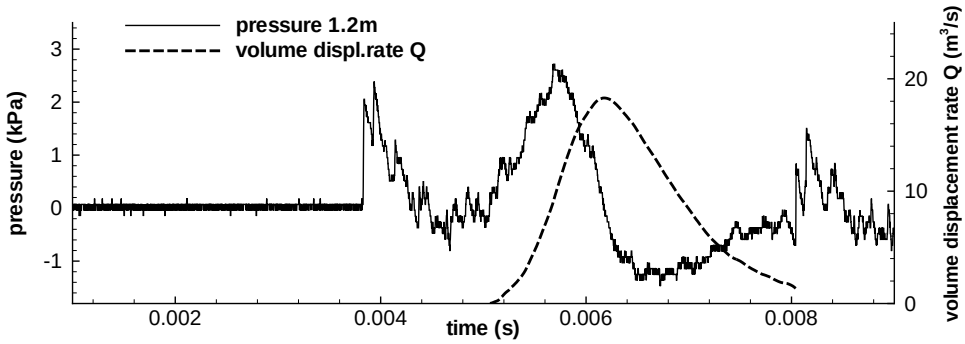

Figure 47: Shot 106, $\Phi = 2.5$. Volume displacement rate calculated from Eq. 7 using the pressure history obtained at 0.6 m. The integration was carried out from 4.85 ms to 7.82 ms. The time delay of R/c is not taken into account.

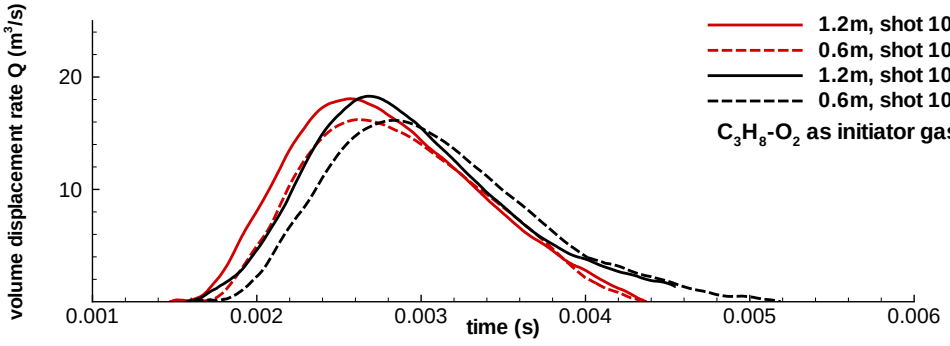

Figure 48: Shot 104 and 106, both $\Phi = 2.5$. Volume displacement rate calculated from Eq. 7 for both gauge locations taking the delay time R/c into account, where R is the distance from the gauge to the fireball and c is the speed of sound.

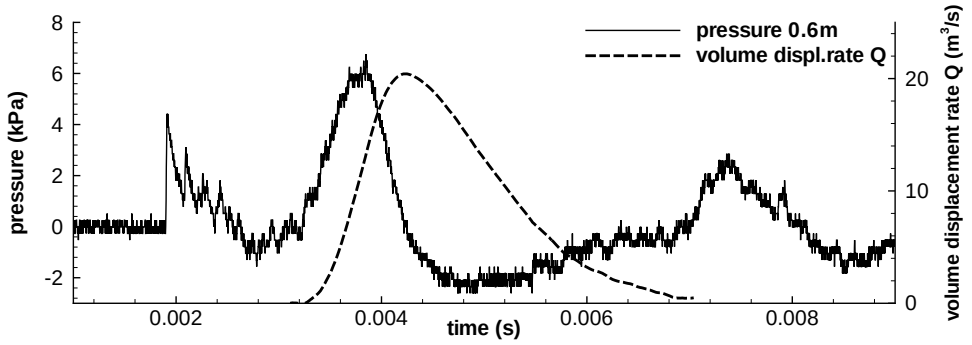

Figure 49: Shot 174, $\Phi = 2.5$. Volume displacement rate calculated from Eq. 7 using the pressure history obtained at 0.6 m. The integration was carried out from 3.1 ms to 7.04 ms. The delay time of R/c is not taken into account.

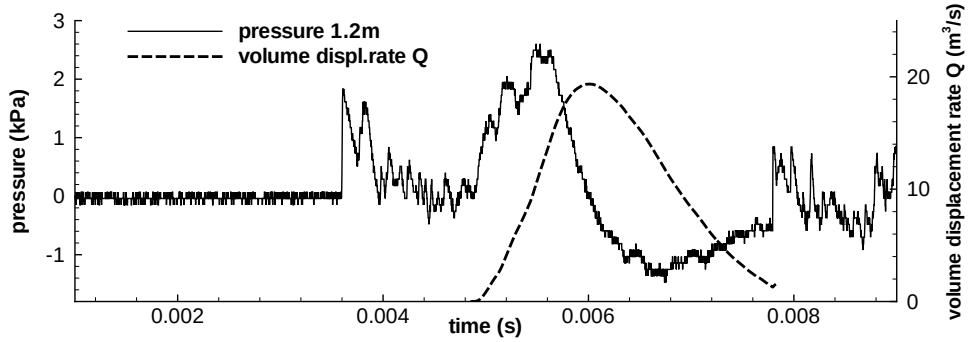

Figure 50: Shot 174, $\Phi = 2.5$. Volume displacement rate calculated from Eq. 7 using the pressure history obtained at 1.2 m. The integration was carried out from 4.85 ms to 7.82 ms. The delay time of R/c is not taken into account.

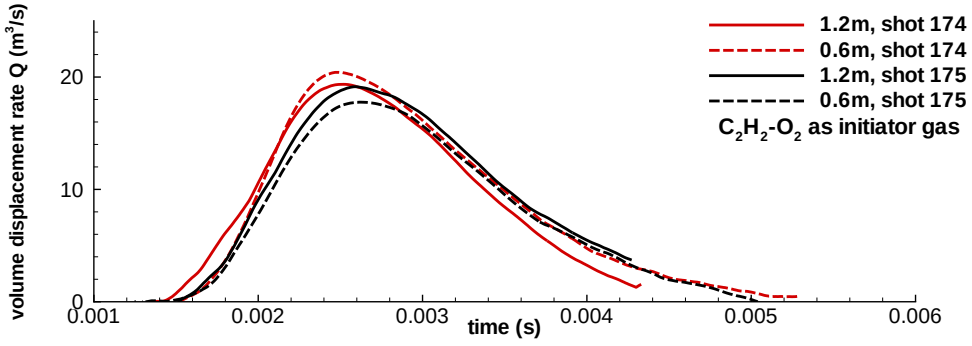

Figure 51: Shot 174 and 175, both $\Phi = 2.5$. Volume displacement rate calculated from Eq. 7 for both gauge locations taking the time R/c into account, where R is the distance from the gauge to the fireball and c is the speed of sound.

this case. Taking into account the delay in wave travel to the gauge location at 0.6 and 1.2 m, there is good agreement between the Q derived from the gauge locations at 0.6 and 1.2 m, Fig. 48 and Fig. 51. The volume displacement rate derived from the gauge location at 1.2 m is slightly larger than the ones derived from the gauge at 0.6 m. The maximum in the volume displacement rate occurs at about 2.8 ms after the ignition.

The net volume displacement ΔV (Fig. 52) can be obtained by integrating the volume displacement rate (Fig. 48, 51) for the time interval considered. The total volume displacement (C_3H_8-O_2 initiator) derived from the gauge at 0.6 m is 23 l and, for the gauge at 1.2 m, is 25 l. For the experiments using C_2H_2-O_2 initiators, ΔV ranges between 28 l and 30 l. These values are 44-56% of the total volume displacement of 53 l derived from the ideal thermodynamic model discussed in the previous section. The thermodynamic model assuming a stoichiometric mixture at state 3 is the upper bound of volume displacement that can be achieved. Furthermore, for slower volume displacement rates not the entire total volume displacement contributes to the pressure rise.

The volume displacement determined by the acoustic analysis can be compared with the apparent volume of the luminous fireball observed on the high-speed video. The fireball luminous volume (Fig. 53) was determined numerically by assuming a cylindrically-symmetric fireball shape and performing a numerical integration on a frame-by-frame basis. The visual edge of the fireball was defined by applying a threshold filter to each image. For $\Phi = 2.5$, the steepest increase in luminous volume occurs at approximately 2.8 ms, which agrees with the time of the maximum volume displacement rate derived from the acoustic analysis. The maximum value of the luminous volume is about two times larger than the volume displacement determined by the acoustic analysis for this case. This is not unreasonable since the luminous volume is not expected to be fully mixed and there are probably substantial “funnels” or “pockets” of air within the luminous region that are not molecularly mixed or reacted with the combustion products.

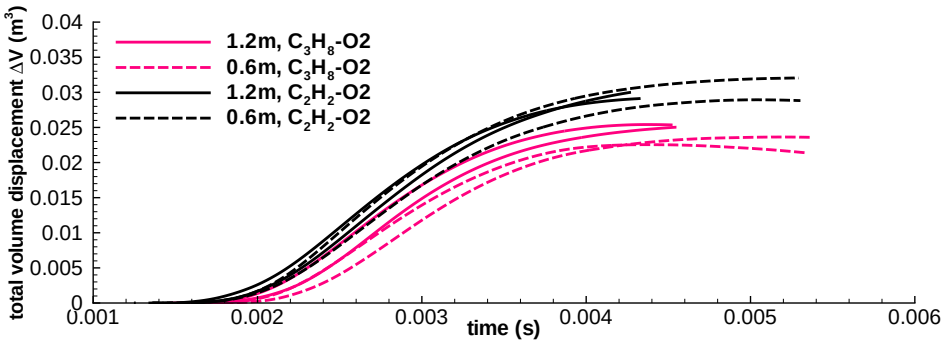

Figure 52: Volume displacement ΔV derived from integrating the volume displacement rate Q shown in Fig. 51 and Fig. 48. $\Phi = 2.5$, C_3H_8-O_2 and C_2H_2-O_2 initiator mixture.

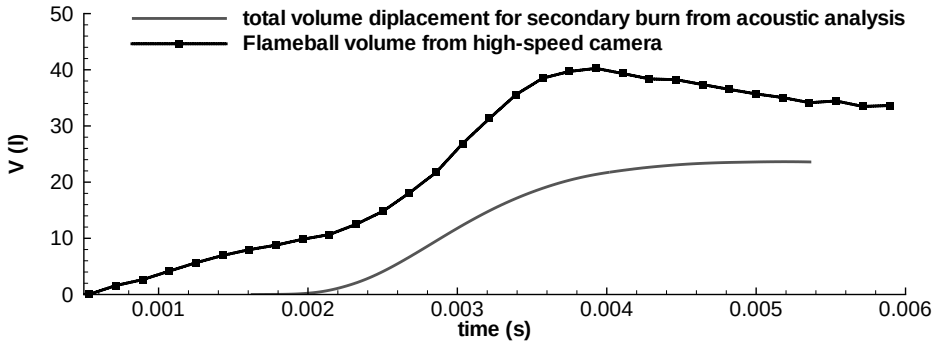

Figure 53: Volume displacement ΔV derived from integrating the volume displacement rate Q shown in Fig. 51 and integrated volume of fireball from high speed video. Shot 106. $\Phi = 2.5$, C_3H_8-O_2 initiator mixture. The delay time of R/c is included.

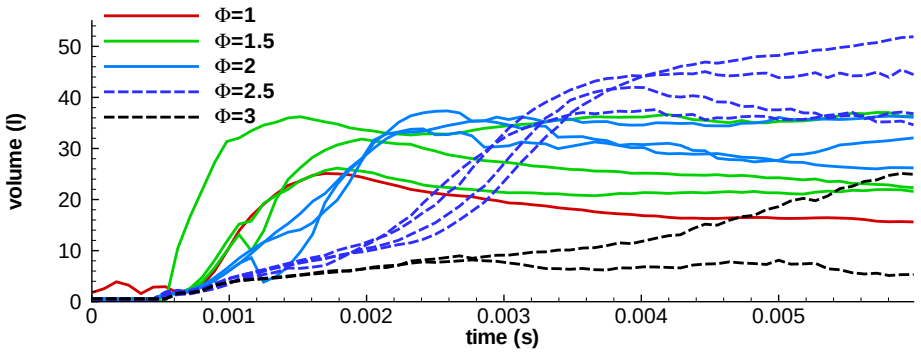

Figure 54: Luminous volume of fireball determined by analyzing the high-speed video for shots at several different equivalence ratios. C_3H_8-O_2 initiator mixture.

For $\Phi < 2.5$, the luminous volume increases much more rapidly, Fig.54, than at higher equivalence ratios. For $\Phi > 2.5$, the luminous volume increases very slowly which agrees with the lack of a definite secondary pressure wave for these cases. More observations about the luminous volume time dependence are given in the subsequent section.

3.8 High-speed camera imaging

A high-speed camera was used to record the natural luminosity of the fireball. The camera was operated at 11200 frames per second, has a resolution of 256×256 pixels, and an exposure time of $2\,\mu s$. This camera was used to image the experiments for the center initiation location and the C_3H_8-O_2 initiator mixture. An 18-mm lens (Nikon, 18-35MM F/3.5-D ED zoom Nikkor) with an aperture between f/3.5 and f/11 was used to image the event over a field of view of 0.57 m × 0.57 m. The spectral sensitivity range was approximately between 300 and 800 nm. The sequence of images obtained for a shot with equivalence ratio of 1.5 shows that the balloon stretches slightly before it ruptures, Fig. 55 and B.22. On the second frame can be seen the light-bulb-shaped outline of the initial balloon shape. The time $t = 0$ coincides with the initiation of the spark plug

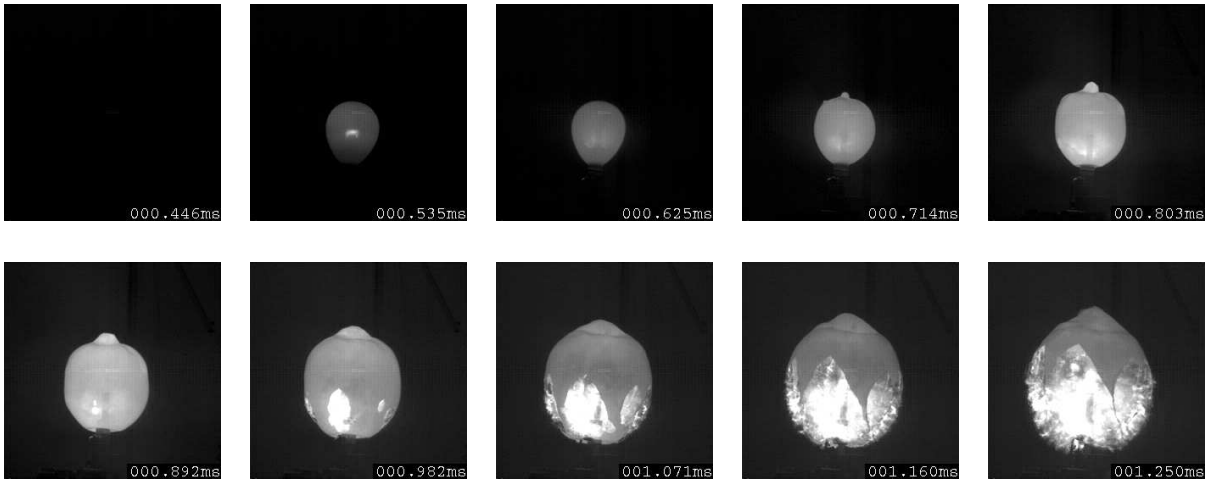

Figure 55: Sequence of high-speed movie for $\Phi = 1.5$ (shot 111).The complete sequences for all high-speed movies is shown in Sec. B.

in the initiator tube. The detonation emerges out of the initiator tube at approximately 0.5 ms and illuminates the balloon from the inside. Despite the balloon opacity, one can identify on some image sequences (e.g., Fig. B.10) the diffracting detonation emerging from the initiator tube into the balloon. For higher equivalence ratios, the balloon seems to rupture at a later point in time and expands further, see App. B. Also, for higher equivalence ratios, the luminosity is occurring slower and the fireball remains for a much longer duration, Fig. 56.

The images were analyzed to find the variation of total luminosity as a function of time. The luminosity is derived by averaging the counts of all pixels for each frame individually and normalizing by the brightest frame, since different aperture settings were used for different shots. Saturation effects which are observed in some images are neglected in this analysis. The maximum luminosity occurs 2.5 ms after the ignition of the initiator tube for $\Phi = 1$ and at 13 ms for $\Phi = 3$. There have been extensive studies (AIChE, 1994) of fireballs created by the sudden release and combustion of fuel clouds. For example, large-scale experiments (Dorofeev et al., 1995a) with up to 100 tonne of liquid fuel resulted in a maximum heat flux about 1 s after the ignition. The heat flux, fireball duration, and maximum size of the fireball increase with increasing mass of fuel (AIChE, 1994) so the long duration of these large fireballs is not unexpected. There are few data on small fireballs of partially-oxidized products so it is not possible to directly compare the present results with those of previous studies.

The pressure traces from the gauges located at 0.6 and 1.2 m can be overlayed with the high-speed video. The time between the pressure wave leaving the balloon edge and detection at the pressure gauge can be calculated assuming a spherical shock wave. This enables identifying the image frame which corresponds to the point in time at which a shock wave was sent out from the fireball center. The Mach number at the pencil gauge can be computed using the shock jump conditions and the velocity as a function

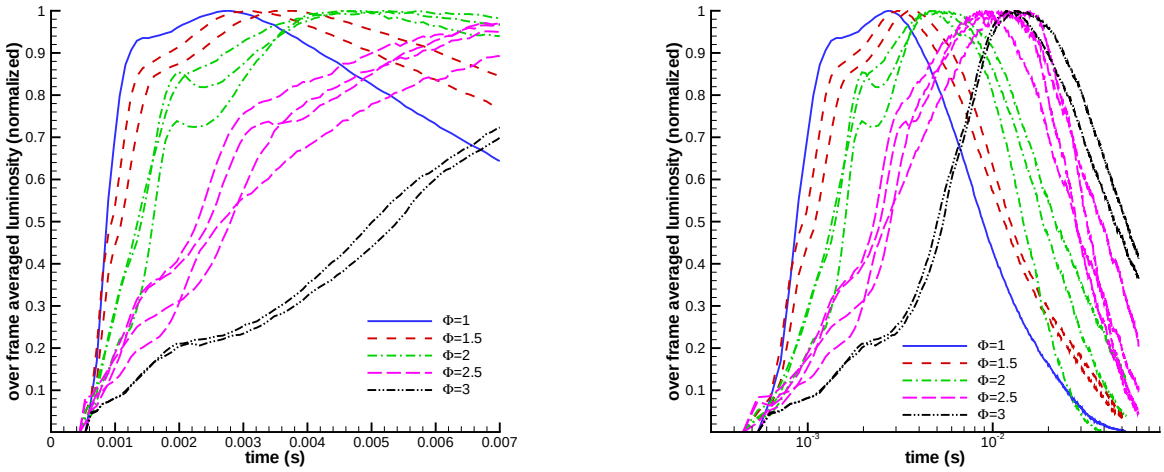

Figure 56: Luminosity derived from high-speed videos by averaging the luminosity of each frame and normalizing by the peak luminosity.

of distance can be derived by using the inverse dependence of pressure on distance:

$$Ma = \left(\frac{\Delta p}{p_0}\frac{\gamma+1}{2\gamma}+1\right)^{\frac{1}{2}} \tag{8}$$

$$u(x) = a_0\left(\frac{\Delta p_{gauge}}{p_0}\frac{x_{gauge}}{x}\frac{\gamma+1}{2\gamma}+1\right)^{\frac{1}{2}} \tag{9}$$

$$\Delta t(x_{gauge}) = \int_{0.07m}^{x_{gauge}} \frac{1}{a_0}\left(\frac{\Delta p}{p_0}\frac{x_{gauge}}{x}\frac{\gamma+1}{2\gamma}+1\right)^{-\frac{1}{2}} dx, \tag{10}$$

where Ma is the Mach number of the shockwave, Δp is the pressure jump, p_0 is the ambient pressure (1 atm), and γ the specific heat ratio of the surrounding air. The shock velocity in the lab frame is $u(x)$ at a distance x from the balloon center, where Δp_{gauge} is the pressure jump measured at the gauge location with a distance x_{gauge}. The transit time $\Delta t(x_{gauge})$ of the shock wave to travel from the balloon edge (0.07 m) to the gauge location x_{gauge} (0.6 or 1.2 m). The transit time $\Delta t(x_{gauge})$ is obtained by integrating the inverse velocity over the distance. For the blast wave peak pressure of 24 kPa and 9 kPa measured at 0.6 m and 1.2 m respectively for $\Phi = 1$ (shot 113), the wave transit time is 1.29 ms and 3.02 ms. The blast wave is detected at the gauges at 2.07 ms (0.6 m) and 3.62 ms

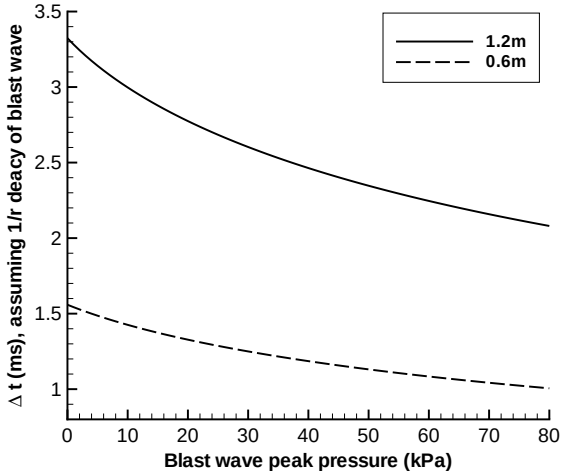

Figure 57: Transit time Δt that a blast wave needs to travel from the balloon edge (0.07 m) to the gauge located at 0.6 m and 1.2 m as a function of the blast wave peak pressure measured at the corresponding gauges, Eq. 10. A blast wave pressure decay of $1/r$ is assumed.

(1.2 m). The time that the blast wave originated from the balloon edge is computed to be 2.07-1.29=0.78 ms and 3.62-3.02=0.6 ms. This implies that the shockwave is generated at about 0.7 ms, which corresponds well to Frame 4 in the high speed image sequence shown in Fig. 55. In Frame 4 the balloon is fully illuminated but not expanded, so the primary blast wave seems to get transmitted through the balloon. Uncertainties in this analysis can be caused by the time-base uncertainty of the high-speed movie which can be up to 1 frame, since the camera is used in pre-trigger mode. Furthermore, the blast wave might decay slower than the assumed $1/r$ dependence, Dorofeev et al. (1995b). For higher equivalence ratios and weaker blast waves, the transit time (Fig. 57) is increased. For $\Phi = 2.5$ (shot 105), the peak pressures of the blast wave at 0.6 m and 1.2 m are 10.8 kPa and 6.1 kPa and the corresponding Δt are 1.38 ms and 3.23 ms, respectively. This leads to a blast wave generation time for the 0.6 and 1.2 m gauges respectively of 0.65 ms and 0.54 ms.

An event corresponding to the secondary pressure rise can not be clearly identified from the high-speed imaging. Assuming a propagation speed of the secondary pressure rise equal to the sound speed, the point in time corresponding to the secondary pressure rise in the high-speed image sequence can be back-calculated in the fashion illustrated above for the blast wave. For some cases, this time falls during the rupture of the balloon. Further investigation is required in order to be more specific in correlating the images with the secondary pressure rise.

4 Conclusions

A series of experiments was carried out to investigate the effect of fireball composition on secondary combustion. The fireball was created from a 1.5 liter balloon filled with a propane-oxygen mixture ($1< \Phi <3$) and initiated by a detonation. Two initiation locations and two initiator strengths were studied. Two pencil pressure gauges located at 0.6 and 1.2 m and in some experiments, simultaneous high-speed imaging, were used as diagnostics. For $\Phi > 1$, the incompletely oxidized products from the primary burn mix with the surrounding air and may be oxidized in a secondary combustion process.

The unique feature of the present experiments was a repeatable secondary pressure pulse for sufficiently rich mixtures. For the configurations studied, the effect of the secondary pressure rise was most pronounced for $\Phi = 2.5$. For $2.5 > \Phi > 1.75$, a smoother secondary pressure rise occurred between 1 and 3 ms after the primary blast wave, depending on the equivalence ratio. The secondary pressure was observed repeatably for all initiation configurations. For $\Phi = 2$, the secondary pressure rise magnitude exceeds the primary blast peak pressure. The nature of the secondary pressure pulse is a strong function of the initial equivalence ratio. For $\Phi = 1$ and 1.5, no secondary pressure waves are observed. This is apparently due to the lack of fuel in these near-stoichiometric mixtures. For $\Phi = 1.75$, the volume displacement is sufficiently rapid that weak shock waves are generated by the secondary combustion process. For $2.5 > \Phi > 2$, the volume displacement rate is a smooth function of time and is consistent with progressive mixing and combustion of the fireball with the surrounding air. For $\Phi = 3$, no distinct secondary combustion pressure wave is observed. This is consistent with the cold temperatures predicted for the expanded fireball.

An acoustic analysis of the measured pressure histories has been carried out to infer the rate of volume displacement and the total volume displaced by the secondary combustion. The results of the acoustic analysis are in reasonable agreement with a simpli-

fied thermodynamic model predicting the total volume displacement assuming constant-pressure combustion for the secondary burn. An analysis of the fireball luminosity of the high-speed images was performed and the volume of luminous gas was estimated. The point in time of the most rapid luminous volume increase derived from the high-speed videos coincides with the point in time of the largest volume displacement rate derived from the acoustic analysis.

The pressure and impulse measurements indicate that the explosions of the rich propane-oxygen mixtures have some unusual characteristics in the near-to-intermediate field measurement locations used in this study. For nearly stoichiometric mixtures, $\Phi = 1$ and 1.5, the leading blast wave peak pressures and impulses are comparable with the previously-measured gaseous and high explosive blasts when the energy content of the balloon only is used to formulate Sachs scaling variables. This is consistent with a detonation being initiated in the balloon at these equivalence ratios. The peak pressure of the leading wave rapidly decreases below the energy-equivalent reference blast values as the equivalence ratio is increased. This is consistent with a much slower combustion process than detonation for $\Phi > 2$. At $\Phi = 3$, the peak blast pressure is only 15% of the reference blast pressure, consistent with a flame speed of 60 m/s.

For all intermediate equivalence ratios, $2.75 > \Phi > 1$, the Sachs-scaled agrees well with the predictions on the basis of the energy in the balloon alone. This is consistent with a non ideal explosion resulting in a pressure decay following the leading blast that is slower than the reference case and also, for $2.5 > \Phi > 1.75$, a significant contribution from the secondary combustion. Although the impulse is as expected on the basis of the balloon contents alone, the augmentation due to mixing and combustion with the surrounding air is still lower than what could be achieved if all the fuel was rapidly and completely oxidized. From a purely thermodynamic point of view, at least a factor of two increase in the impulse over the values obtained in this study for $3 \leq \Phi \leq 2$ may be

possible for the richest cases.

One of the key results of the present study has been the documentation of the existence of the secondary pressure wave. Previous studies on rich fireball combustion in high explosives have focused on examining the contribution of fireball mixing and combustion to pressure over much longer times for which the confinement plays a significant role. In contrast, the present study has emphasized the acoustic nature of the secondary pressure waves and the origin of these pressure waves due to the processes at the interface between the fireball and the atmosphere. The presence of the secondary pressure peak and the higher impulses indicate that there is the potential for significant enhancement of the blast through secondary combustion. Further experiments are needed to determine if interaction of reflected shock waves with the fireball can be used to increase the mixing and combustion rates in order to enhance the secondary pressure pulse. The secondary pressure pulse also provides a very demanding test for mathematical modeling of the secondary combustion process since it is proportional to the time derivative of the volume generation rate.

4.1 Future Directions

The present experiments are first steps in providing detailed experimental data and developing an understanding of the mechanics of the secondary combustion of partially-oxidized combustion products in fireballs. Clearly, secondary combustion is a very complex phenomenon requiring detailed considerations of chemical and physical processes together with multi-dimensional numerical modeling of the fireball and chemical reactions in order to make quantitative analyses. Additional experiments will be needed to clarify the appropriate physical and chemical models and also to provide detailed data for validating simulations. These experiments include:

1. Visualization of the fireball-air mixing interface by light sheet scattering techniques.

2. Effect of reflected and focusing pressure waves on the intensity of secondary combustion.

3. Influence of balloon membrane - this could be examined by using large soap bubbles to contain the initial mixture.

4. Effect of particulates within the fireball - combustible and inert - on the secondary combustion event.

5. Quantifying the time-dependence of the species within the fireball and mixing zone.

Bibliography

AIChE. *Guidelines for Evaluating the Characteristics of Vapor Cloud Explosions, Flash Fires, and BLEVES*. American Institute of Chemical Engineers, 1994. Center for Chemical Process Safety. 15, 17, 37

AMC. *Engineering design handbook, Explosions in Air*, volume 1. US Army Materiel Command, 1974. AMCP 706-181. 12, 16

Q. A. Baker and M. J. Tang. Vapor-cloud explosion analysis. In *28th Loss Preventions Symposium*, Atlanta, USA, 1994. 18

W. E. Baker, J. J. Kulesz, P. S. Westine, P. A. Cox, and J. S. Wilbeck. A manual for prediction of blast and fragment loading on structures. *U.S. Department of Energy Report*, DOE/TIC 11268(3), 1980. 13, 16, 18

S. B. Dorofeev, V. P. Sidorov, A. A. Efimenko, A. S. Kochurko, M. S. Kuznesov, B. B. Chaivanov, D. I. Matsukov, A. K. Pereverzev, and V. A. Avenyan. Fireballs from deflagration and detonation of heterogenous fuel-rich clouds. *Fire Safety Journal*, 25: 323 – 336, 1995a. 37

S. B. Dorofeev, V. P. Sidorov, M. S. Kuznesov, A. E. Dvoinishnikov, V. I. Alekseev, and A. A. Efimenko. Air blast and heat radiation from fuel-rich mixture detonation. *Shock Waves*, 6:21 – 28, 1995b. 13, 14, 15, 16, 17, 18, 39

W. Fickett and W. C. Davis. *Detonation*. University of California Press, Berkerely, CA, 1979. p. 39. 15

L. D. Landau and E. M. Lifshitz. *Course of Theoretical Physics*, volume 6, Fluid Mechanics. Butterworth-Heinemann, 2nd edition, 1987. ISBN 0-08-033933-6. Chapter VIII: Sound. 30

I. O. Moen, P. A. Thibault, and J. W. Funk. Blast wave parameters from non-spherical fuel-air explosion. In *8th International Symposium on Military Application of Blast Simulation*, Spiez, Switzerland, 1983. 16, 18

M. J. Tang and W. E. Baker. A new set of blast curves from vapor cloud explosion. *Process Safety Progress*, 18(3):235–240, 1999. 18, 19

A Plots

A.1 Peak pressure

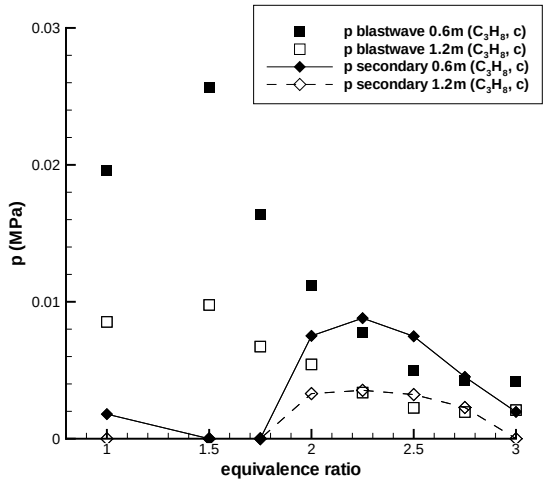

A.1.1: Peak pressure for C_3H_8-O_2 initiator. Center initiation location.

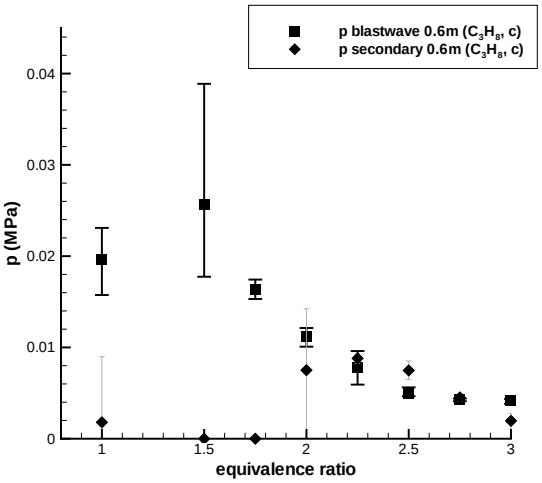

A.1.2: Peak pressure for C_3H_8-O_2 initiator. Center initiation location.

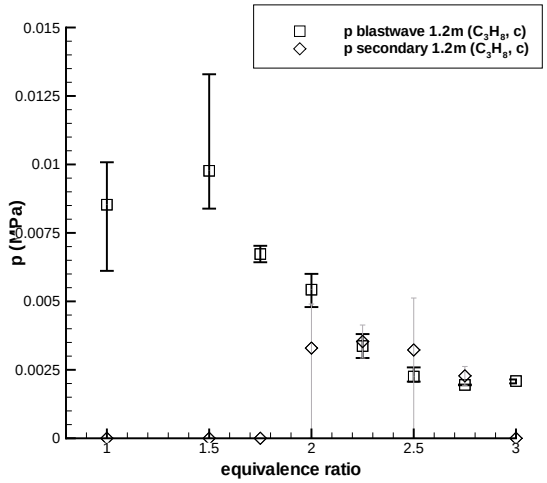

A.1.3: Peak pressure for C_3H_8-O_2 initiator. Center initiation location.

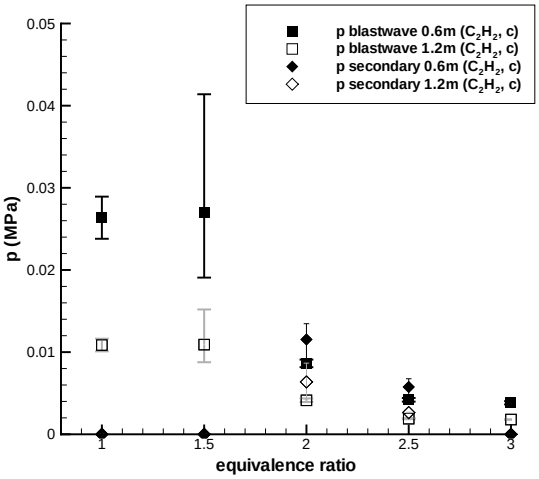

A.1.4: Peak pressure for C_2H_2-O_2 initiator. Center initiation location.

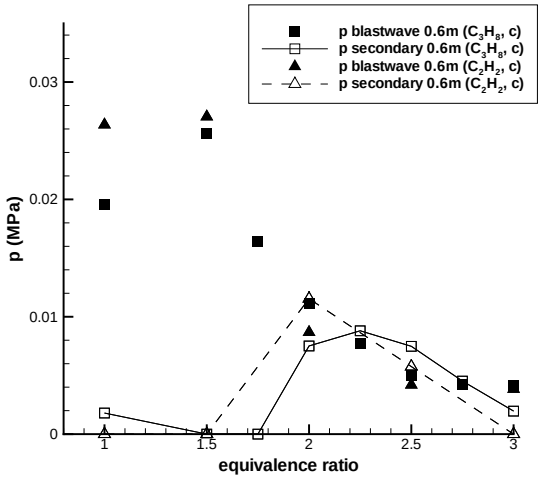

A.1.5: Peak pressure for C_3H_8-O_2 and C_2H_2-O_2 initiator. 0.6 m. Center initiation location.

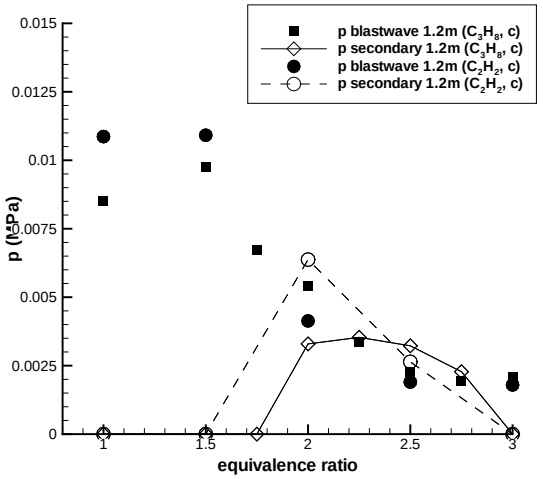

A.1.6: Peak pressure for C_3H_8-O_2 and C_2H_2-O_2 initiator. 1.2 m. Center initiation location.

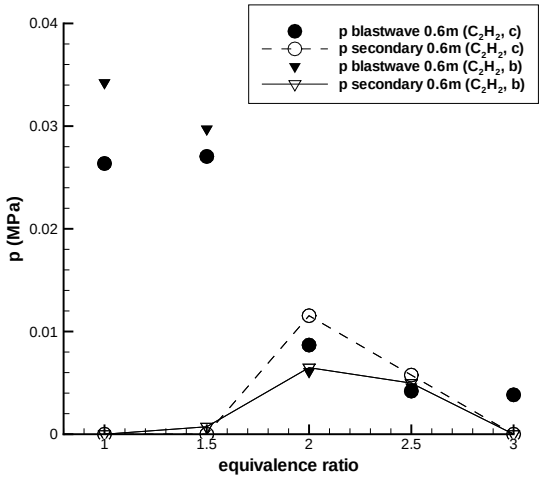

A.1.7: Peak pressure for center and bottom initiation location. 0.6 m. C_2H_2-O_2 initiator mixture.

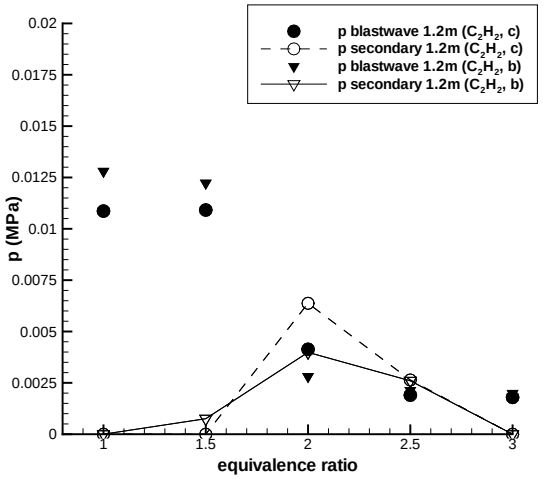

A.1.8: Peak pressure for center and bottom initiation location. 1.2 m. C_2H_2-O_2 initiator mixture.

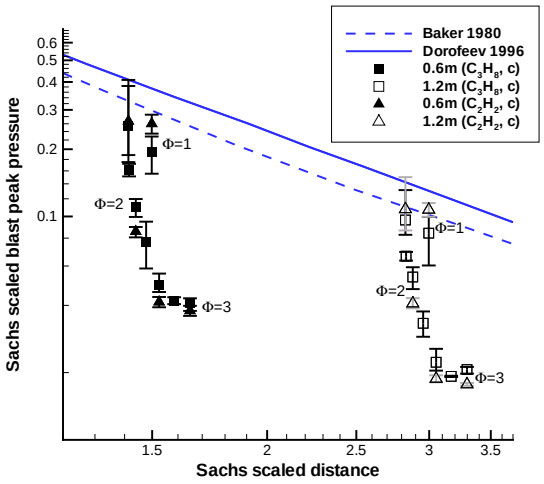

A.1.9: E_1-Sachs-scaled impulse for both initiator mixtures versus Sachs-scaled distance. Center initiation location.

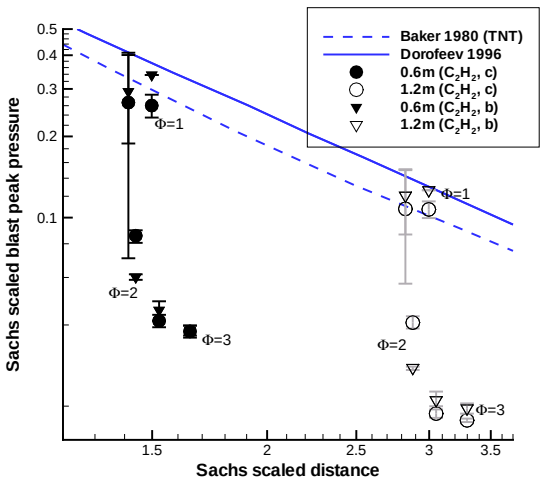

A.1.10: E_1-Sachs-scaled peak pressure for center and bottom initiation location versus Sachs-scaled distance. C_2H_2-O_2 initiator mixture.

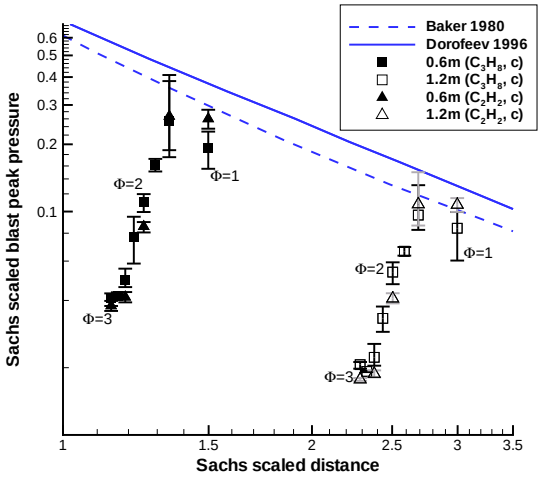

A.1.11: E_2-Sachs-scaled impulse for both initiator mixtures versus Sachs-scaled distance. Center initiation location.

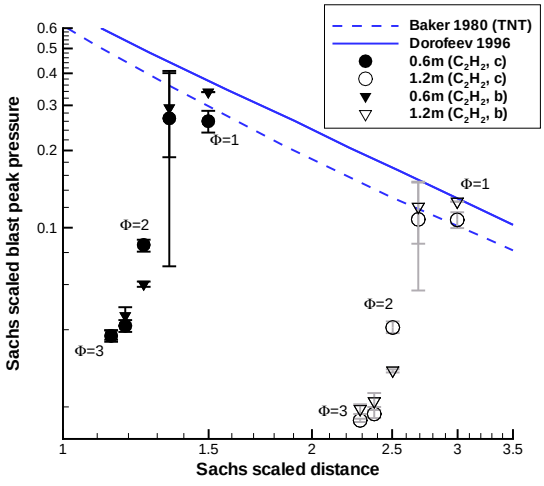

A.1.12: E_2-Sachs-scaled peak pressure for center and bottom initiation location versus Sachs-scaled distance. C_2H_2-O_2 initiator mixture.

A.2 Impulse

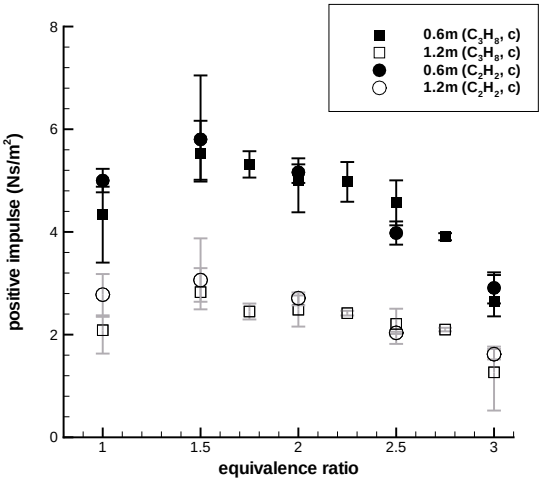

A.2.1: Impulse for both initiator mixtures versus equivalence ratio. Center initiation location.

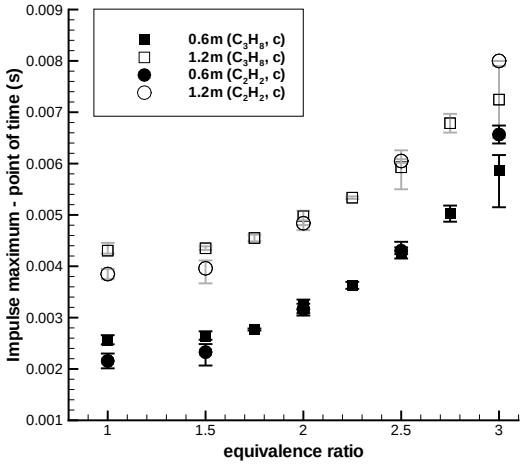

A.2.2: Maximum impulse point in time for both initiator mixtures versus equivalence ratio. Center initiation location.

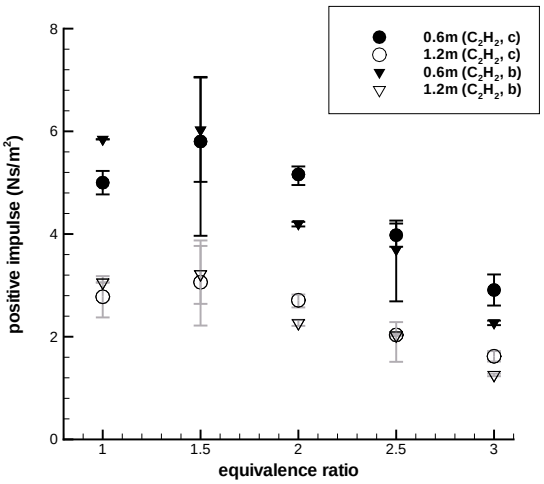

A.2.3: Impulse for both initiation locations versus equivalence ratio. C_2H_2-O_2 initiator mixture.

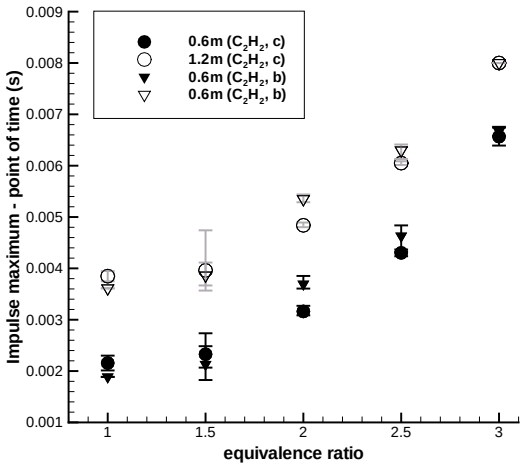

A.2.4: Maximum impulse point in time for both initiation lo actions versus equivalence ratio. C_2H_2-O_2 initiator mixture.

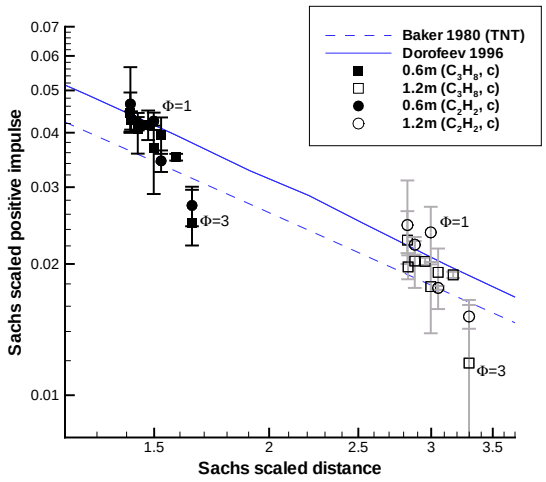

A.2.5: E_1-Sachs-scaled impulse for both initiator mixtures versus Sachs-scaled distance. Center initiation location.

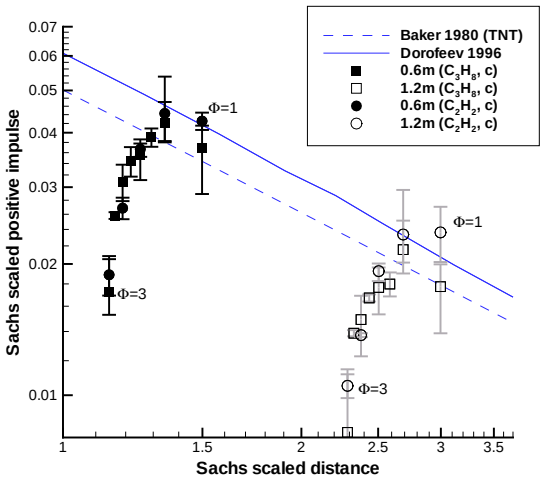

A.2.6: E_2-Sachs-scaled impulse for both initiator mixtures versus Sachs-scaled distance. Center initiation location.

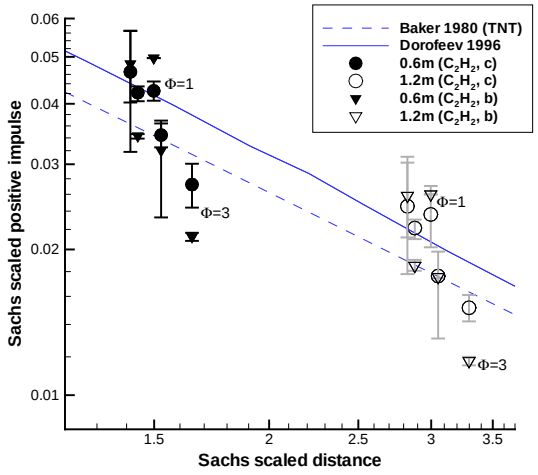

A.2.7: E_1-Sachs-scaled impulse for center and bottom initiation location versus Sachs-scaled distance. C_2H_2-O_2 initiator mixture.

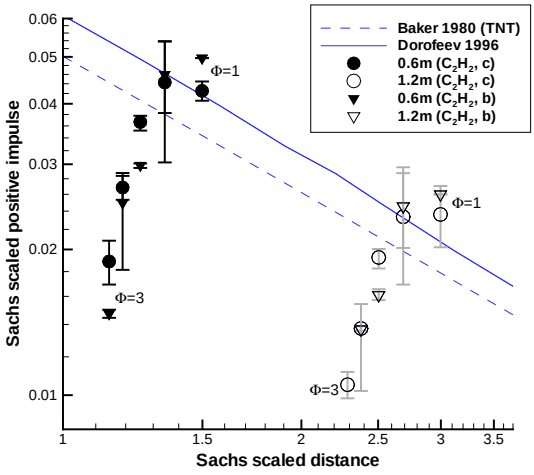

A.2.8: E_2-Sachs-scaled impulse for center and bottom initiation location versus Sachs-scaled distance. C_2H_2-O_2 initiator mixture.

A.3 Time to Secondary Pressure Peak

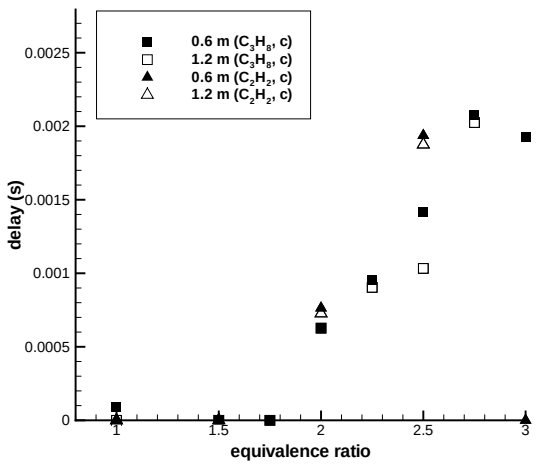

A.3.1: Time to secondary pressure peak for both initiator mixtures versus equivalence ratio. Center initiation location.

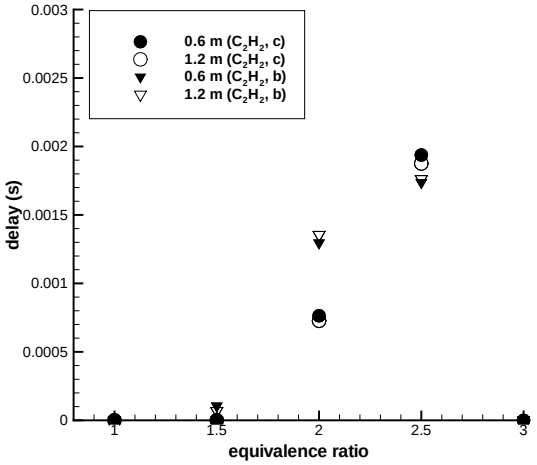

A.3.2: Time to secondary pressure peak for both initiation locations versus equivalence ratio. C_2H_2-O_2 initiator mixture.

A.4 Pressure traces

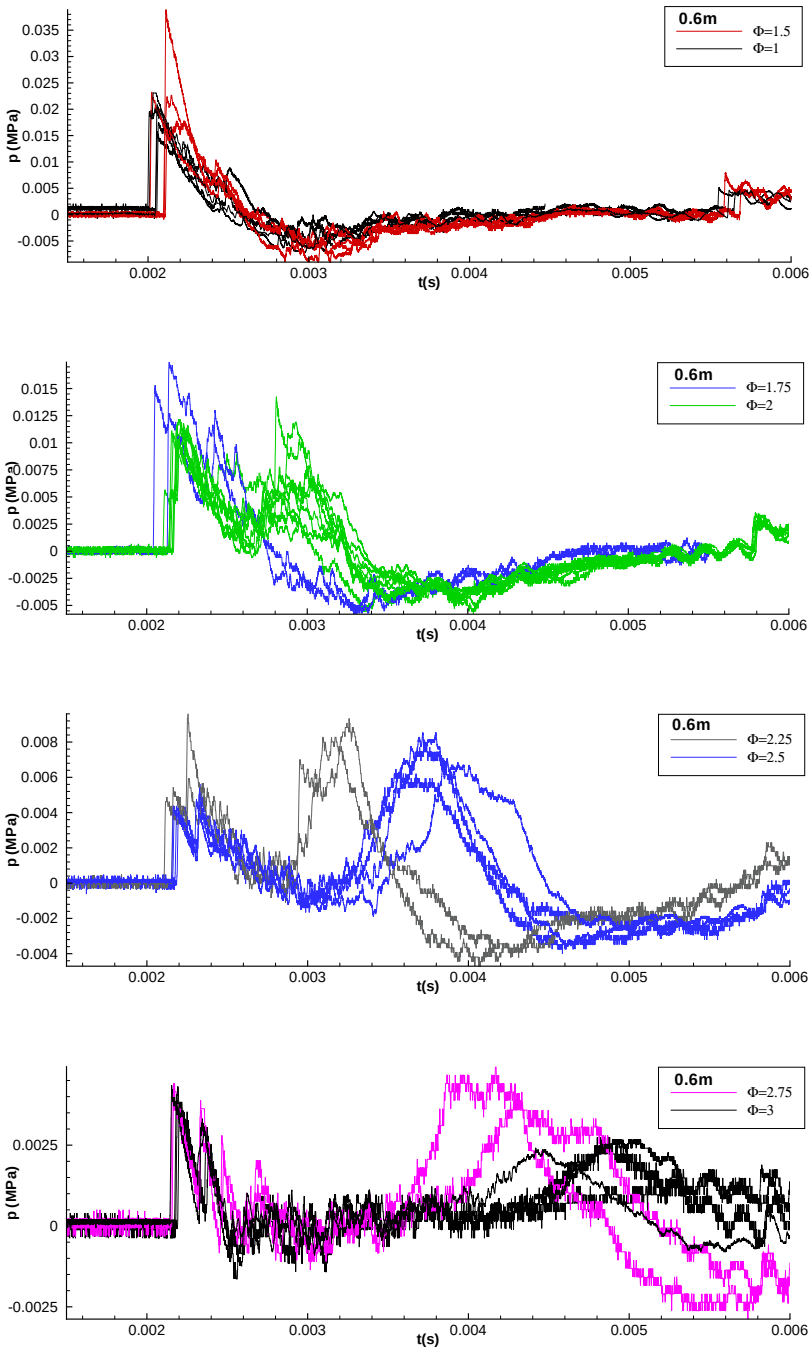

A.4.1: Examples of pressure traces for replica tests obtained from the pencil gauge at 0.6 m. C_3H_8-O_2 initiator mixture. Center initiation location.

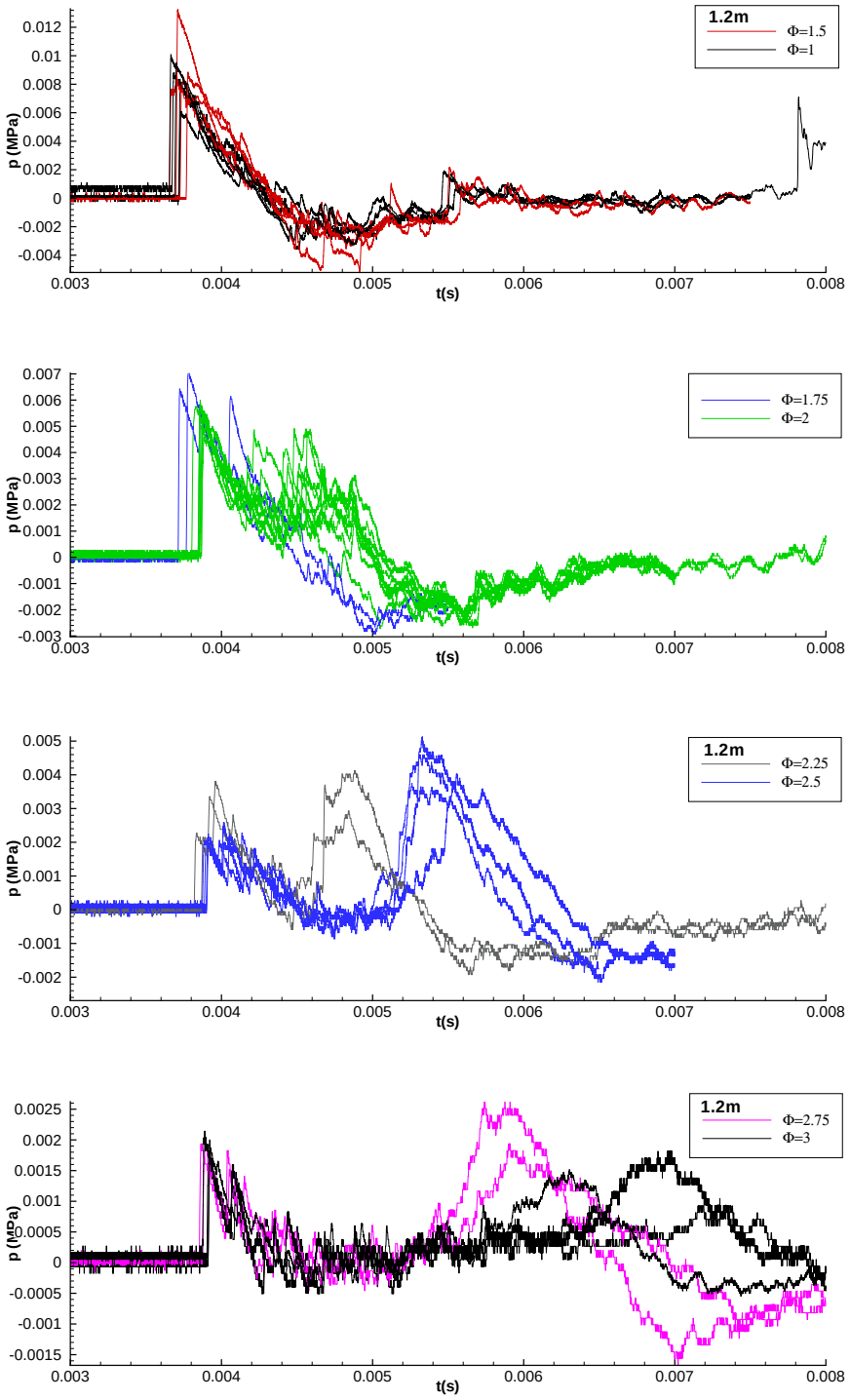

A.4.2: Examples of pressure traces for replica tests obtained from the pencil gauge at 1.2 m. C_3H_8-O_2 initiator. Center initiation location.

A.5 Species shift during expansion

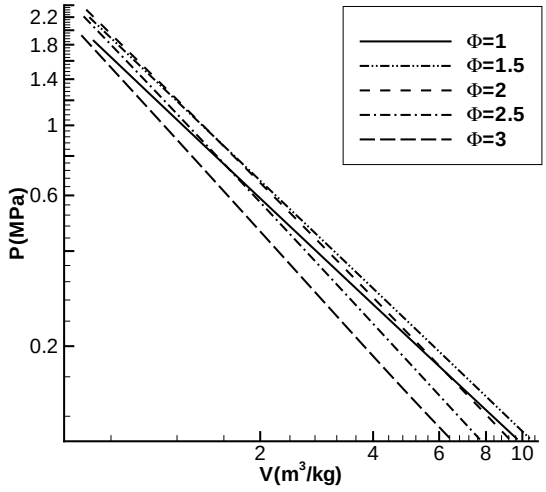

A.5.1: Pressure-volume relationship for chemically-equilibrated isentropic expansion to atmospheric pressure calculated for different equivalence ratios of the primary combustion.

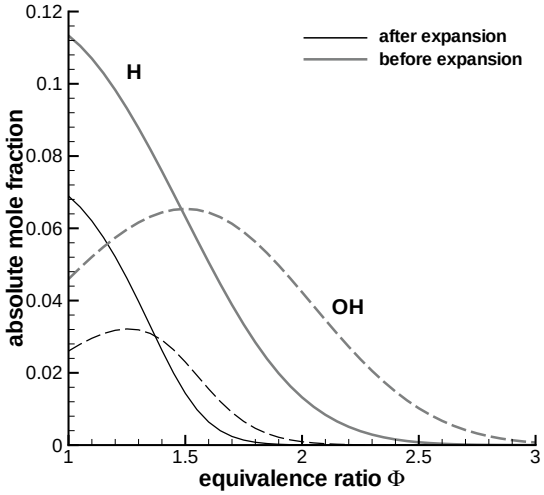

A.5.2: Shift in OH and H mole fraction for chemically-equilibrated isentropic expansion from state 1 to state 2 to atmospheric pressure.

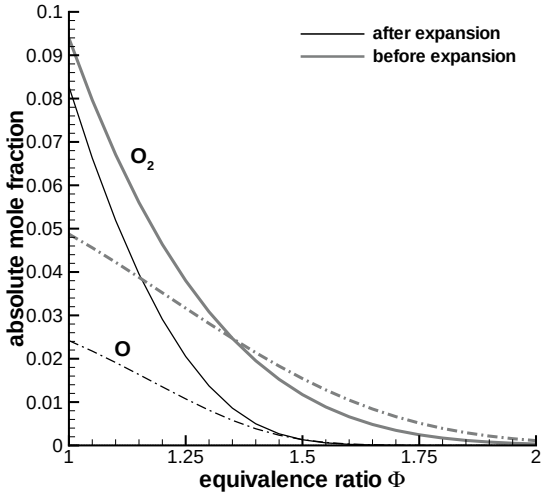

A.5.3: Shift in O_2 and O mole fraction for chemically-equilibrated isentropic expansion from state 1 to state 2 to atmospheric pressure. Note that Φ only ranges from 1 to 2.

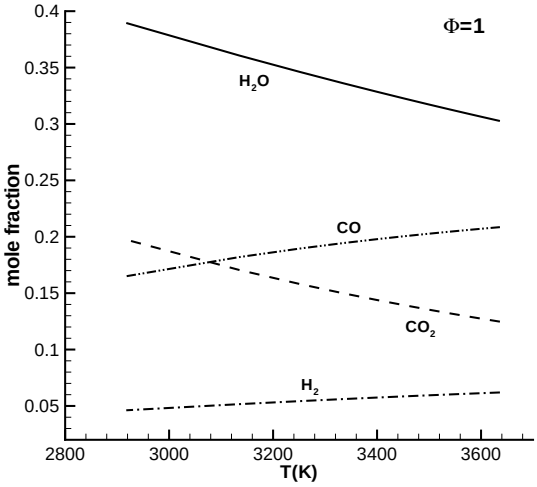

A.5.4: Shift in major species for chemically-equilibrated isentropic expansion from state 1 to state 2 to atmospheric pressure calculated for Φ=1.

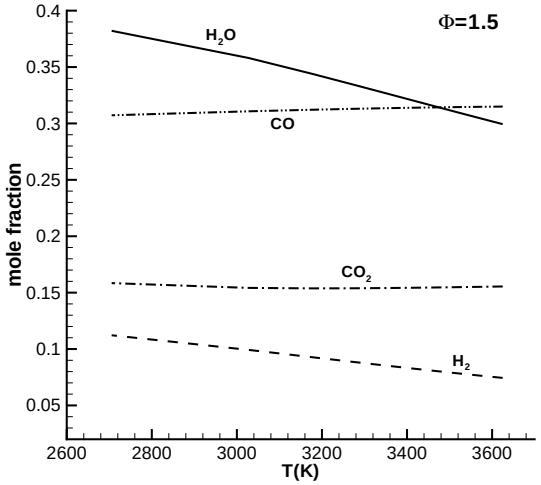

A.5.5: Shift in major species for chemically-equilibrated isentropic expansion from state 1 to state 2 to atmospheric pressure calculated for Φ=1.5.

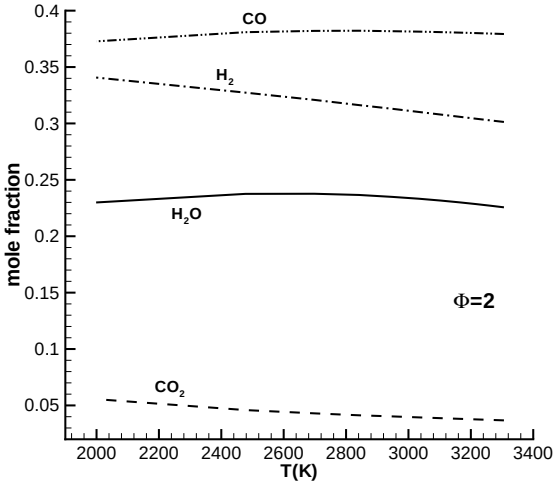

A.5.6: Shift in major species for chemically-equilibrated isentropic expansion from state 1 to state 2 to atmospheric pressure calculated for Φ=2.

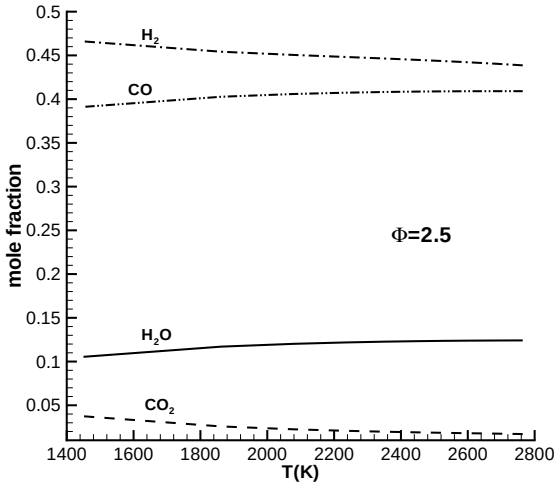

A.5.7: Shift in major species for chemically-equilibrated isentropic expansion from state 1 to state 2 to atmospheric pressure calculated for Φ=2.5.

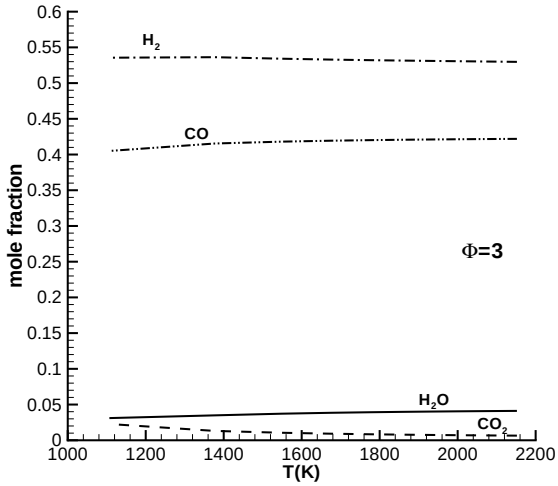

A.5.8: Shift in major species for chemically-equilibrated isentropic expansion from state 1 to state 2 to atmospheric pressure calculated for Φ=3.

A.6 Pencil gauge calibration

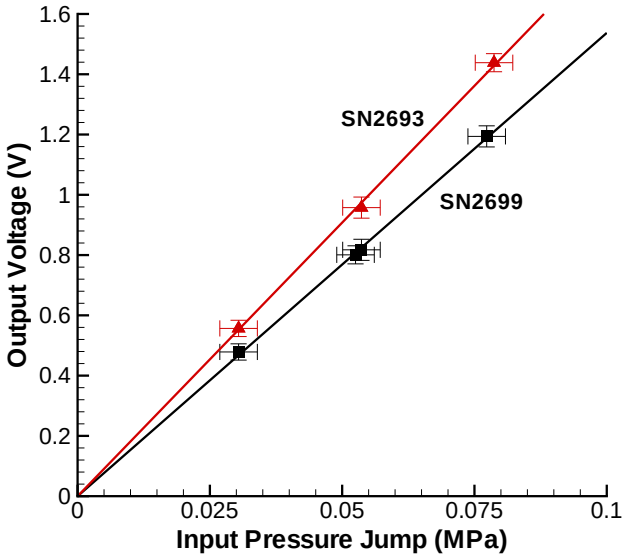

A.6.1: Calibration curves obtained from shock tube experiments for the two pencil gauges used. The shock strength ranging from Mach number 1.1 to 1.3 was calculated from the time of arrival of the shock wave at two pressure transducers in the shock tube wall spaced 0.5 m. Using a least square linear fit the sensitivities are 18.15 mV/kPa (SN2693, 1.2 m) and 15.37 mV/kPa (SN2699, 0.6 m). The errors in the sensitivities are below 5%.

B Highspeed movies

The high speed movies have an interframe time of 89.3 μs. The field of view is 0.57 $\times$ 0.57 m. The time origin of the time stamp given in the bottom right corner of each frame is the discharge of the spark plug in the initiator tube.

All image sequences shown are from experiments using the center initiation location and the C_3H_8-O_2 initiator mixture. The time Δt given for both transducers (0.6 and 1.2 m) is the time the blast wave needs to travel from the balloon edge to the gauge, as derived from Eq.10. The time an acoustic wave needs to travel to the transducers at 0.6 m and 1.2 m is 1.55 ms and 3.33 ms, respectively.

The image sequences are sorted by increasing equivalence ratio.

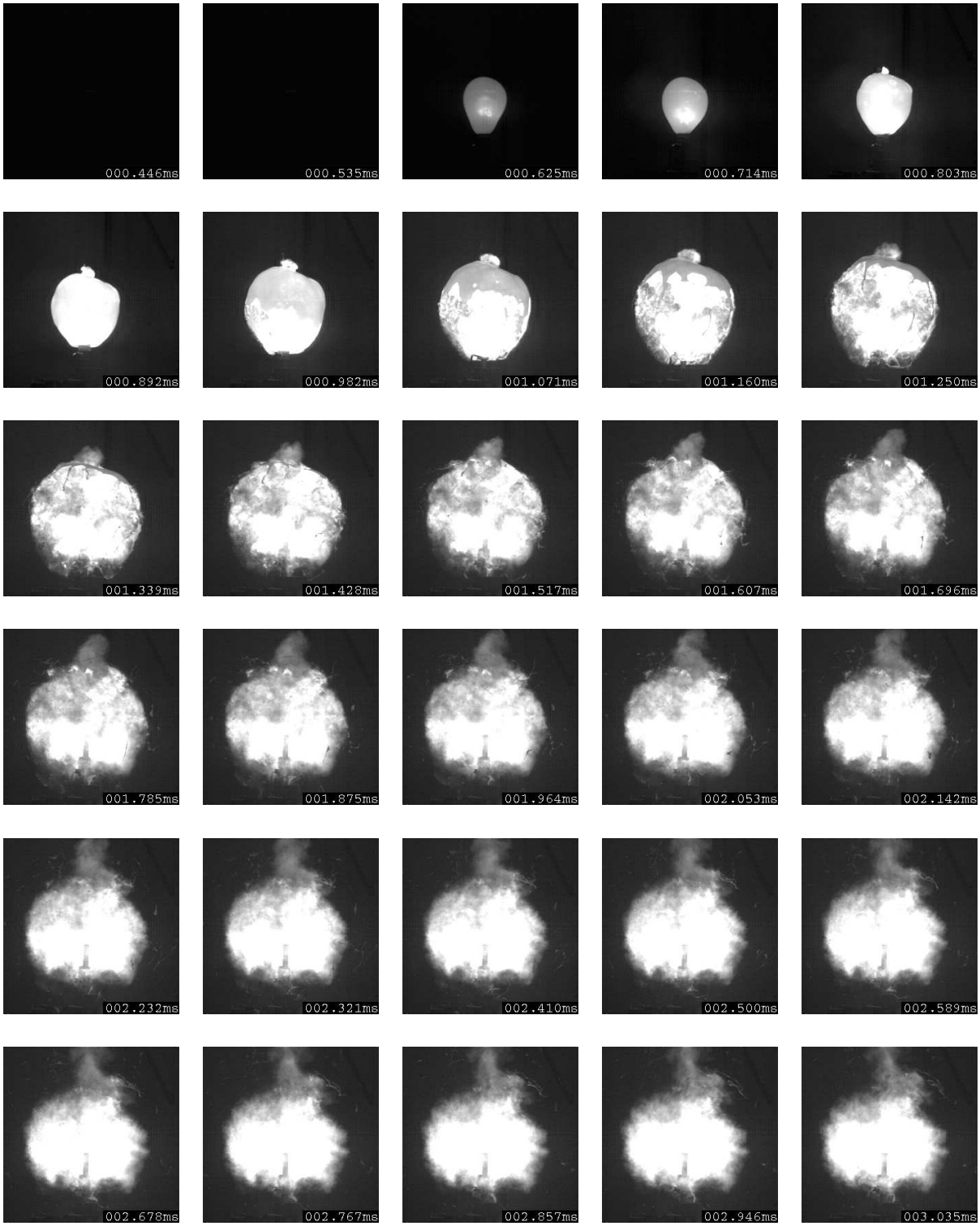

B.1: Shot 113, frames 5 to 34, interframe time: 89 μs, $\Phi = \mathbf{1}$, Δt(0.6 m)=1.08 ms, Δt(1.2 m)=2.65 ms

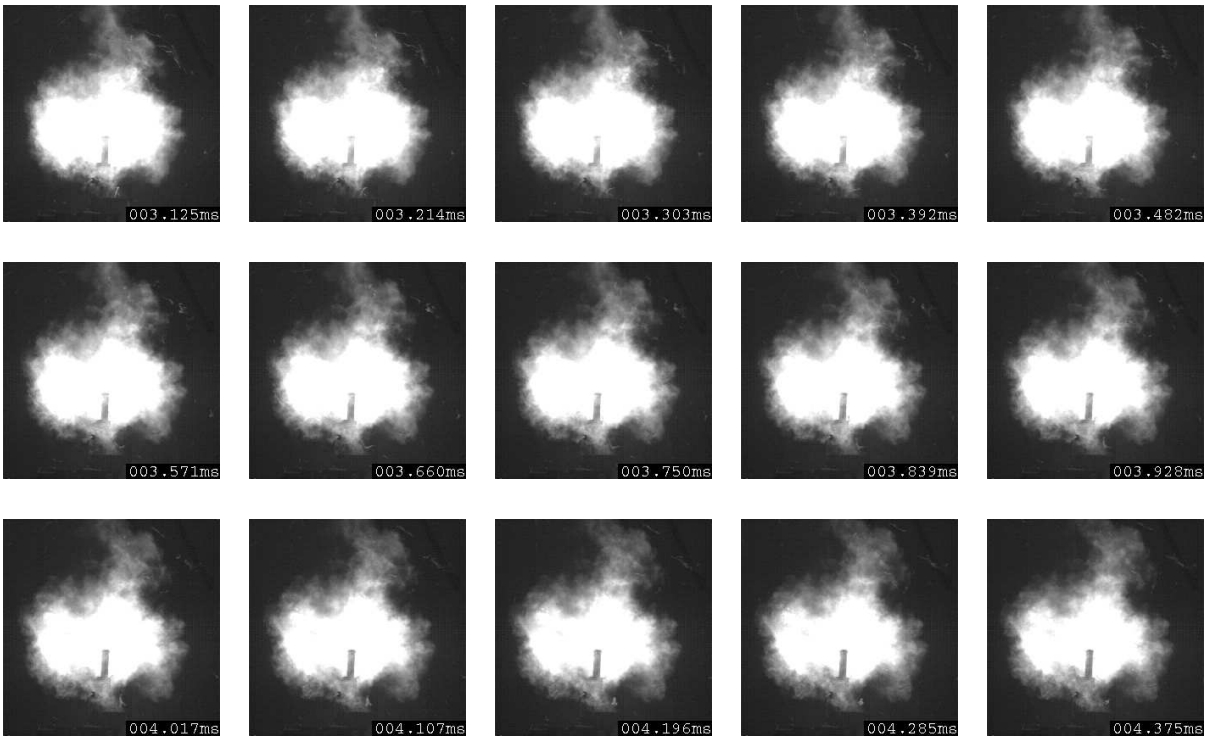

B.2: Shot 113, frames 35 to 49, interframe time: 89 μs, $\Phi = \mathbf{1}$, Δt(0.6 m)=1.29 ms, Δt(1.2 m)=3.02 ms

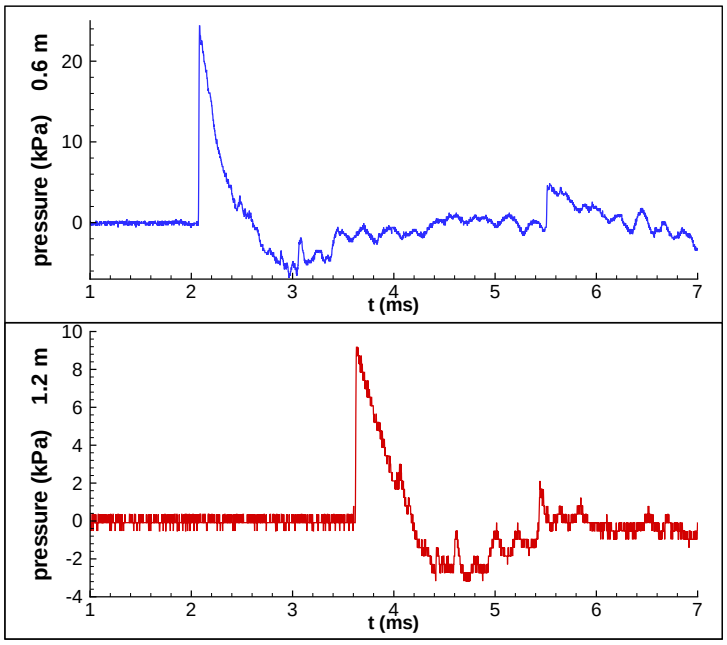

B.3: Shot 113. Pressure traces from the pencil gauges located at 0.6 and 1.2 m.

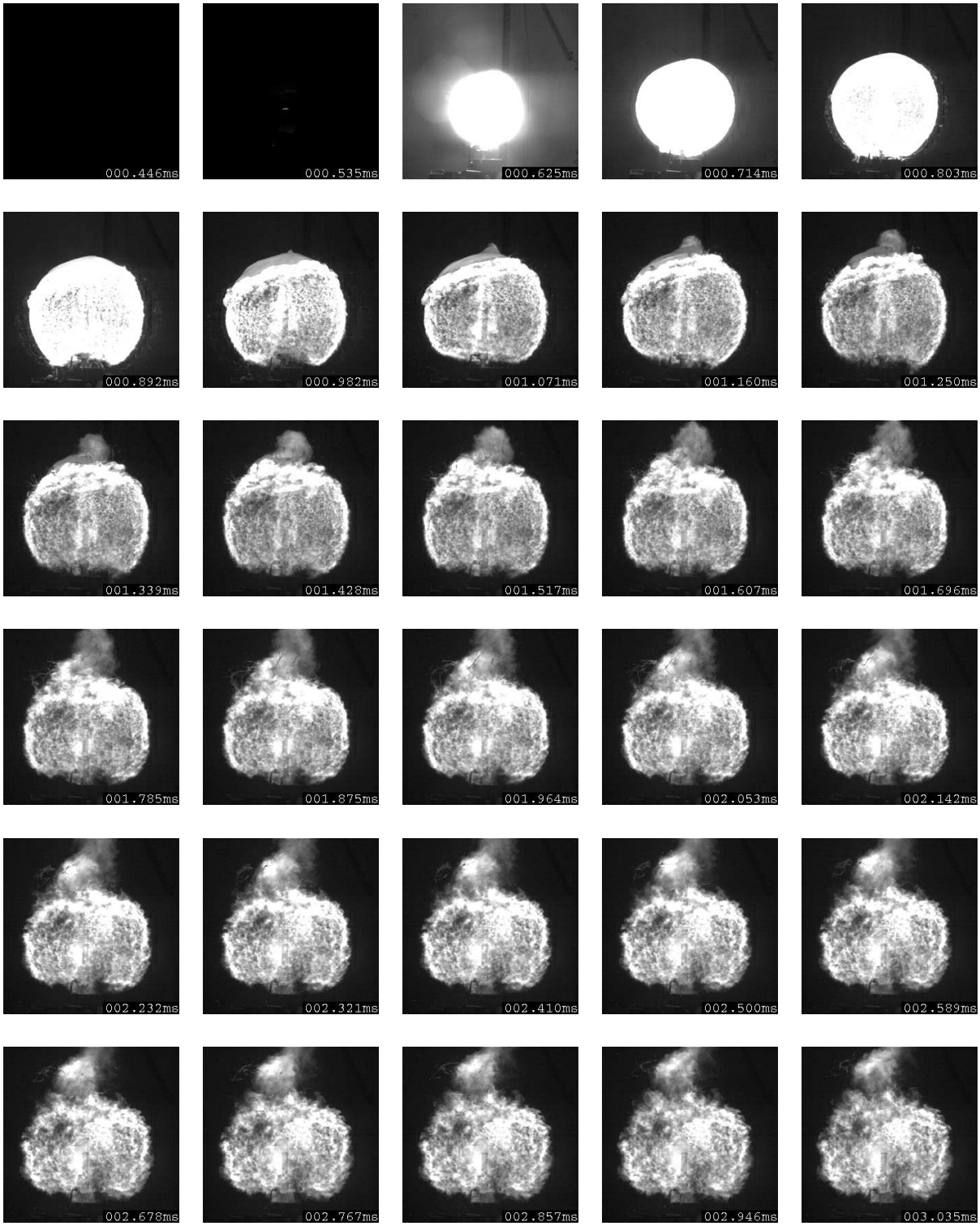

B.4: Shot 110, frames 5 to 34, interframe time: 89 μs, Φ = **1.5**, Δt(0.6 m)=1.09 ms (signal cut off), Δt(1.2 m)=2.45 ms

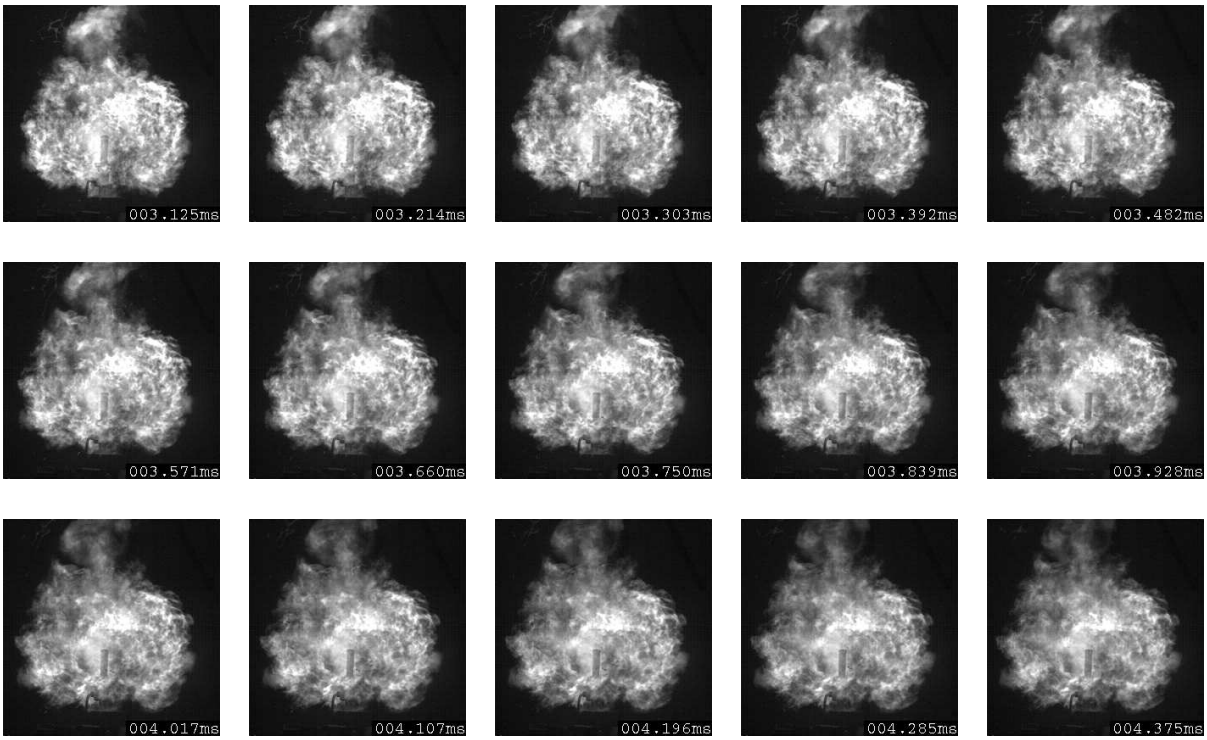

B.5: Shot 110, frames 35 to 49, interframe time: 89 μs, Φ = **1.5**, Δt(0.6 m)=1.3 ms (signal cut off), Δt(1.2 m)=2.9 ms

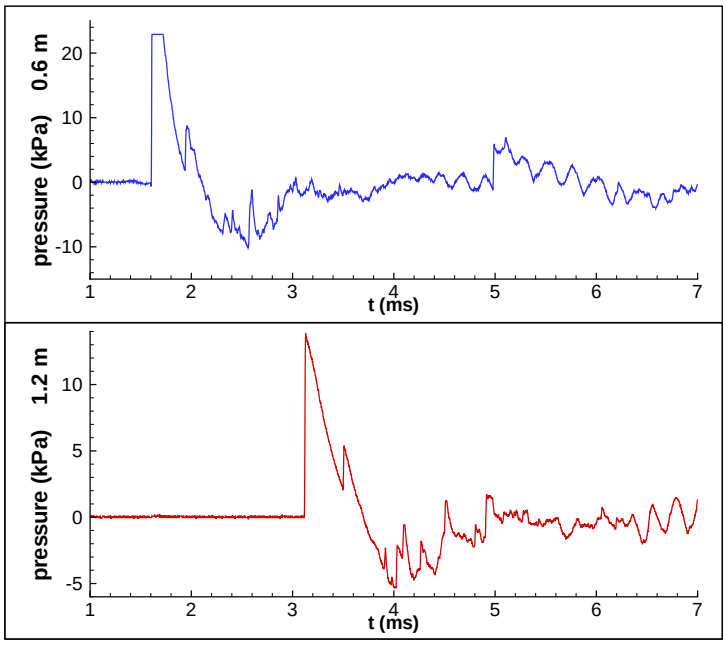

B.6: Shot 110. Pressure traces from the pencil gauges located at 0.6 and 1.2 m.

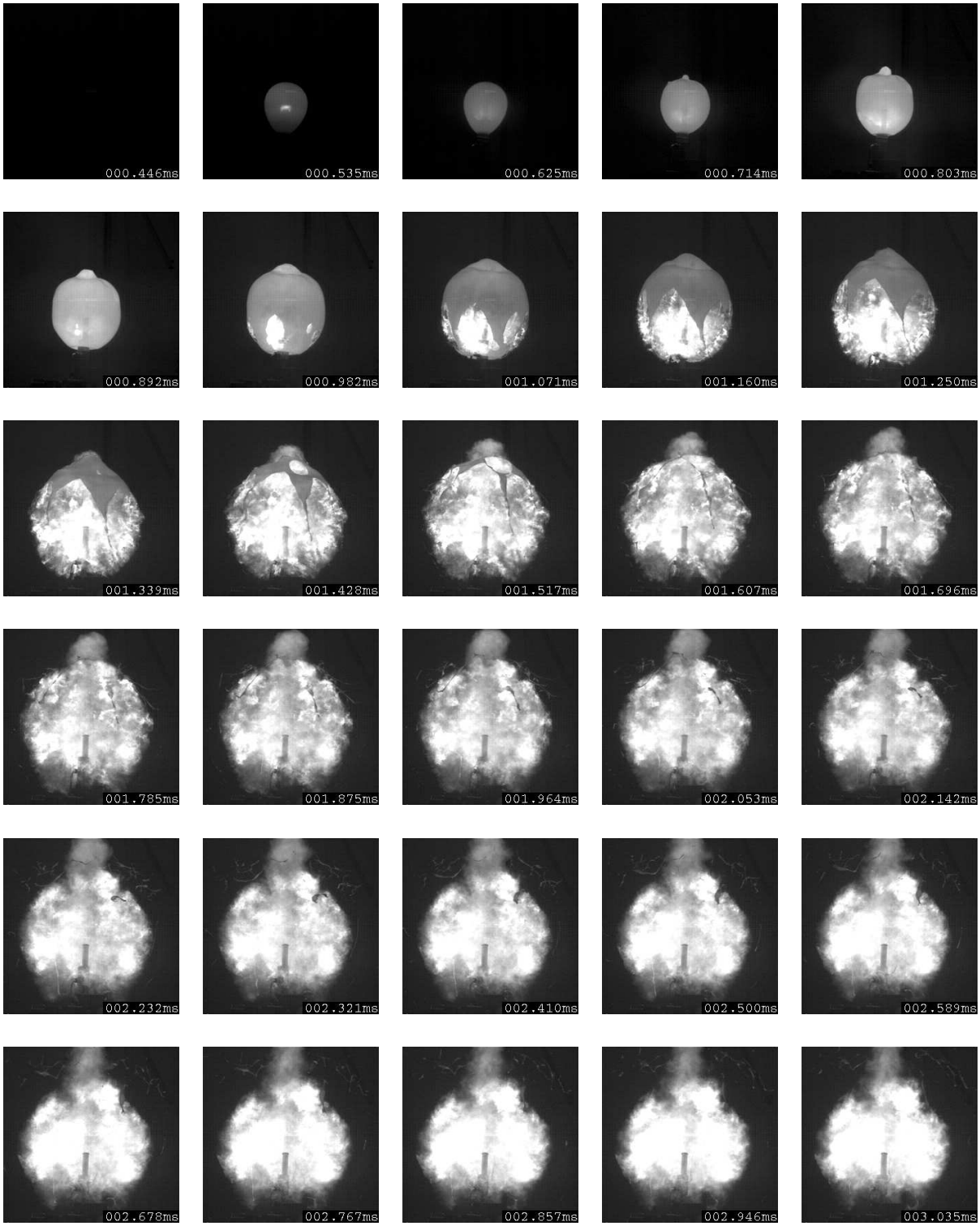

B.7: Shot 111, frames 5 to 34, interframe time: 89 μs, $\Phi = \mathbf{1.5}$, Δt(0.6 m)=1.17 ms, Δt(1.2 m)=2.69 ms

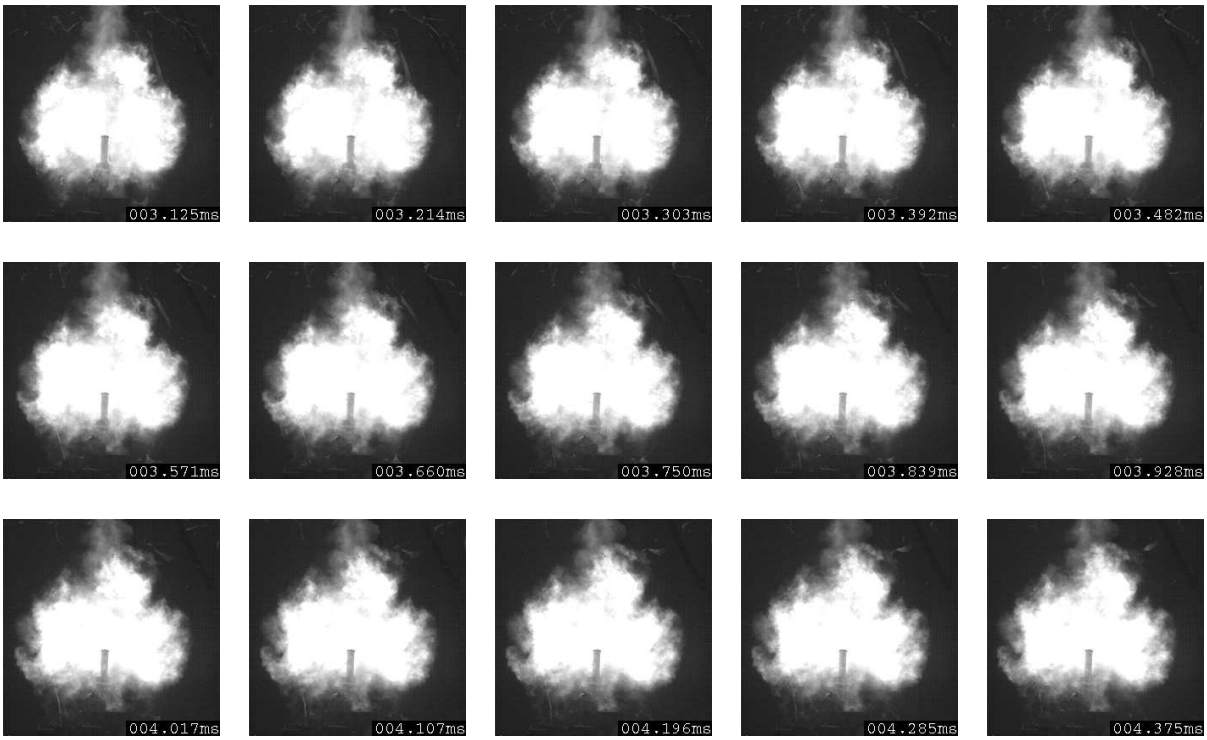

B.8: Shot 111, frames 35 to 49, interframe time: 89 μs, Φ = **1.5**, Δt(0.6 m)=1.35 ms, Δt(1.2 m)=3.04 ms

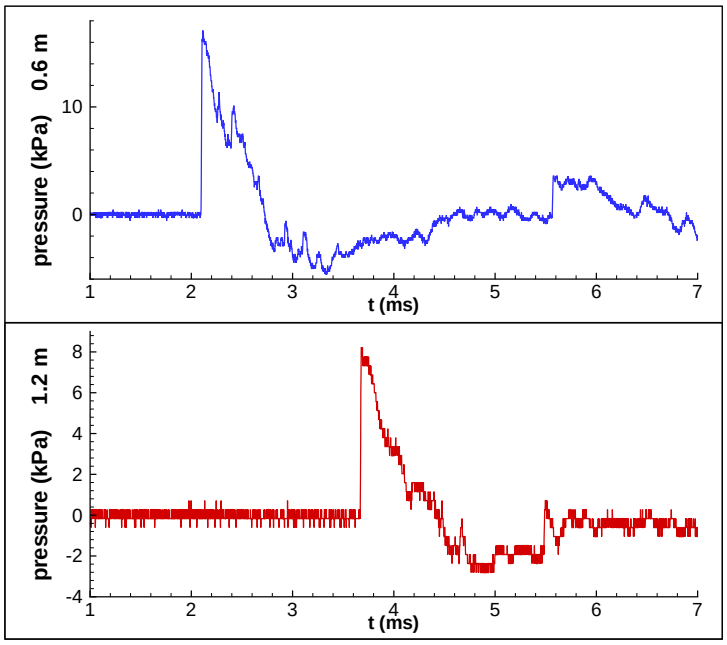

B.9: Shot 111. Pressure traces from the pencil gauges located at 0.6 and 1.2 m.

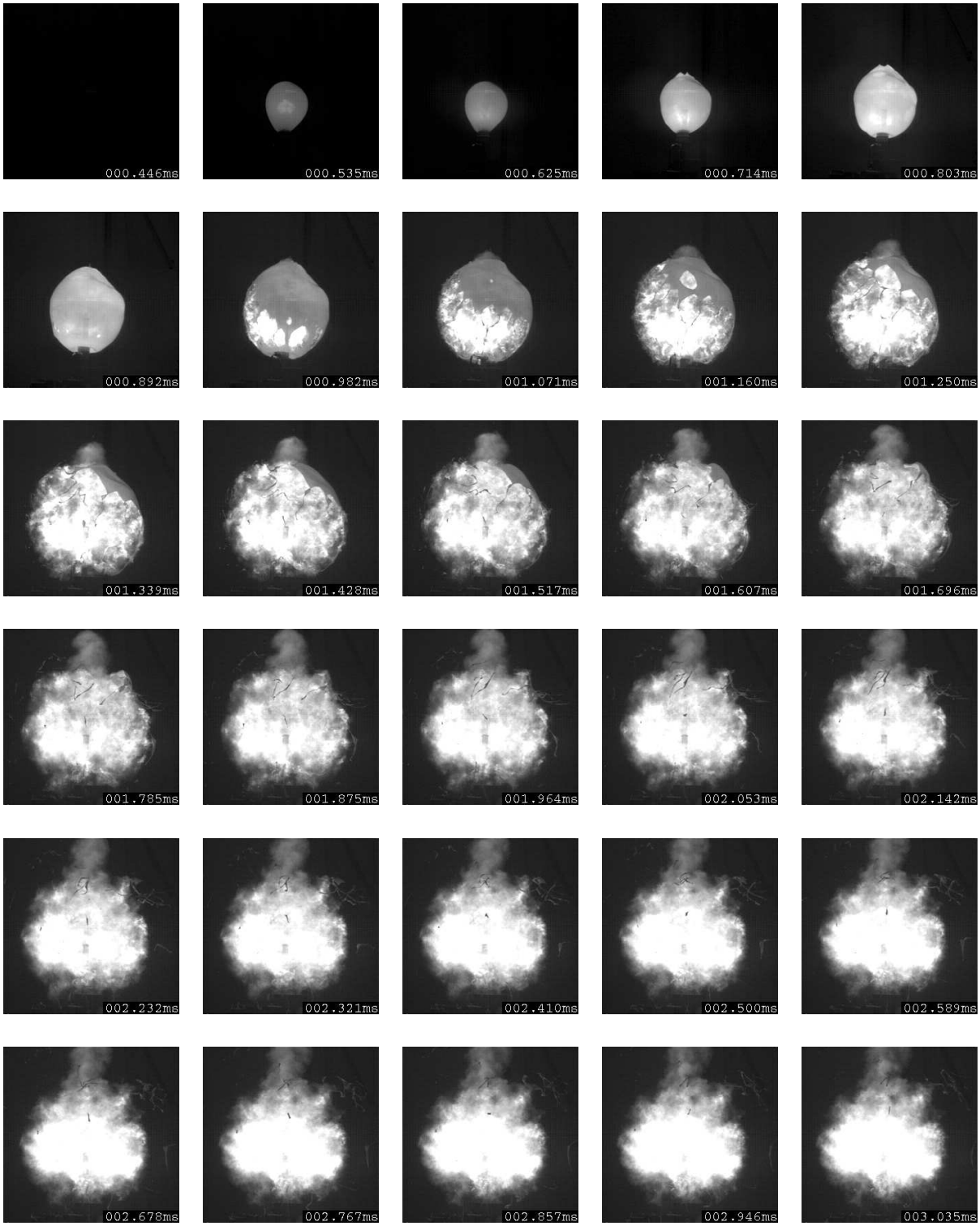

B.10: Shot 112, frames 5 to 34, interframe time: 89 μs, $\Phi = \mathbf{1.5}$, Δt(0.6 m)=1.16 ms, Δt(1.2 m)=2.69 ms

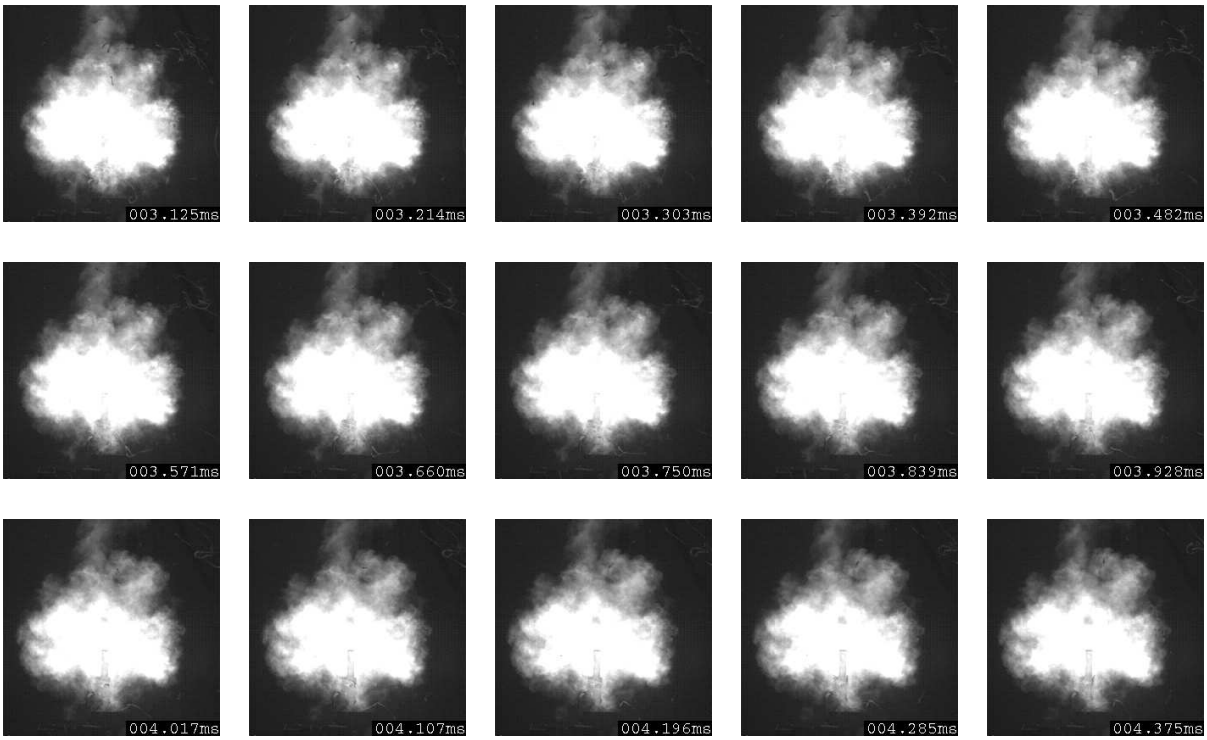

B.11: Shot 112, frames 35 to 49, interframe time: 89 μs, Φ = **1.5**, Δt(0.6 m)=1.34 ms, Δt(1.2 m)=3.04 ms

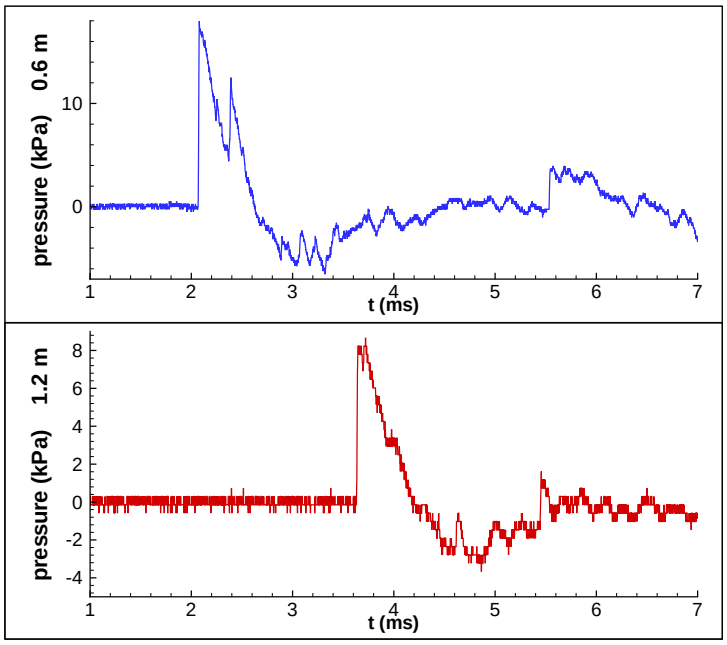

B.12: Shot 112. Pressure traces from the pencil gauges located at 0.6 and 1.2 m.

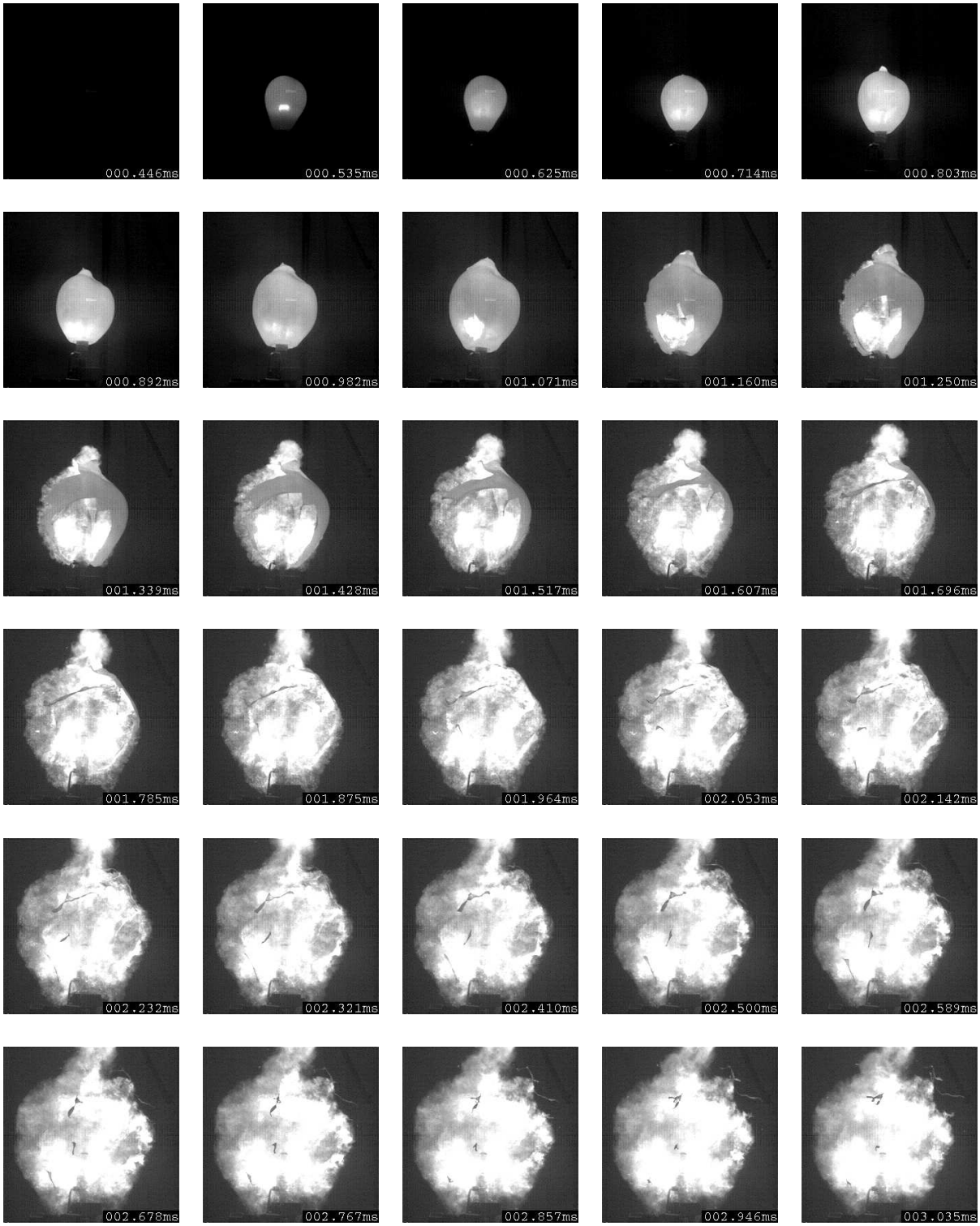

B.13: Shot 107, frames 5 to 34, interframe time: 89 μs, $\Phi = \mathbf{2}$, Δt(0.6 m)=1.29 ms, Δt(1.2 m)=2.95 ms

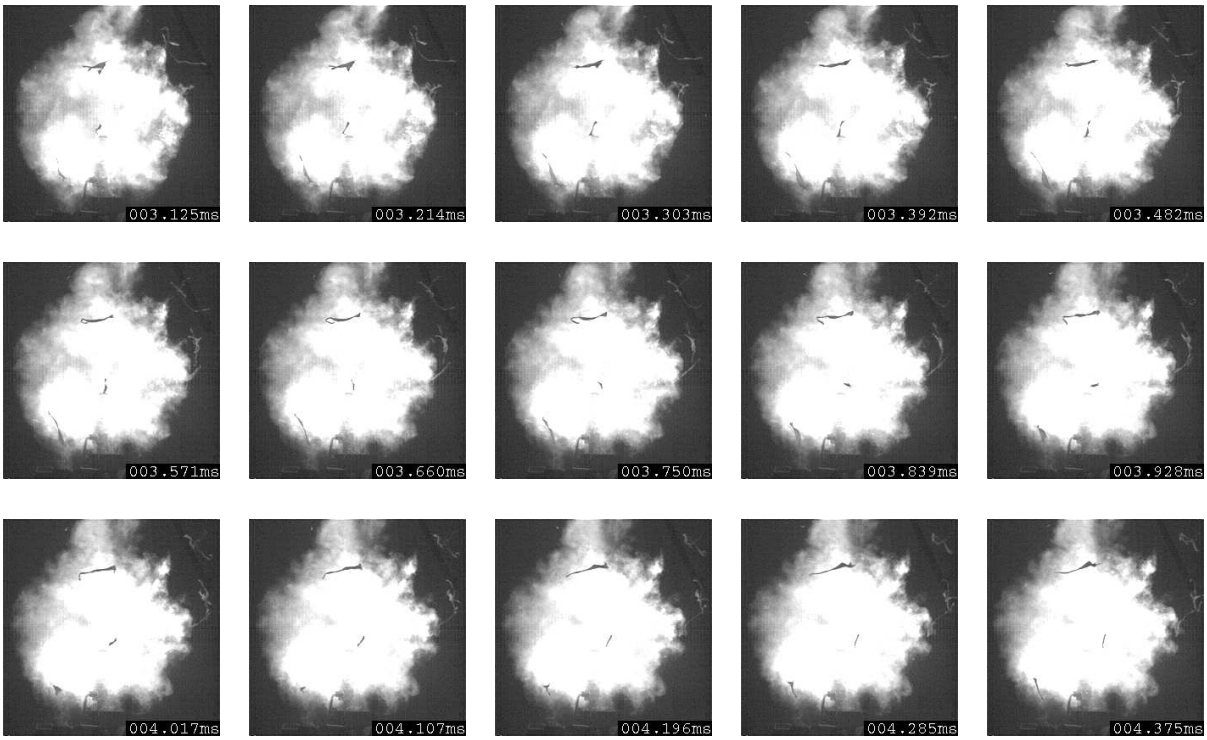

B.14: Shot 107, frames 35 to 49, interframe time: 89 μs, Φ = **2**, Δt(0.6 m)=1.43 ms, Δt(1.2 m)=3.17 ms

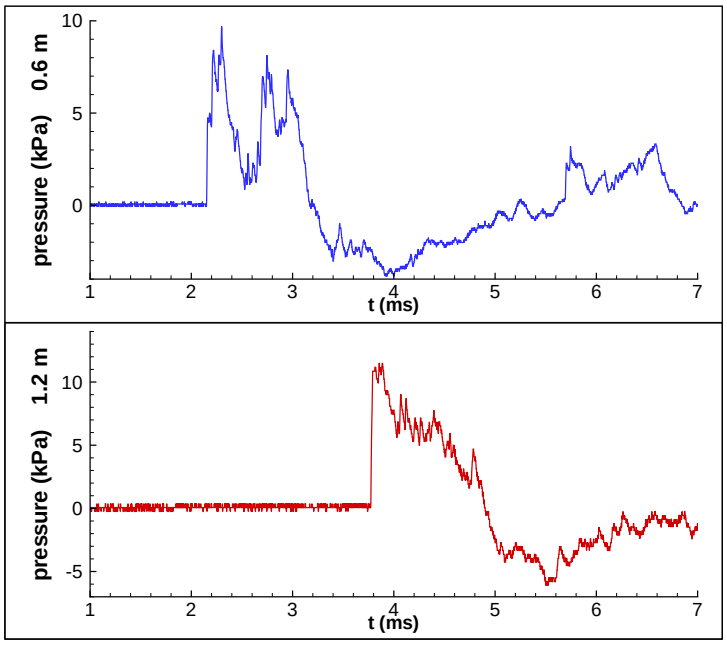

B.15: Shot 107. Pressure traces from the pencil gauges located at 0.6 and 1.2 m.

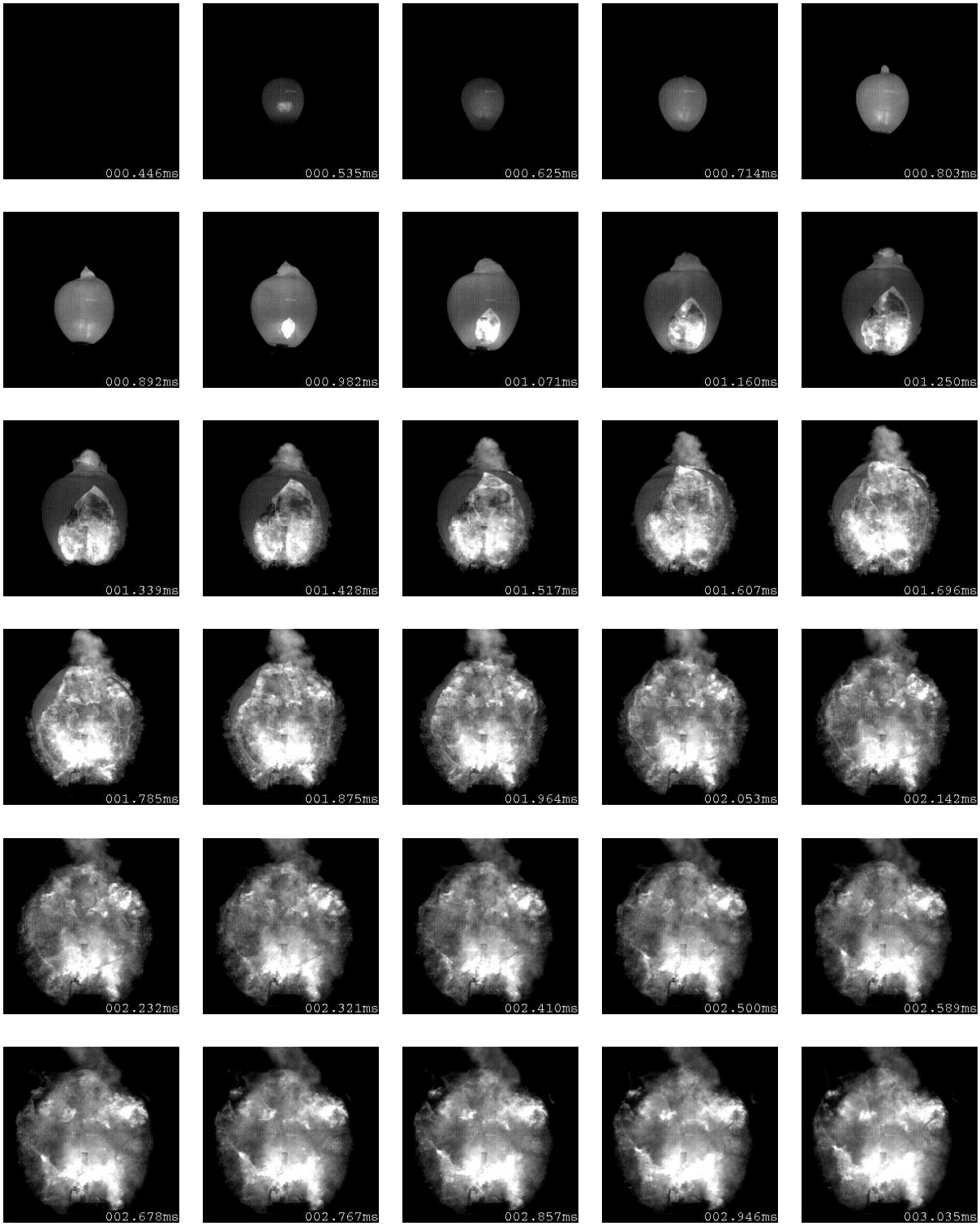

B.16: Shot 108, frames 5 to 34, interframe time: 89 μs, $\Phi = \mathbf{2}$, Δt(0.6 m)=1.31 ms, Δt(1.2 m)=2.91 ms

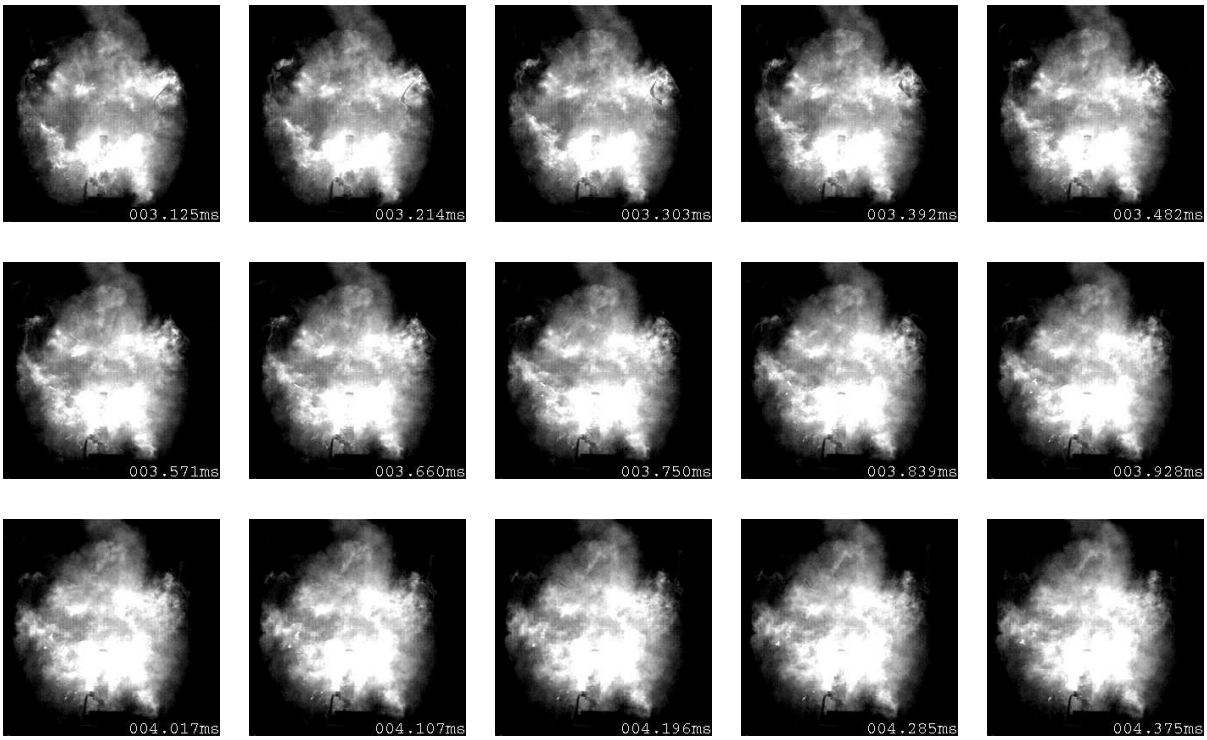

B.17: Shot 108, frames 35 to 49, interframe time: 89 μs, Φ = **2**, Δt(0.6 m)=1.44 ms, Δt(1.2 m)=3.15 ms

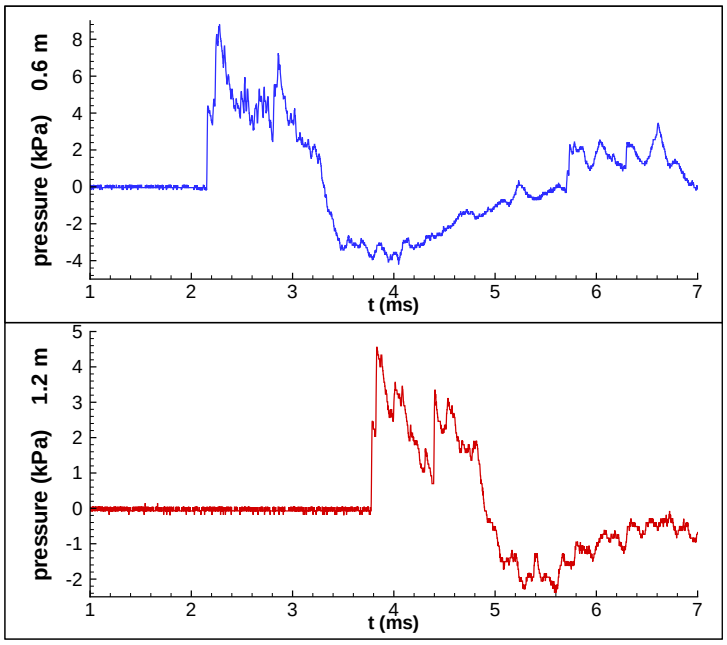

B.18: Shot 108. Pressure traces from the pencil gauges located at 0.6 and 1.2 m.

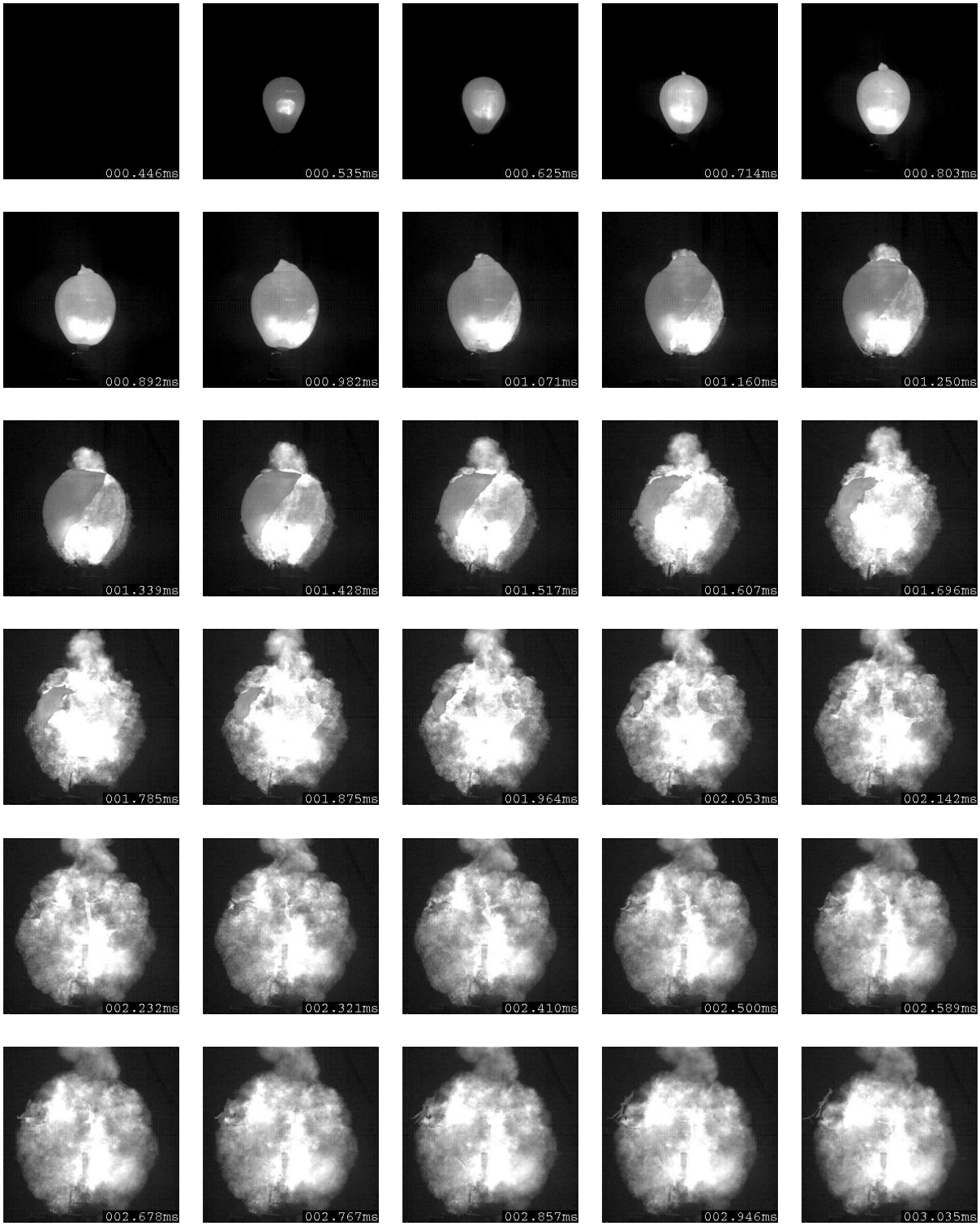

B.19: Shot 109, frames 5 to 34, interframe time: 89 μs, $\Phi = \mathbf{2}$, Δt(0.6 m)=1.30 ms, Δt(1.2 m)=2.87 ms

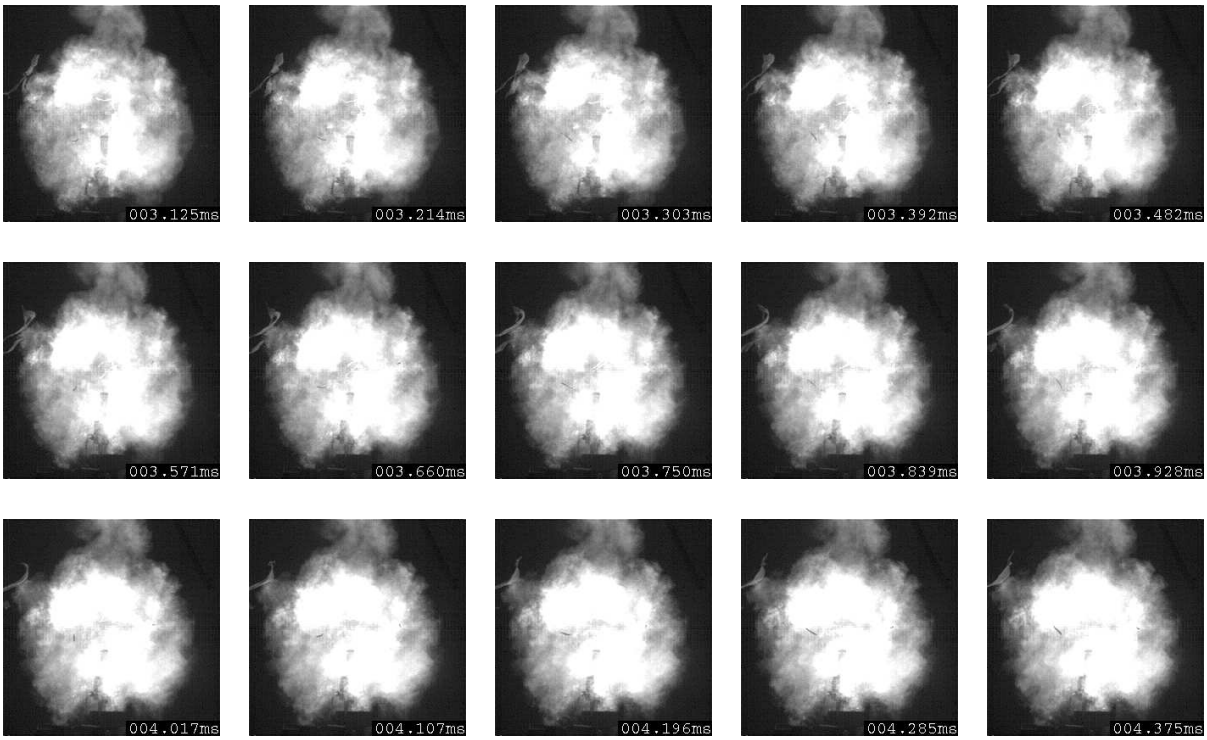

B.20: Shot 109, frames 35 to 49, interframe time: 89 μs, Φ = **2**, Δt(0.6 m)=1.43 ms, Δt(1.2 m)=3.14 ms

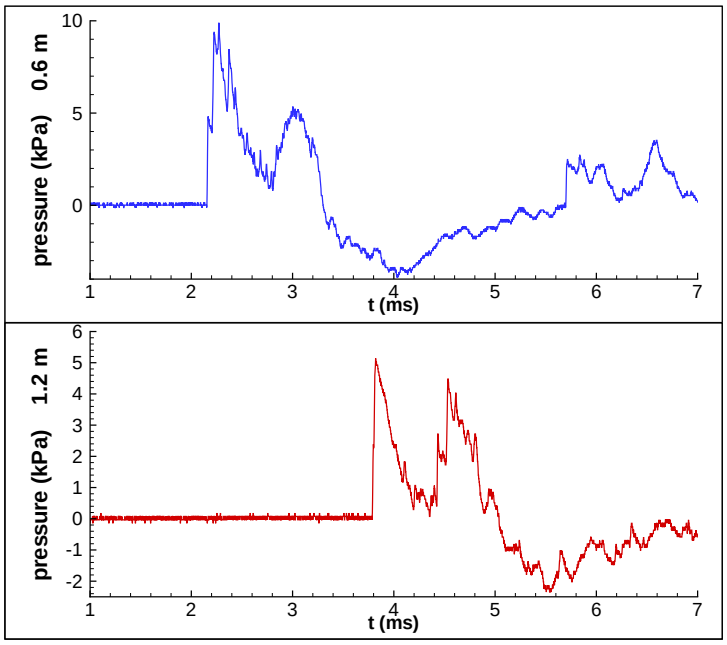

B.21: Shot 109. Pressure traces from the pencil gauges located at 0.6 and 1.2 m.

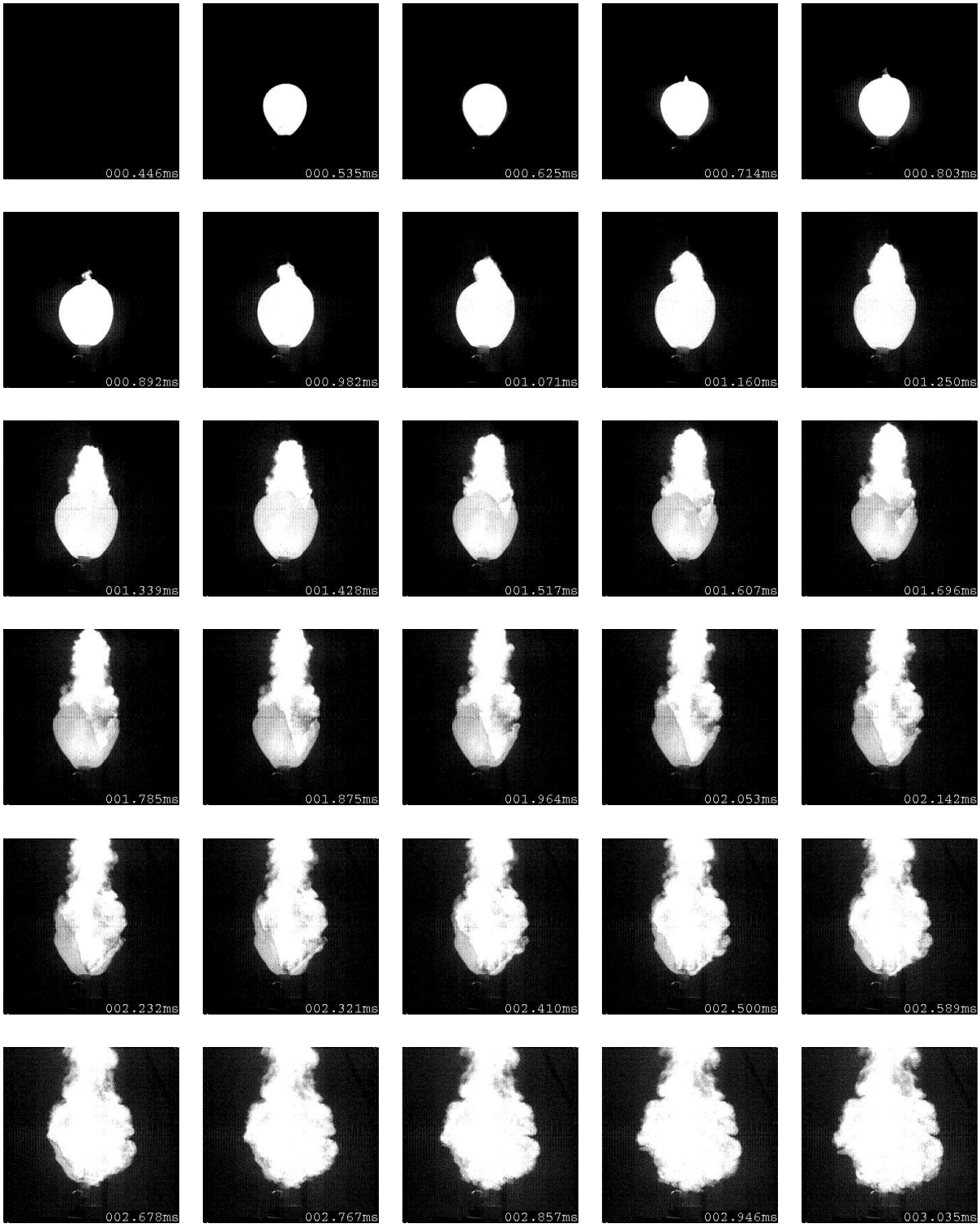

B.22: Shot 103, frames 5 to 34, interframe time: 89 μs, $\Phi = \mathbf{2.5}$, Δt(0.6 m)=1.40 ms, Δt(1.2 m)=3.10 ms

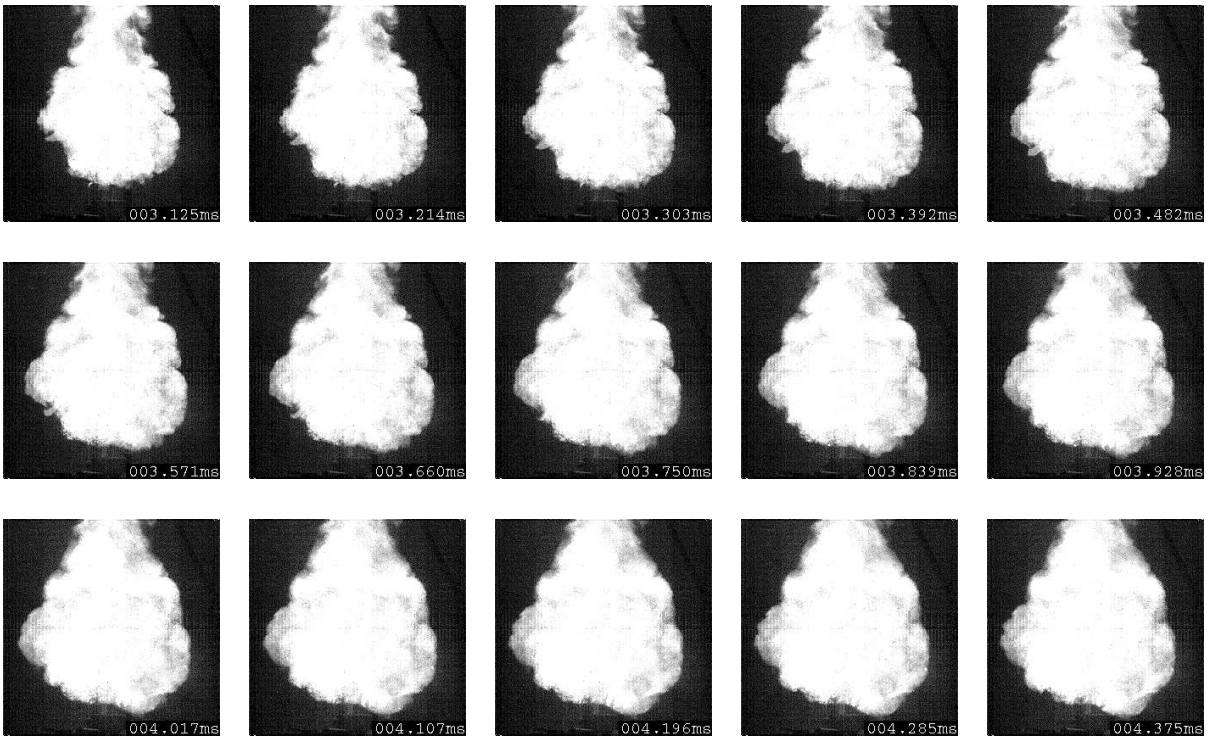

B.23: Shot 103, frames 35 to 49, interframe time: 89 μs, Φ = **2.5**, Δt(0.6 m)=1.49 ms, Δt(1.2 m)=3.24 ms

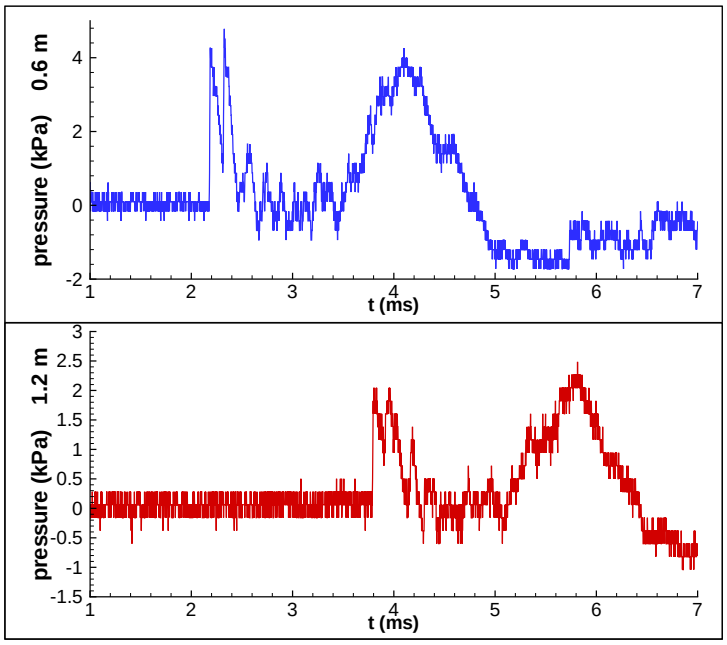

B.24: Shot 103. Pressure traces from the pencil gauges located at 0.6 and 1.2 m.

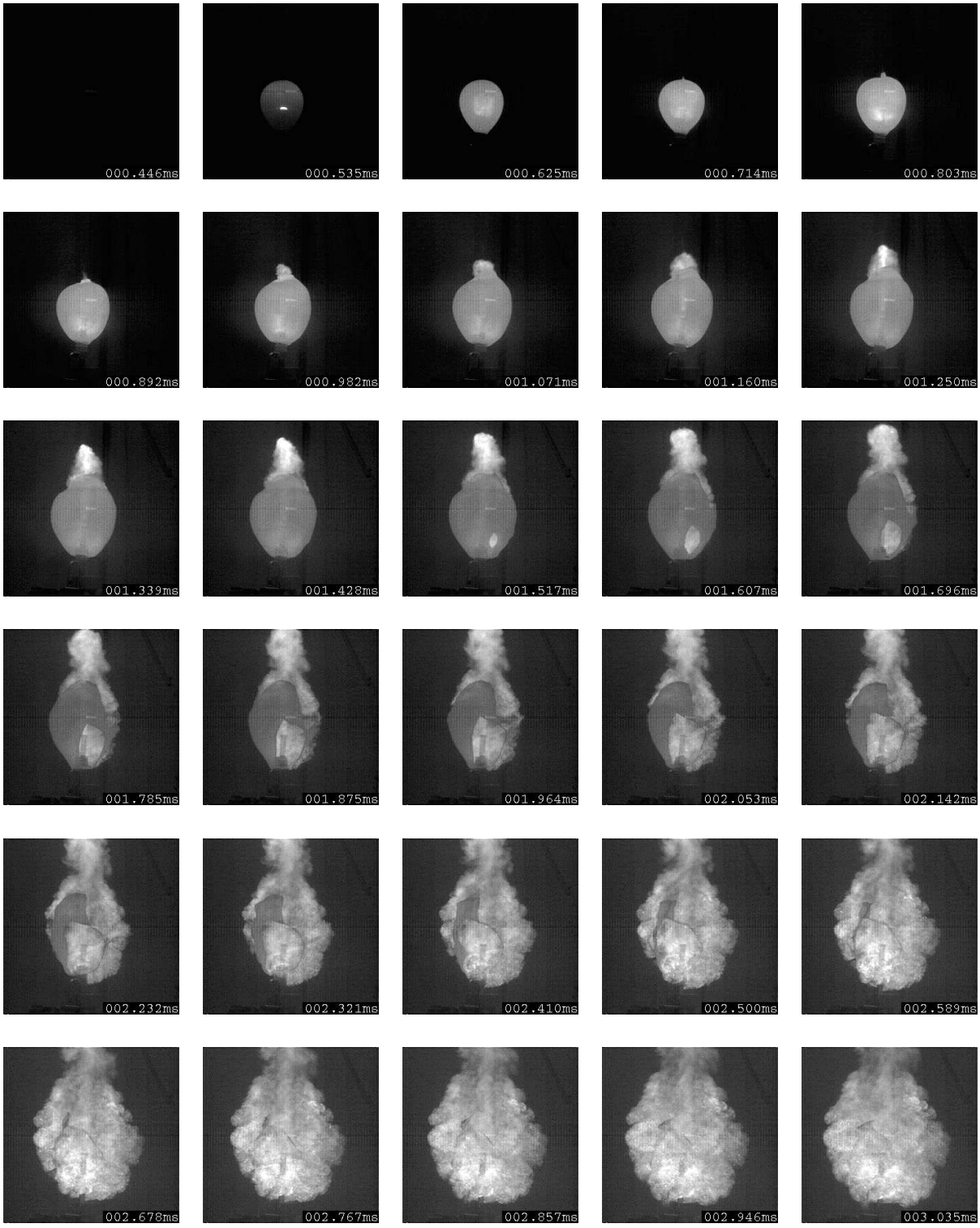

B.25: Shot 104, frames 5 to 34, interframe time: 89 μs, Φ = **2.5**, Δt(0.6 m)=1.41 ms, Δt(1.2 m)=3.07 ms

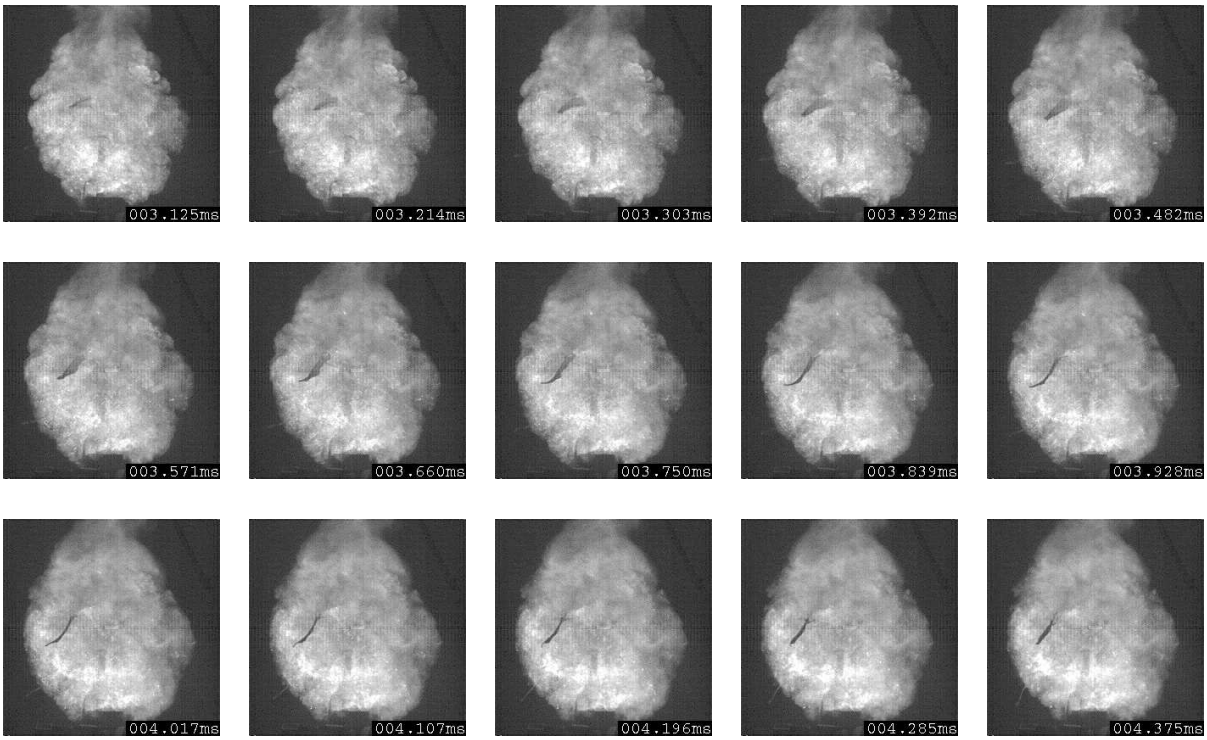

B.26: Shot 104, frames 35 to 49, interframe time: 89 μs, Φ = **2.5**, Δt(0.6 m)=1.49 ms, Δt(1.2 m)=3.22 ms

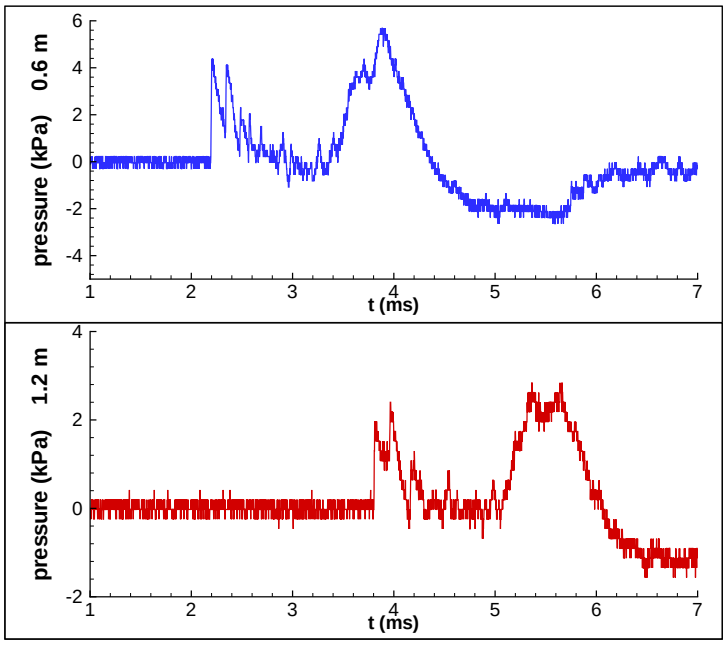

B.27: Shot 104. Pressure traces from the pencil gauges located at 0.6 and 1.2 m.

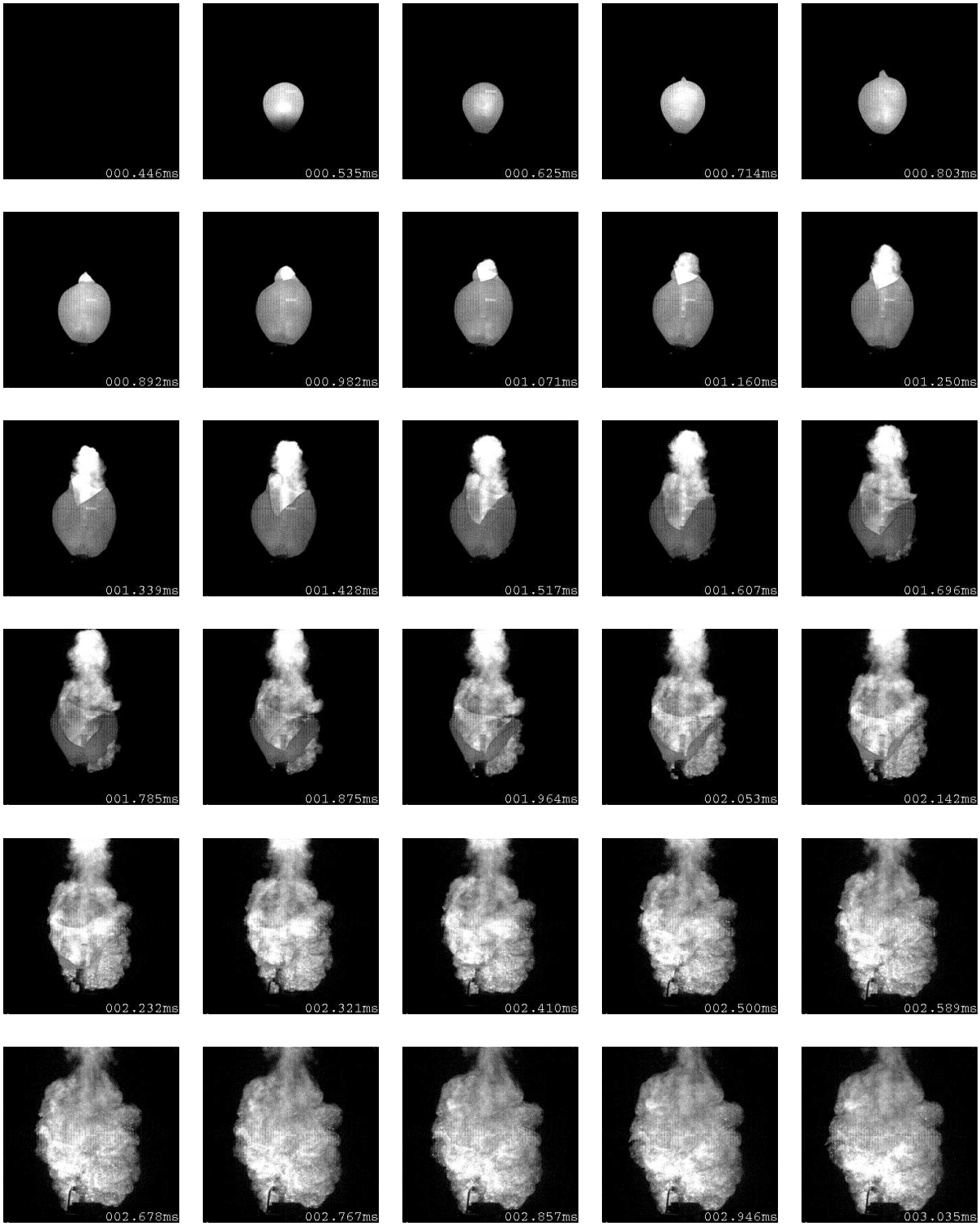

B.28: Shot 105, frames 5 to 34, interframe time: 89 μs, Φ = **2.5**, Δt(0.6 m)=1.39 ms, Δt(1.2 m)=3.08 ms

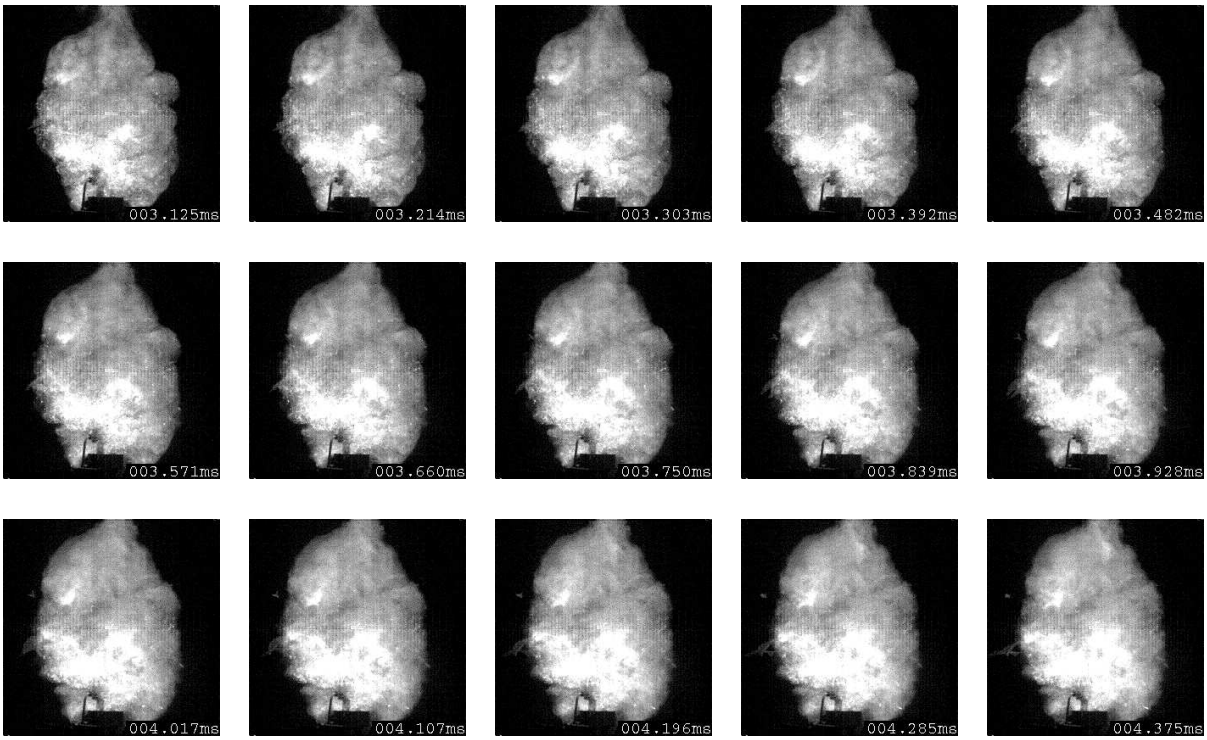

B.29: Shot 105, frames 35 to 49, interframe time: 89 μs, Φ = **2.5**, Δt(0.6 m)=1.48 ms, Δt(1.2 m)=3.23 ms

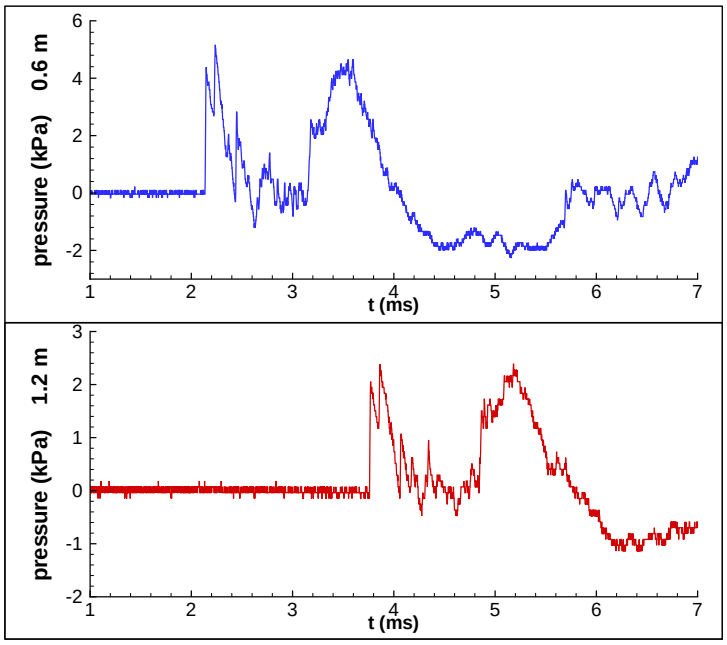

B.30: Shot 105. Pressure traces from the pencil gauges located at 0.6 and 1.2 m.

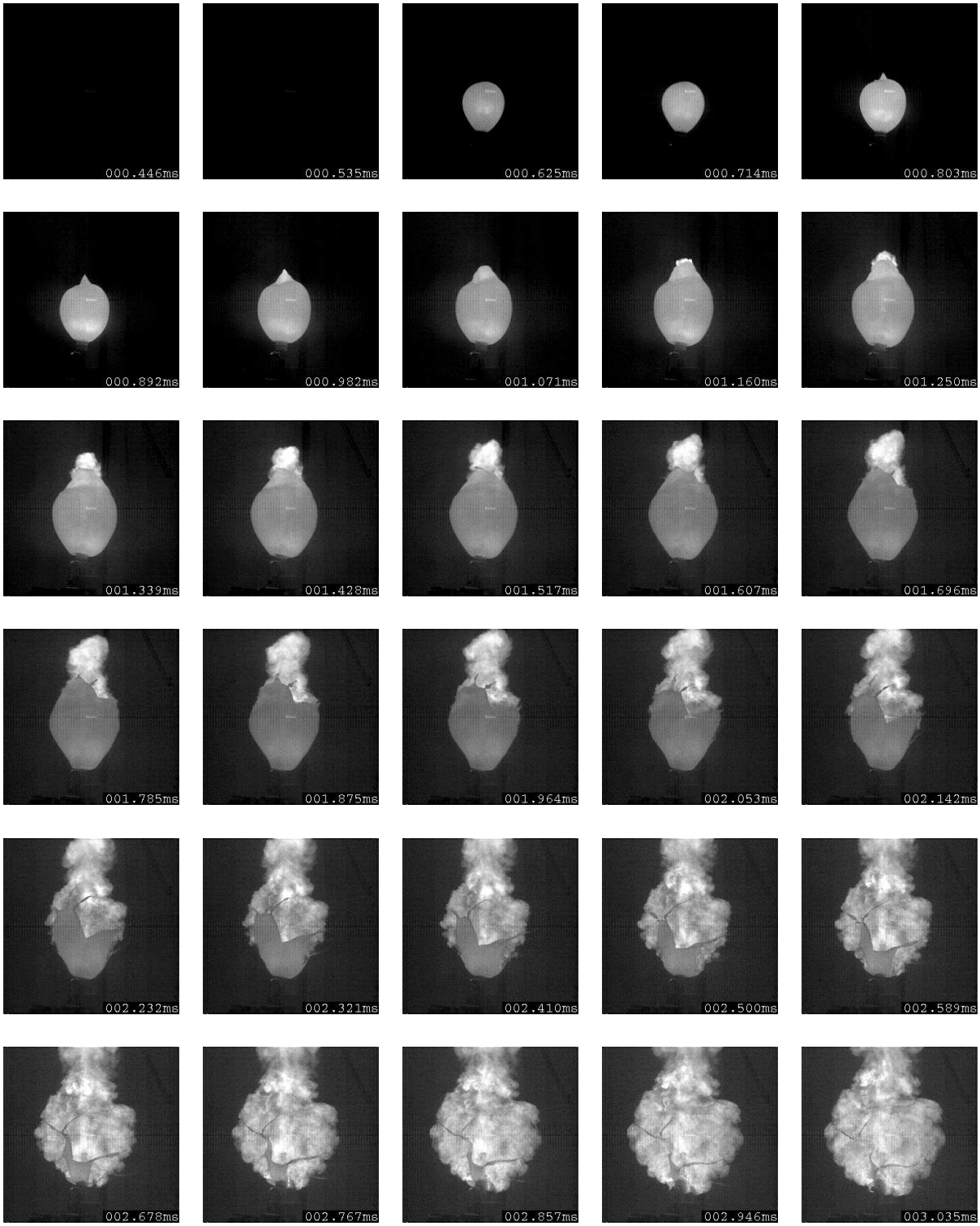

B.31: Shot 106, frames 5 to 34, interframe time: 89 μs, Φ = **2.5**, Δt(0.6 m)=1.42 ms, Δt(1.2 m)=3.10 ms

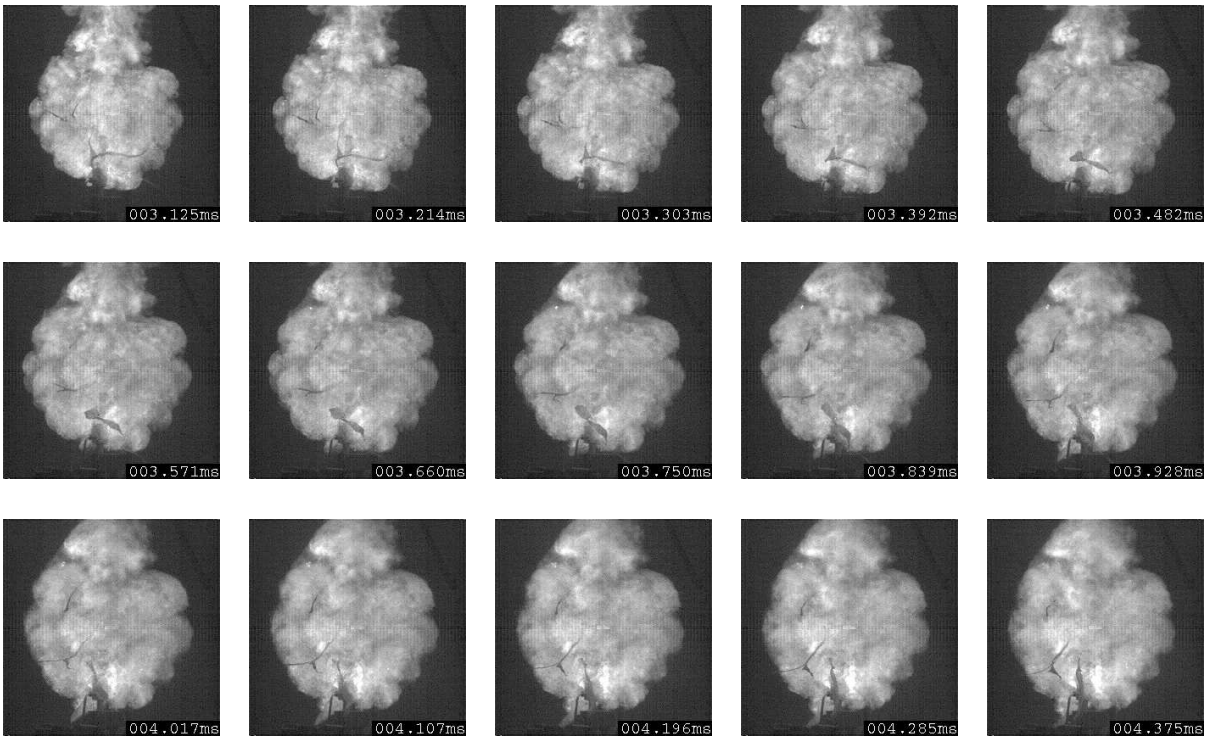

B.32: Shot 106, frames 35 to 49, interframe time: 89 μs, Φ = **2.5**, Δt(0.6 m)=1.49 ms, Δt(1.2 m)=3.24 ms

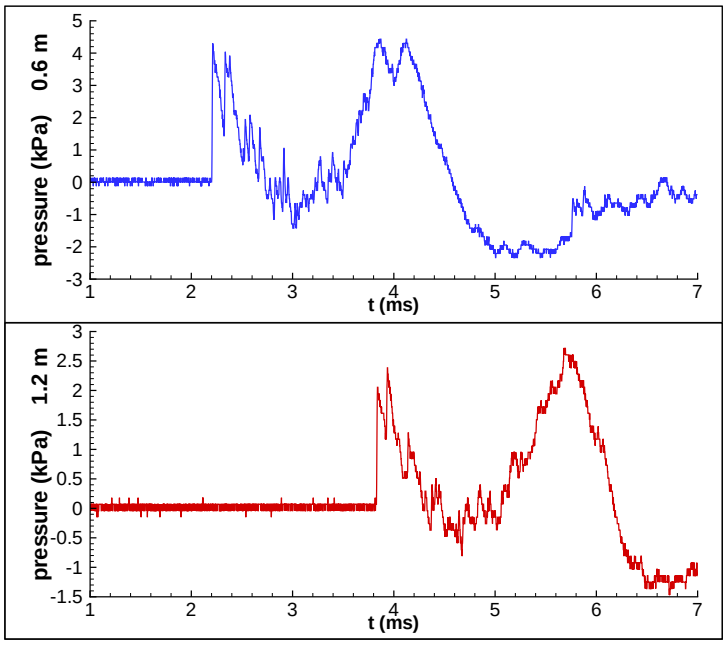

B.33: Shot 106. Pressure traces from the pencil gauges located at 0.6 and 1.2 m.

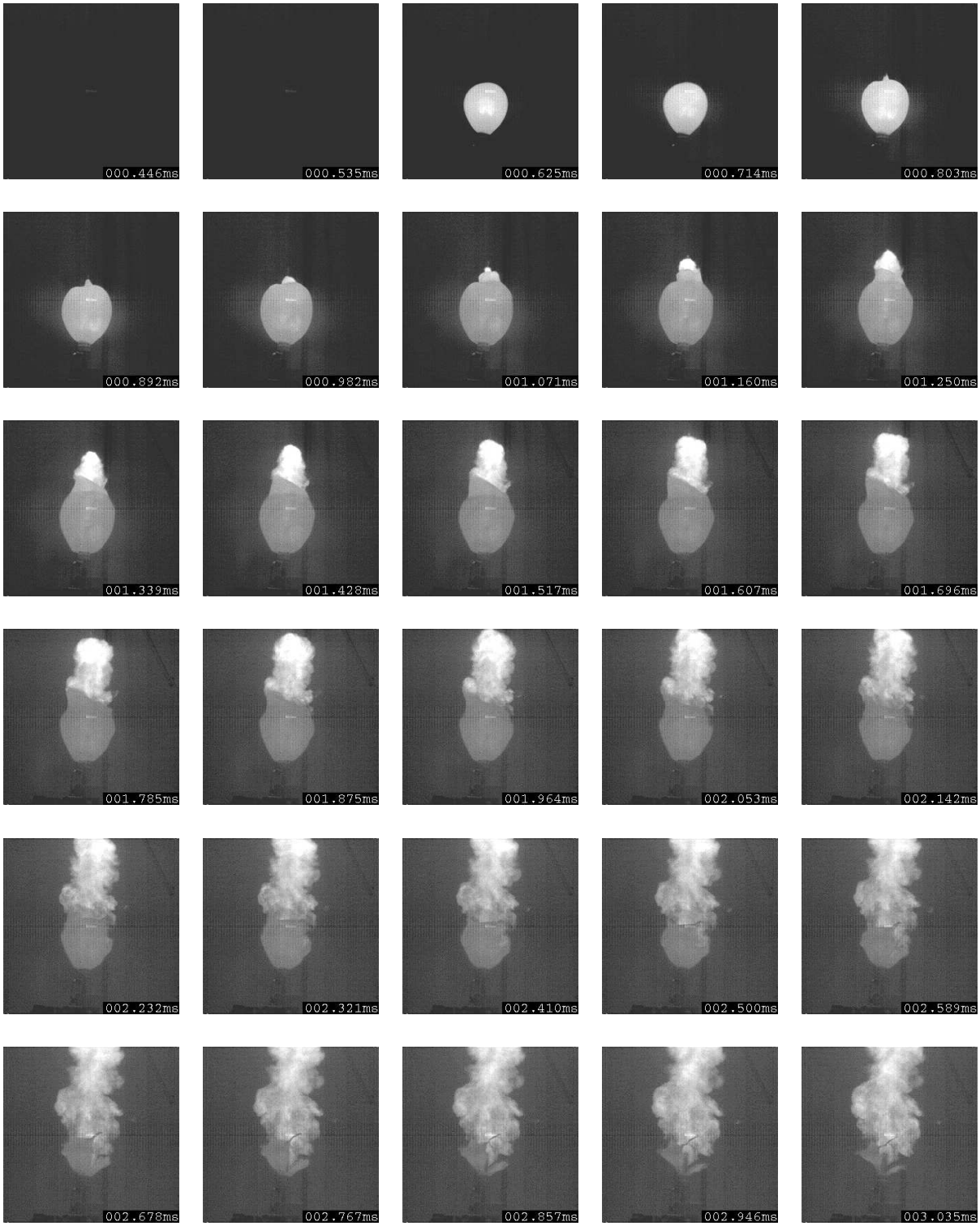

B.34: Shot 114, frames 5 to 34, interframe time: 89 μs, $\Phi = \mathbf{3}$, Δt(0.6 m)=1.49 ms, Δt(1.2 m)=3.25 ms

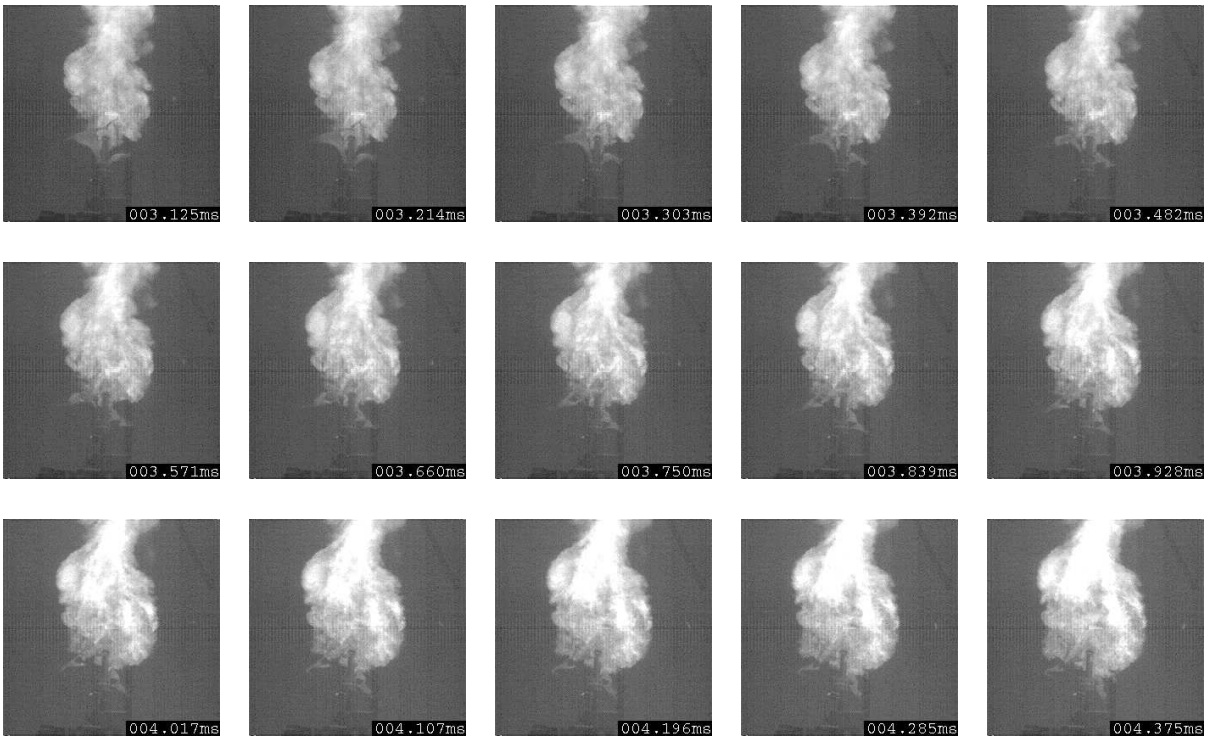

B.35: Shot 114, frames 35 to 49, interframe time: 89 μs, Φ = **3**, Δt(0.6 m)=1.41 ms, Δt(1.2 m)=3.12 ms

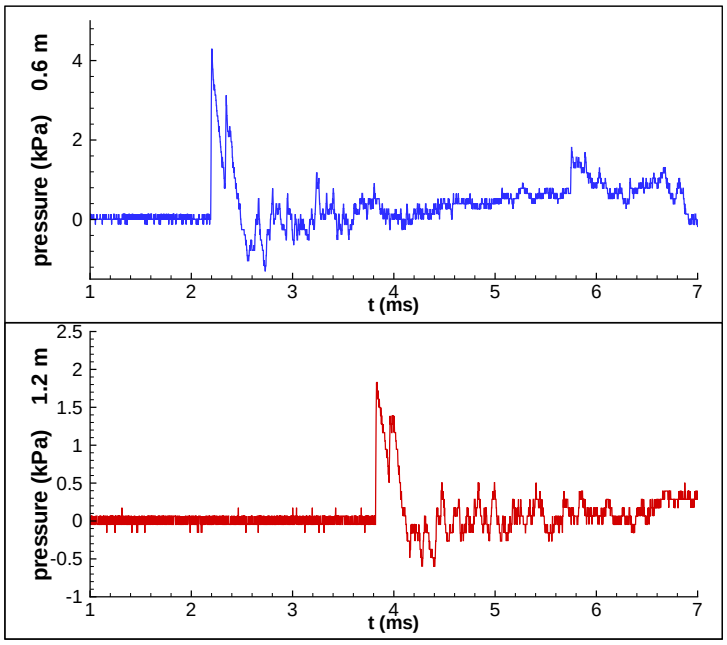

B.36: Shot 114. Pressure traces from the pencil gauges located at 0.6 and 1.2 m.

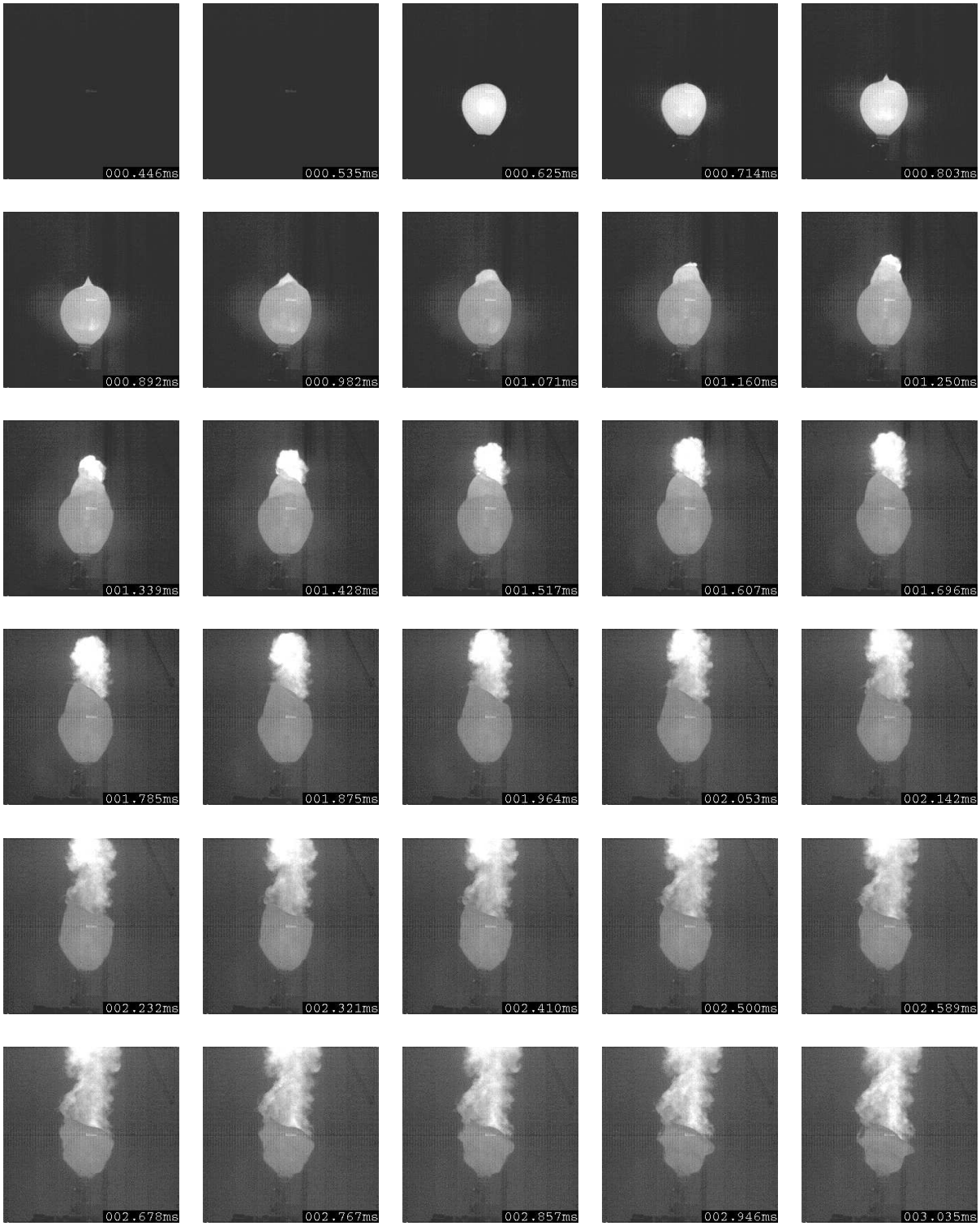

B.37: Shot 115, frames 5 to 34, interframe time: 89 μs, $\Phi = \mathbf{3}$, Δt(0.6 m)=1.43 ms, Δt(1.2 m)=3.13 ms

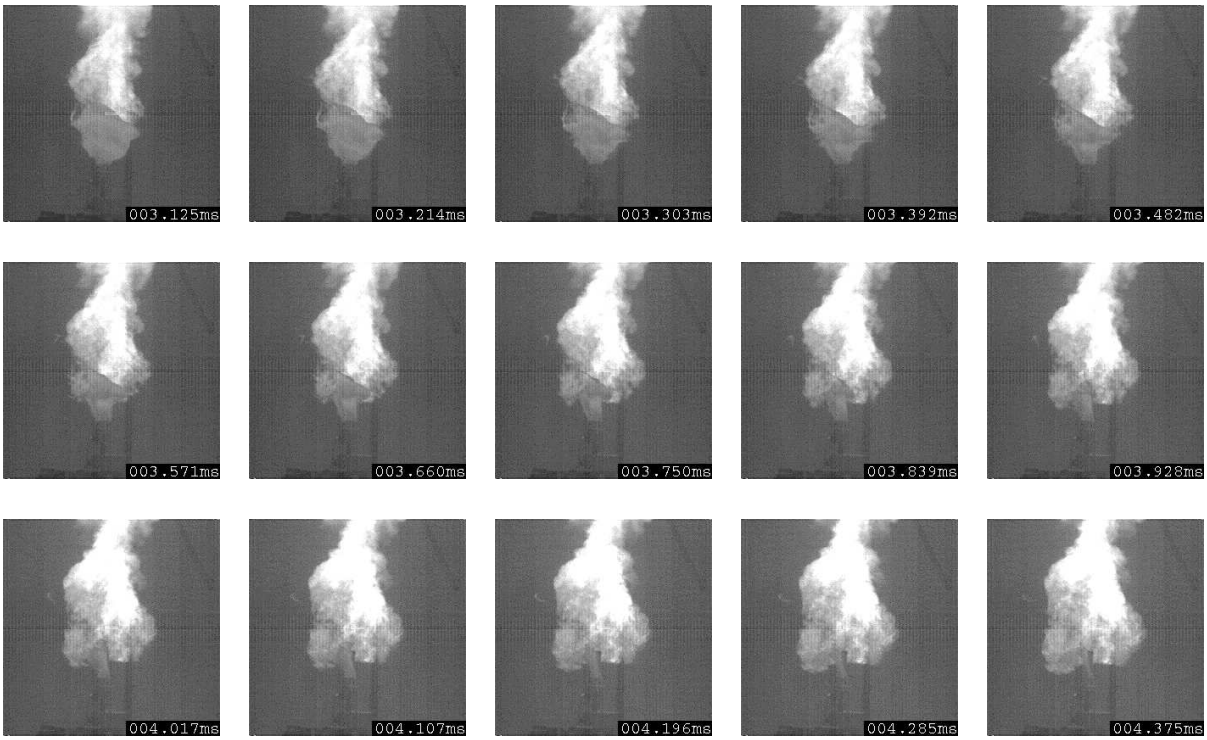

B.38: Shot 115, frames 35 to 49, interframe time: 89 μs, Φ = **3**, Δt(0.6 m)=1.50 ms, Δt(1.2 m)=3.25 ms

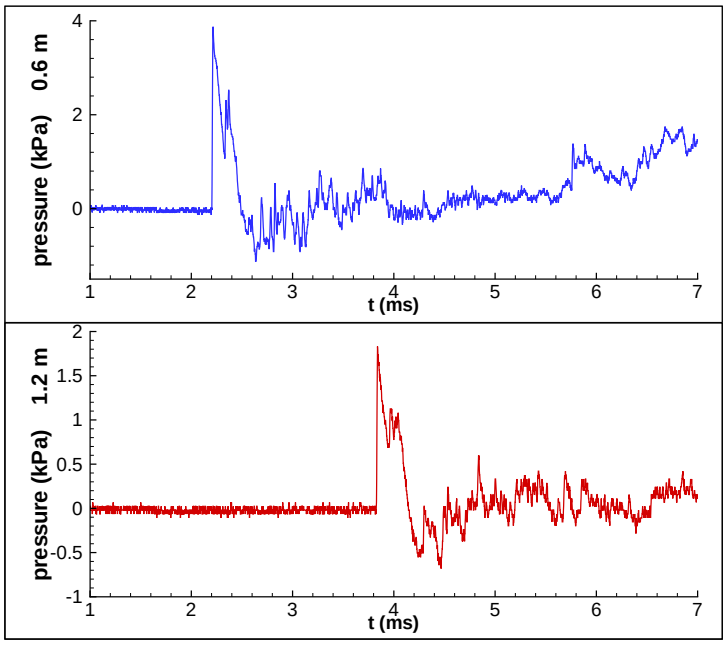

B.39: Shot 115. Pressure traces from the pencil gauges located at 0.6 and 1.2 m.

C Shotlist

shot number	equiv. ratio Φ	initiation location (b)ottom / (c)enter	initiator mixture
54	1	c	C_3H_8
55	1	c	C_3H_8
56	1.5	c	C_3H_8
57	2	c	C_3H_8
58	2	c	C_3H_8
59	1.5	c	C_3H_8
60	1.75	c	C_3H_8
61	1.75	c	C_3H_8
63	2.5	c	C_3H_8
64	2.5	c	C_3H_8
65	3	c	C_3H_8
66	3	c	C_3H_8
67	2.75	c	C_3H_8
68	2.75	c	C_3H_8
69	2.25	c	C_3H_8
70	2.25	c	C_3H_8
72	1	c	C_3H_8
73	1	c	C_3H_8
74	1.5	c	C_3H_8
75	1.5	c	C_3H_8
76	2	c	C_3H_8
77	2	c	C_3H_8
78	2	c	C_3H_8
79	2.5	c	C_3H_8
80	2.5	c	C_3H_8
81	3	c	C_3H_8
82	3	c	C_3H_8
83	2	c	C_3H_8
84	2	c	C_3H_8
85	2	c	C_3H_8
87	1	c	C_3H_8
88	2	c	C_3H_8
103	2.5	c	C_3H_8
104	2.5	c	C_3H_8
105	2.5	c	C_3H_8
106	2.5	c	C_3H_8
107	2	c	C_3H_8
108	2	c	C_3H_8
109	2	c	C_3H_8
110	1.5	c	C_3H_8
111	1.5	c	C_3H_8
112	1.5	c	C_3H_8
113	1	c	C_3H_8
114	3	c	C_3H_8
115	3	c	C_3H_8
143	1.5	b	C_2H_2
144	1.5	b	C_2H_2
146	1	b	C_2H_2
147	1.5	b	C_2H_2
148	1.5	b	C_2H_2
149	2	b	C_2H_2
150	2	b	C_2H_2
151	2.5	b	C_2H_2
152	2.5	b	C_2H_2
153	2.5	b	C_2H_2
154	2.5	b	C_2H_2
155	2.5	b	C_2H_2
156	2.5	b	C_2H_2
157	2.5	b	C_2H_2
158	3	b	C_2H_2
159	3	b	C_2H_2
161	2.5	b	C_2H_2
162	1.5	b	C_2H_2
163	1.5	b	C_2H_2
164	2	b	C_2H_2
165	1.5	b	C_2H_2
166	1	c	C_2H_2
167	1	c	C_2H_2
168	1.5	c	C_2H_2
169	1.5	c	C_2H_2
170	1.5	c	C_2H_2
171	2	c	C_2H_2
172	2	c	C_2H_2
173	2	c	C_2H_2
174	2.5	c	C_2H_2
175	2.5	c	C_2H_2
176	3	c	C_2H_2
177	3	c	C_2H_2

Table 2: Shotlist of experiments with balloon charge, which were used for the data analysis and the plots shown in A and the text.

D Initial balloon shape

The balloon is initially bulb shaped, and differed from shot to shot. In order to quantify the deviation from a perfact sphere balloon shapes from three experiments are shown in Fig.D.1 along with the outline of a sphere of the same volume. In Tables 3 to 5 the balloon outline for these shots is given as numerical values.

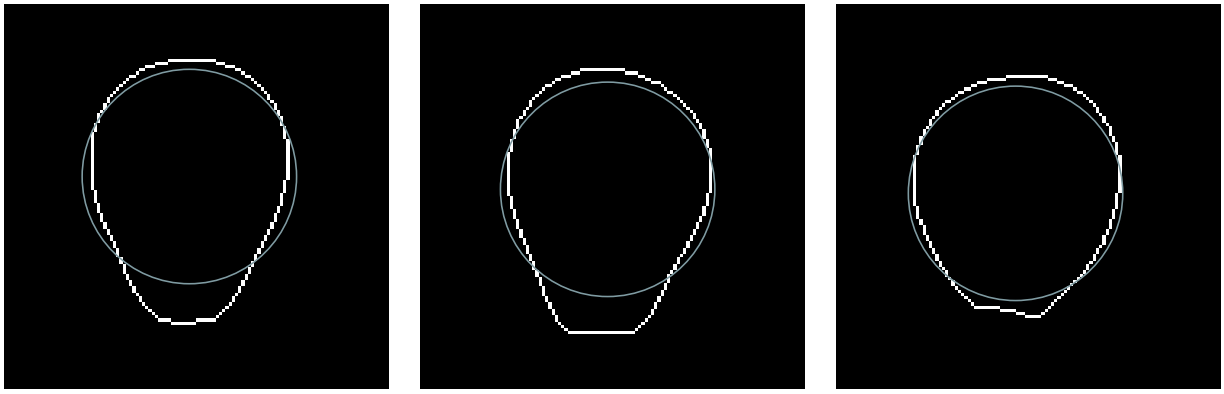

Shot 109 Shot 113 Shot114

D.1: Outline of balloon geometry (white) from first high speed video image and ouline of a sphere (gray) with same volume. The image is cropped to 120×120 pixel which corresponds to a field of view of 267×267 mm.

x	y	x	y	x	y	x	y	x	y	x	y
-11.1	-13.4	-8.9	-13.4	-6.7	-13.4	-4.5	-13.4	-2.2	-13.4	0.0	-13.4
2.2	-13.4	4.5	-13.4	6.7	-13.4	8.9	-13.4	11.1	-13.4	13.4	-13.4
15.6	-13.4	17.8	-13.4	20.0	-13.4	-20.0	-15.6	-17.8	-15.6	-15.6	-15.6
-13.4	-15.6	22.3	-15.6	24.5	-15.6	26.7	-15.6	-26.7	-17.8	-24.5	-17.8
-22.3	-17.8	28.9	-17.8	31.2	-17.8	33.4	-17.8	-31.2	-20.0	-28.9	-20.0
35.6	-20.0	37.9	-20.0	-33.4	-22.3	40.1	-22.3	-37.9	-24.5	-35.6	-24.5
42.3	-24.5	44.5	-24.5	-40.1	-26.7	46.8	-26.7	-42.3	-28.9	49.0	-28.9
-44.5	-31.2	51.2	-31.2	-46.8	-33.4	53.4	-33.4	-49.0	-35.6	55.7	-35.6
-51.2	-37.9	57.9	-37.9	-53.4	-40.1	57.9	-40.1	-53.4	-42.3	60.1	-42.3
-55.7	-44.5	62.3	-44.5	-55.7	-46.8	62.3	-46.8	-57.9	-49.0	64.6	-49.0
-60.1	-51.2	64.6	-51.2	-60.1	-53.4	66.8	-53.4	-60.1	-55.7	66.8	-55.7
-62.3	-57.9	66.8	-57.9	-62.3	-60.1	69.0	-60.1	-62.3	-62.3	69.0	-62.3
-64.6	-64.6	69.0	-64.6	-64.6	-66.8	69.0	-66.8	-64.6	-69.0	71.2	-69.0
-64.6	-71.2	71.2	-71.2	-64.6	-73.5	71.2	-73.5	-64.6	-75.7	71.2	-75.7
-64.6	-77.9	71.2	-77.9	-64.6	-80.2	71.2	-80.2	-64.6	-82.4	71.2	-82.4
-64.6	-84.6	71.2	-84.6	-64.6	-86.8	71.2	-86.8	-64.6	-89.1	71.2	-89.1
-64.6	-91.3	71.2	-91.3	-64.6	-93.5	71.2	-93.5	-64.6	-95.7	71.2	-95.7
-64.6	-98.0	69.0	-98.0	-64.6	-100.2	69.0	-100.2	-64.6	-102.4	69.0	-102.4
-62.3	-104.6	69.0	-104.6	-62.3	-106.9	66.8	-106.9	-62.3	-109.1	66.8	-109.1
-62.3	-111.3	66.8	-111.3	-60.1	-113.6	66.8	-113.6	-60.1	-115.8	64.6	-115.8
-60.1	-118.0	64.6	-118.0	-57.9	-120.2	62.3	-120.2	-57.9	-122.5	62.3	-122.5
-57.9	-124.7	62.3	-124.7	-55.7	-126.9	60.1	-126.9	-55.7	-129.1	60.1	-129.1
-53.4	-131.4	57.9	-131.4	-53.4	-133.6	57.9	-133.6	-51.2	-135.8	55.7	-135.8
-51.2	-138.0	55.7	-138.0	-49.0	-140.3	53.4	-140.3	-49.0	-142.5	53.4	-142.5
-46.8	-144.7	51.2	-144.7	-46.8	-147.0	51.2	-147.0	-46.8	-149.2	49.0	-149.2
-44.5	-151.4	49.0	-151.4	-44.5	-153.6	46.8	-153.6	-42.3	-155.9	46.8	-155.9
-42.3	-158.1	44.5	-158.1	-42.3	-160.3	44.5	-160.3	-40.1	-162.5	42.3	-162.5
-40.1	-164.8	42.3	-164.8	-37.9	-167.0	40.1	-167.0	-37.9	-169.2	40.1	-169.2
-35.6	-171.4	37.9	-171.4	-35.6	-173.7	37.9	-173.7	-33.4	-175.9	35.6	-175.9
-31.2	-178.1	33.4	-178.1	-31.2	-180.4	33.4	-180.4	-28.9	-182.6	31.2	-182.6
-26.7	-184.8	28.9	-184.8	-24.5	-187.0	26.7	-187.0	-22.3	-189.3	24.5	-189.3
-20.0	-191.5	22.3	-191.5	-17.8	-193.7	-15.6	-193.7	-13.4	-193.7	-11.1	-193.7
8.9	-193.7	11.1	-193.7	13.4	-193.7	15.6	-193.7	17.8	-193.7	20.0	-193.7
-8.9	-195.9	-6.7	-195.9	-4.5	-195.9	-2.2	-195.9	0.0	-195.9	2.2	-195.9
4.5	-195.9	6.7	-195.9								

Table 3: Shot 109. Initial balloon outline coordinates are given in mm, where x is the horizontal axis. The initiator tube was located for the center initiation at the coordinate origin.

x	y	x	y	x	y	x	y	x	y	x	y
-17.8	-13.4	-15.6	-13.4	-13.4	-13.4	-11.1	-13.4	-8.9	-13.4	-6.7	-13.4
-4.5	-13.4	-2.2	-13.4	0.0	-13.4	2.2	-13.4	4.5	-13.4	6.7	-13.4
8.9	-13.4	11.1	-13.4	-24.5	-15.6	-22.3	-15.6	-20.0	-15.6	13.4	-15.6
15.6	-15.6	17.8	-15.6	20.0	-15.6	-31.2	-17.8	-28.9	-17.8	-26.7	-17.8
22.3	-17.8	24.5	-17.8	-35.6	-20.0	-33.4	-20.0	26.7	-20.0	28.9	-20.0
-37.9	-22.3	31.2	-22.3	33.4	-22.3	35.6	-22.3	-42.3	-24.5	-40.1	-24.5
37.9	-24.5	-44.5	-26.7	40.1	-26.7	-46.8	-28.9	42.3	-28.9	44.5	-28.9
-49.0	-31.2	46.8	-31.2	-51.2	-33.4	49.0	-33.4	-53.4	-35.6	51.2	-35.6
-53.4	-37.9	53.4	-37.9	-55.7	-40.1	55.7	-40.1	-57.9	-42.3	57.9	-42.3
-57.9	-44.5	60.1	-44.5	-60.1	-46.8	60.1	-46.8	-62.3	-49.0	62.3	-49.0
-62.3	-51.2	64.6	-51.2	-62.3	-53.4	64.6	-53.4	-64.6	-55.7	66.8	-55.7
-64.6	-57.9	66.8	-57.9	-64.6	-60.1	66.8	-60.1	-66.8	-62.3	69.0	-62.3
-66.8	-64.6	69.0	-64.6	-66.8	-66.8	69.0	-66.8	-66.8	-69.0	71.2	-69.0
-69.0	-71.2	71.2	-71.2	-69.0	-73.5	71.2	-73.5	-69.0	-75.7	71.2	-75.7
-69.0	-77.9	71.2	-77.9	-69.0	-80.2	71.2	-80.2	-69.0	-82.4	71.2	-82.4
-69.0	-84.6	71.2	-84.6	-69.0	-86.8	71.2	-86.8	-69.0	-89.1	71.2	-89.1
-69.0	-91.3	71.2	-91.3	-69.0	-93.5	71.2	-93.5	-69.0	-95.7	71.2	-95.7
-69.0	-98.0	71.2	-98.0	-69.0	-100.2	69.0	-100.2	-66.8	-102.4	69.0	-102.4
-66.8	-104.6	69.0	-104.6	-66.8	-106.9	69.0	-106.9	-66.8	-109.1	66.8	-109.1
-64.6	-111.3	66.8	-111.3	-64.6	-113.6	66.8	-113.6	-64.6	-115.8	64.6	-115.8
-62.3	-118.0	64.6	-118.0	-62.3	-120.2	62.3	-120.2	-62.3	-122.5	62.3	-122.5
-60.1	-124.7	60.1	-124.7	-60.1	-126.9	60.1	-126.9	-60.1	-129.1	57.9	-129.1
-57.9	-131.4	57.9	-131.4	-57.9	-133.6	55.7	-133.6	-55.7	-135.8	55.7	-135.8
-55.7	-138.0	53.4	-138.0	-55.7	-140.3	53.4	-140.3	-53.4	-142.5	51.2	-142.5
-53.4	-144.7	49.0	-144.7	-51.2	-147.0	49.0	-147.0	-51.2	-149.2	46.8	-149.2
-51.2	-151.4	46.8	-151.4	-49.0	-153.6	44.5	-153.6	-49.0	-155.9	42.3	-155.9
-46.8	-158.1	42.3	-158.1	-46.8	-160.3	42.3	-160.3	-46.8	-162.5	40.1	-162.5
-44.5	-164.8	40.1	-164.8	-44.5	-167.0	37.9	-167.0	-44.5	-169.2	37.9	-169.2
-42.3	-171.4	35.6	-171.4	-42.3	-173.7	35.6	-173.7	-40.1	-175.9	33.4	-175.9
-40.1	-178.1	33.4	-178.1	-37.9	-180.4	31.2	-180.4	-37.9	-182.6	31.2	-182.6
-35.6	-184.8	28.9	-184.8	-35.6	-187.0	26.7	-187.0	-33.4	-189.3	24.5	-189.3
-31.2	-191.5	22.3	-191.5	-28.9	-193.7	20.0	-193.7	-26.7	-195.9	-24.5	-195.9
-22.3	-195.9	-20.0	-195.9	-17.8	-195.9	-15.6	-195.9	-13.4	-195.9	-11.1	-195.9
-8.9	-195.9	-6.7	-195.9	-4.5	-195.9	-2.2	-195.9	0.0	-195.9	2.2	-195.9
4.5	-195.9	6.7	-195.9	8.9	-195.9	11.1	-195.9	13.4	-195.9	15.6	-195.9
17.8	-195.9										

Table 4: Shot 109. Initial balloon outline coordinates are given in mm, where x is the horizontal axis. The initiator tube was located for the center initiation at the coordinate origin.

x	y	x	y	x	y	x	y	x	y	x	y
-2.2	-31.2	0.0	-31.2	2.2	-31.2	4.5	-31.2	6.7	-31.2	8.9	-31.2
11.1	-31.2	13.4	-31.2	15.6	-31.2	17.8	-31.2	20.0	-31.2	22.3	-31.2
24.5	-31.2	-15.6	-33.4	-13.4	-33.4	-11.1	-33.4	-8.9	-33.4	-6.7	-33.4
-4.5	-33.4	26.7	-33.4	28.9	-33.4	31.2	-33.4	-22.3	-35.6	-20.0	-35.6
-17.8	-35.6	33.4	-35.6	35.6	-35.6	-26.7	-37.9	-24.5	-37.9	37.9	-37.9
40.1	-37.9	42.3	-37.9	-31.2	-40.1	-28.9	-40.1	44.5	-40.1	-35.6	-42.3
-33.4	-42.3	46.8	-42.3	49.0	-42.3	-37.9	-44.5	51.2	-44.5	-40.1	-46.8
53.4	-46.8	-44.5	-49.0	-42.3	-49.0	55.7	-49.0	-46.8	-51.2	57.9	-51.2
-49.0	-53.4	60.1	-53.4	-51.2	-55.7	60.1	-55.7	-51.2	-57.9	62.3	-57.9
-53.4	-60.1	64.6	-60.1	-55.7	-62.3	64.6	-62.3	-55.7	-64.6	66.8	-64.6
-57.9	-66.8	69.0	-66.8	-60.1	-69.0	69.0	-69.0	-60.1	-71.2	69.0	-71.2
-62.3	-73.5	71.2	-73.5	-62.3	-75.7	71.2	-75.7	-62.3	-77.9	73.5	-77.9
-64.6	-80.2	73.5	-80.2	-64.6	-82.4	73.5	-82.4	-64.6	-84.6	73.5	-84.6
-66.8	-86.8	75.7	-86.8	-66.8	-89.1	75.7	-89.1	-66.8	-91.3	75.7	-91.3
-66.8	-93.5	75.7	-93.5	-66.8	-95.7	75.7	-95.7	-66.8	-98.0	75.7	-98.0
-66.8	-100.2	75.7	-100.2	-66.8	-102.4	75.7	-102.4	-66.8	-104.6	75.7	-104.6
-66.8	-106.9	75.7	-106.9	-66.8	-109.1	75.7	-109.1	-66.8	-111.3	75.7	-111.3
-66.8	-113.6	73.5	-113.6	-66.8	-115.8	73.5	-115.8	-66.8	-118.0	73.5	-118.0
-66.8	-120.2	73.5	-120.2	-64.6	-122.5	73.5	-122.5	-64.6	-124.7	71.2	-124.7
-64.6	-126.9	71.2	-126.9	-64.6	-129.1	71.2	-129.1	-62.3	-131.4	69.0	-131.4
-62.3	-133.6	69.0	-133.6	-60.1	-135.8	69.0	-135.8	-60.1	-138.0	66.8	-138.0
-60.1	-140.3	66.8	-140.3	-57.9	-142.5	64.6	-142.5	-57.9	-144.7	64.6	-144.7
-55.7	-147.0	64.6	-147.0	-55.7	-149.2	62.3	-149.2	-53.4	-151.4	60.1	-151.4
-53.4	-153.6	60.1	-153.6	-51.2	-155.9	57.9	-155.9	-51.2	-158.1	57.9	-158.1
-49.0	-160.3	55.7	-160.3	-49.0	-162.5	53.4	-162.5	-46.8	-164.8	53.4	-164.8
-44.5	-167.0	51.2	-167.0	-44.5	-169.2	49.0	-169.2	-42.3	-171.4	46.8	-171.4
-40.1	-173.7	44.5	-173.7	-40.1	-175.9	42.3	-175.9	-37.9	-178.1	40.1	-178.1
-35.6	-180.4	37.9	-180.4	-33.4	-182.6	35.6	-182.6	-31.2	-184.8	33.4	-184.8
-28.9	-187.0	31.2	-187.0	-26.7	-189.3	28.9	-189.3	-24.5	-191.5	-22.3	-191.5
-20.0	-191.5	-17.8	-191.5	-15.6	-191.5	-13.4	-191.5	-11.1	-191.5	-8.9	-191.5
26.7	-191.5	-6.7	-193.7	-4.5	-193.7	-2.2	-193.7	0.0	-193.7	2.2	-193.7
24.5	-193.7	4.5	-195.9	6.7	-195.9	8.9	-195.9	22.3	-195.9	11.1	-198.2
13.4	-198.2	15.6	-198.2	17.8	-198.2	20.0	-198.2				

Table 5: Shot 114. Initial balloon outline coordinates are given in mm, where x is the horizontal axis. The initiator tube was located for the center initiation at the coordinate origin.